Mass transfer in Direct Air Capture sorbents

Modeling adsorption and desorption of carbon dioxide and water in typical solid sorbents

Paula Sophie Sauter

Delft University of Technology

TU Delft

Mass transfer in Direct Air Capture sorbents

Modeling adsorption and desorption of carbon dioxide and water in typical solid sorbents

by

Paula Sophie Sauter

to obtain the degree of Master of Science
at the Delft University of Technology,
to be defended publicly on Tuesday August 27, 2024 at 10:00 AM.

Student number:	5830222	
Project duration:	November 27, 2023 – August 27, 2024	
Thesis committee:	Dr. ir. T. M. J. Nijssen,	TU Delft P&E, supervisor
	Dr. O. Moultos,	TU Delft P&E
	Dr. ir. D. A. Vermaas,	TU Delft ChemE

Cover: Photo by Matt Palmer on Unsplash

An electronic version of this thesis is available at http://repository.tudelft.nl/.

TU Delft

Preface

Working on this thesis has been a truly engaging experience with lots of learnings. The environmental relevance of this research has made it all the more meaningful for me, and I have genuinely enjoyed applying and expanding my knowledge gained throughout my time as a student.

I am especially grateful to my supervisor, Tim Nijssen, whose support and guidance have been invaluable. Our meetings were a great blend of focused discussions and lighter moments, making the research process both productive and enjoyable. His insights and encouragement made a real difference throughout this journey.

I also want to thank my friends and family for their constant support. Their encouragement has kept me going through the ups and downs of this process, and I truly couldn't have done it without them. As a not insignificant part of my time working on this thesis, I want to mention everyone that made the long hours in the P&E flexroom feel shorter and lighter.

As I wrap up my studies and move on to the next chapter, I feel grateful for my time in Delft and everyone I was lucky enough to meet along the way. This journey has been full of learning, growth, fun and laughter, and I am looking forward to seeing where life takes me next.

Thank you all for being there with me along the way.

Paula Sophie Sauter
Delft, August 2024

Abstract

The severe rise in global surface temperature and its associated damages to the ecosystem are primarily attributed to anthropogenic carbon dioxide emissions. The present CO_2 levels in the air today and the continuing emissions necessitate even the most ambitious development scenarios to rely on net negative CO_2 emissions to limit the global temperature rise to 1.5°C until the year 2100. Direct Air Capture (DAC) refers to the direct extraction of carbon dioxide from the ambient air and addresses the need for net negative emissions. As the technology is still in its infancy, understanding and modeling the occurring processes is crucial.

This thesis addresses the challenges in modeling adsorption and desorption processes in solid-sorbent Direct Air Capture, focusing on the complexities introduced by the porous structures of sorbent materials and the effects of humidity. Current models fail to incorporate the full spectrum of mass transfer processes, or do not consider the significant effects of humidity on the process. To bridge this gap, a detailed mass transfer and reaction kinetics model at the particle scale was developed, aiming to provide a more accurate framework for predicting the performance of amine-functionalized sorbents in DAC applications. The model was developed on a particle scale, and subsequently included in contactor models of a packed-bed and a monolith. The study considered all relevant transport mechanisms, finding that pore diffusion and reaction kinetics are critical in governing sorbent uptake dynamics. The contactor model effectively compares the performance of packed-bed and monolith reactors, highlighting a trade-off between productivity and energy efficiency, with significant potentials for energy savings offered by the monolith.

Contents

Nomenclature

Abbreviations

Abbreviation	Definition
CFD	Computational Fluid Dynamics
DAC	Direct Air Capture
MOL	Method of lines
ODE	Ordinary Differential Equation
PDE	Partial Differential Equation
RH	Relative Humidity
S-TVSA	Steam - assisted temperature-vacuum swing adsorption
TGA	Thermogravimetric analysis
TVSA	Temperature-vacuum swing adsorption

Symbols

Symbol	Definition	Unit
A_j	Arrhenius prefactor of reaction j	reac. spec.
a_i	Activity species i	[-]
b_1	Channel width monolith	[m]
b_2	Cell width monolith	[m]
C	Concentration	[mol/m^3]
D	Diffusion coefficient	[m^2/s]
D_p	Particle diameter	[m]
d_p	Pore diameter	[m]
dw	Wall thickness monolith	[m]
E_j	Activation energy of reaction j	[J/mol]
G	Gibbs free energy	[J/mol]
H	Enthalpy	[J/mol]
h	Mass transfer coefficient	[m/s]
J	Diffusive molar flux	[mol/s]
K_j	Equilibrium constant reaction j	reac. spec.
k_j	Kinetic factor of reaction j	reac. spec.
Kn	Knudsen number	[-]
L	Contactor length	[m]
M	Molar mass	[kg/mol]
m	Mass	[kg]
N	Molar quantity	[mol]
P	Pressure	[Pa]
p_i	Partial pressure of component i	[Pa]
P_{ads}	Productivity	[mol/kg s]
Pe	Péclet number	[-]
Pr	Prandtl number	[-]
q	Loading	[mol/kg]
R	Particle radius	[m]
R_j	Rate of reaction j	[mol/m^3 s]

Symbol	Definition	Unit
Re	Reynolds number	[-]
S	Entropy	[J/mol K]
Sc	Schmidt number	[-]
Sh	Sherwood number	[-]
T	Temperature	[K]
t	time	[s]
$\dot{V}$	Volumetric flow rate	[l/s]
v_i	Interstitial velocity	[m/s]
v_s	Superficial velocity	[m/s]
W_{fan}	Energy required by the fan	[J]
x	Mole fraction	[-]
y	Mass fraction	[-]
ε	Porosity	[-]
$\mathbf{\Gamma}$	Flux diffusion matrix	[kg/m s]
γ	Activity coefficient	[-]
ν	Kinematic viscosity	[m^2/s]
μ	Dynamic viscosity	[Pa·s]
Φ	Amine efficiency	[-]
ρ	Density	[kg/m^3]
σ_{rel}	Relative standard deviation	[-]
τ	Stoichiometric timescale	[-]
τ_p	Tortuosity	[-]

Indices

Index	Definition
am	Amine
avg	Average
b	Bed
bi	Bicarbonate
ch	Channel
cm	Carbamate
eq	Equivalent
p	Particle
pb	Packed bed
ph	Physisorption
pr	Protonated
mon	Monolith
s	Sorbent
∞	At equilibrium

1

Introduction

The Intergovernmental Panel on Climate Change (IPCC) has reported a rise in global surface temperature of approximately $1.1\,^{\circ}$C between $1850-1900$ and $2011-2020$, primarily attributed to human activities [10]. Carbon dioxide, followed by methane, is the primary greenhouse gas influencing climate change [80, 10]. Over the past 200 years, the concentration of CO_2 in the atmosphere has increased from approximately 280 ppm [96] to about 420 ppm in 2024 [90, 56]. Anthropogenic CO_2 emissions have consistently risen over recent decades, reaching approximately 41.46 Gt per year in 2022 [68]. In the recent IPCC synthesis report from 2023 [10], multiple scenarios for development until the end of the century are explained and compared. Only in a small fraction of the most ambitious scenarios can global warming be limited to an increase of $1.5\,^{\circ}$C without overshooting before 2100. Rogelj et al. [69] conclude from their analysis that there is no feasible scenario that avoids an overshoot. Overshoot implies that the global temperature increase will exceed $1.5\,^{\circ}$C before subsequently reducing to that level before 2100 by removing greenhouse gases from the atmosphere. An overshoot entails severe and potentially irreversible consequences for ecosystems affected by processes such as glacier melt or sea-level rise. A larger overshoot necessitates a higher amount of CO_2 that must be removed from the atmosphere. It can be estimated that approximately 220 Gt of net negative emissions will be required to decrease the global surface temperature by one-tenth of a degree. All pathways mentioned in the report - with or without overshoot - rely on net negative emissions of CO_2 between 220 and 360 Gt in total [10] to achieve the goal of limiting the temperature rise to $1.5\,^{\circ}$C. In general, technologies to capture CO_2 can play a crucial role in achieving to:

1. lower emissions in the near future,
2. balance emissions from distributed sources, such as in aviation and
3. compensate for the overshoot by achieving net negative emissions [10].

To drive the development of solutions to reduce emissions in the near future (1), Carbon Capture and Storage (CCS) has been a key research topic in recent years [31]. Despite the increased employment of renewable energy sources, carbon emissions keep rising. To promptly reduce emissions, capturing carbon from exhaust gases at significant anthropogenic point sources like fossil power stations or steel and iron production sites, represents a promising approach. However, this method is insufficient to address the challenge of balancing emissions from distributed sources (2) or achieving net negative emissions to compensate for overshoot (3). Given that approximately half of the annual carbon dioxide emissions originate from distributed sources, the need for an alternative solution is evident [73]. Direct Air Capture (DAC) refers to the direct extraction of CO_2 from the ambient air, and was first proposed for climate change mitigation by Lackner in 1999 [43]. Since then, the field of DAC gained attention by many scientist and the number of publications increased significantly, particulary in the last fifteen years. Additionally, several start-up companies have been established, focusing on scaling up the technology to a commercial scale [73]. DAC offers the flexibility to be deployed independent of location and emission source, thus enabling the compensation for distributed sources. If the process is powered by sufficiently low-carbon energy and the extracted CO_2 is permanently stored, net negative emissions can be achieved.

1.1. Approaches to DAC

The design of a process to extract CO_2 from the ambient air bears challenges due to the dilute presence of CO_2, as well as the fluctuating environmental conditions like temperature and humidity. For Direct Air Capture to become a viable solution, the process must demonstrate resilience across diverse conditions and prioritize energy efficiency, while employing renewable energy sources to align with its environmental objectives. A promising approach to capture CO_2 from ambient air is the principle of sorption [82]. Various technologies, applying physical sorption, strong bases, amine-functionalized materials, aqueous amino acid solutions with guanidine precipitation, moisture-swing sorption, or electrochemical swing sorption, have been explored and are still topic of current research [82].

Strong base materials exhibit high chemical binding energy with CO_2 which makes them suitable to capture it from ambient air. After the absorption, a concentrated CO_2 stream can be released via a calcination step. However, this requires high temperatures which makes the process energy-intensive [82]. Nevertheless, the first commercial DAC capture systems are based on aqueous alkali hydroxide solutions (operated by Carbon Engineering [38]). In the closed-loop process, the air is exposed to the alkali hydroxide solution in a contactor, which reacts with CO_2 to form a solution that contains alkali carbonate species. Next, the solution is brought in contact with $Ca(OH)_2$ and calciumcarbonates are formed. The subsequent regeneration of the sorbent and release of the CO_2 is energy intensive, as it requires temperatures above $800°$C [23, 100]. To avoid the drawbacks in efficiency, a route of regeneration through an electrochemical process has been investigated. Although higher efficiency could be achieved, high costs of membrane materials did not make this an economically competitive option [23]. Moisture-swing sorbents bind CO_2 in dry and release it in humid conditions. This is achieved by the nature of quarternary amines which are bound by a support structure. As a result, the adsorption and desorption processes can be carried out without requiring external heating or cooling, leading to energy savings and eliminating the need for dedicated thermal units. However, applying the moisture-swing principle in Direct Air Capture makes the process sensitive to the weather conditions [94] and might require large quantities of water.

An approach by Custelcean et al. follows the principle of employing an aqueous amino acid solution that captures the CO_2, and binding it in crystalline form as a carbonate salt through guanidinium hydrogen bonding. To regenerate, the CO_2 can be released at temperatures around $80-120\,°$C, which facilitates an approach to DAC with low energy and material costs [77, 14]. Although exhibiting high efficacy, further research is needed to scale up and assess its practical viability [82]. Electrochemical processes for CO_2 capture are intriguing, yet current methods require higher CO_2 concentrations than present in ambient air ($\gtrsim 0.04\,\%/400\,\mathrm{ppm}$), posing feasibility challenges for DAC development [82].

The principle of physical sorbents relies on van der Waals or ion quadruple forces. Typical materials are zeolites, activated carbon, aluminia and metal-organic frameworks (MOFs). An advantage of physisorbents is the regeneration process. Due to the weak binding of CO_2, regeneration is comparatively easy and can be done at low temperatures [82]. However, a high binding strength is necessary to allow for high adsorption capacities especially in dilute conditions as present in the atmosphere [34]. Kumar et al. [41] compared the performance of four different physisorbents (one zeolite, two MOFs, and one hybrid ultramicroporous material (HUM)) and one chemisorbent (amine-functionalized mesoporous silica: TEPA-SBA-15) in terms of sorption capacity under atmospheric conditions. The amine-functionalized chemisorbent exhibits a high selectivity for CO_2 in dry conditions, as the amine groups do not react with N_2. The tested physisorbents show a high selectivity for CO_2 over N_2 as well, however they are highly influenced by the presence of water vapour, while the chemisorbents performance is not affected. The CO_2 uptake of physisorbents reduces drastically in the presence of water vapour as the molecules compete with each other for the adsorption sites on the sorbents surface [41]. They conclude that the tested physisorbents might be suitable to apply capture CO_2 from gases with high concentrations and low humidity, such as dried flue gases. Here the low regeneration cost could compensate for the lower uptake. As their performance decreases in dilute and humid conditions, they are less useful in the case of DAC when compared to amine-functionalized chemisorbents [41, 82]

The approach of employing amine functionalized materials for DAC originates from the long practiced CO_2 separation from gas mixtures, commonly by monoethanolamine (MEA), diethanolamine (DEA), and methyldiethanolamine (MDEA) [59]. High energy costs in the regeneration step due to their high heat capacities and heat losses due to evaporation lowers the efficiency of the process severely [82].

The application of solid amine functionalized materials has gained attention in the last years, and is already employed in multiple DAC plants, built by Climeworks [6] and Global Thermostat [29]. They have shown high potential for DAC due to their low energy consumption for regeneration compared to methods employing liquid solutions, chemical stability, high reversibility and availability [82, 23, 17]. They perform well under humid conditions [94], exhibit a higher binding strength than physisorbents as they rely on covalent bonding [53], but can be regenerated at rather low temperatures around $70-150\,^{\circ}\mathrm{C}$ [94]. As amine functionalized solid materials are a central focus of research on materials for DAC today [17], this work focuses on this technology.

1.2. Motivation and Research Questions

The diversity of materials considered for Direct Air Capture, including differences in porous structure, support material, amine type, amine loading, and functionalisation methods introduces variations in performance. Furthermore, the impact of humidity on the process is considerable [94]. Modeling the adsorption and desorption process bears challenges regarding the description of the pore structure, the kinetics and the interaction of CO_2 and H_2O. Prior dynamic models for the uptake of CO_2 on amine functionalized sorbents [27, 86, 35, 79, 57, 61] failed to encompass all relevant mass transfer processes and often disregarded the distinction between intra-particle mass transfer and chemical reaction kinetics, making them strongly material-specific. Additionally, these models often consider only dry air or pure CO2, neglecting the effects varying degrees of humidity in air.

Understanding the relevance of the different mass transfer steps is the basis for further research and crucial for process and material design. The influence of intra-particle mass transfer under DAC conditions is not yet covered by models in literature, and will be the focus of this study, where the following research questions are posed:

How do mass transfer and reaction kinetics on a particle scale influence adsorption and desorption in Direct Air Capture?

- Which mass transfer mechanisms are most relevant in the process of adsorption and desorption on a particle scale?
- Which material parameters are crucial to describe the process?
- Can a particle-scale model predict the adsorption behaviour on a contactor scale?
- Which mechanisms govern the breakthrough time?
- How do a packed bed and a monolith contactor compare in terms of productivity and energy consumption for the fan?

In this work, a rigorous mass transfer model for an amine functionalized, solid sorbent on the particle scale is developed. A primary focus is set on including the influence of water during the adsorption and desorption processes. For the development of the model, the commercially available sorbent Lewatit ®VP OC 1065 is chosen. The model is based on material properties as well as thermodynamic and kinetic parameters of the chemical binding mechanisms. This ensures the possibility of tailoring the model to different materials. Furthermore, the particle-scale model is included in contactor models of a fixed bed reactor and a monolith. The influence of particle-scale effects are evaluated and the performance of the different reactors compared.

Chapter 2 covers relevant background on sorbent materials, the principles of the technology, and previous models found in the literature. In Chapter 3 the numerical models developed in this work are explained, along with the relevant theory of mass transfer and adsorption effects as well as the specification of the simulated cases. The results drawn are elucidated in Chapter 4, followed by a discussion in Chapter 5. Chapter 6 provides a conclusion answering the research questions and recommendations for future work.

2

Background

2.1. Sorbent Material

The selection of the sorbent material significantly influences the performance of Direct Air Capture, as it can serve as a key solution to its inherent challenges. With variations in selectivity, capacity, kinetics, and regeneration behavior, the choice of the sorbent strongly impacts the process efficiency. Moreover, the choice of sorbents impacts the economic viability of the process, considering factors such as stability, availability, and affordability. Thus, a sorbent must fulfill several requirements, which are measurable through performance parameters summarized in the following [82, 94, 2]:

- **Selectivity for CO_2 and the influence of water:** The selectivity for CO_2 is a critical factor influencing the sorbent's uptake from the air stream and the purity of CO_2 in the desorption process. It can be expressed through selectivity towards a specific species and should be as high as possible. Simultaneously, it should be low for other species present in air that are not desired to be adsorbed [94]. Since water vapor is ubiquitous in the ambient air, it ideally should not adversely affect the adsorption process [17].
- **Loading capacity and efficiency:** The absolute capacity represents the maximum adsorbed amount of CO_2 per kilogram sorbent under specific conditions, while the working capacity refers to the difference in loading between adsorption and desorption conditions, and is lower than the absolute capacity. Efficiency is commonly used to compare different sorbents and denotes the uptake in relation to the available adsorption sites, such as amine sites, as further explained below.
- **Kinetics:** A carbon capture process benefits from fast kinetics, as higher CO_2 capture in the same time frame can enhance process efficiency and profitability [2]. However, kinetics depend not only on the sorbent itself but also on surrounding conditions like temperature, gas flow rate, and sample size and shape [79, 94].
- **Ease of regeneration:** For an efficient process, the regeneration step must be simple and energy-efficient. Lower desorption temperatures reduce energy costs and potentially allow for heat integration with renewable sources.
- **Stability:** To facilitate numerous cycles, the sorbent material must demonstrate both physical and chemical stability. Otherwise, the degradation of the support structure or the active adsorbent may lead to capacity losses [30]. Considering the DAC process, resistance to water presence and oxidation is crucial [41, 44].
- **Availability and affordability:** To make Direct Air Capture a scalable and profitable process, the sorbent must be affordable and widely available [2].

2.1.1. Amine Functionalized Sorbents

Amine-functionalized solid sorbents exhibit numerous advantageous characteristics, including chemical stability, low regeneration temperatures, high reversibility, widespread availability, and exceptional performance in humid conditions [82, 17, 94]. Consequently, they are of central focus in research for potential application in DAC [100]. Within this category, materials may vary in functionalization method, amine type, support structure, amine loading, and applied additives, providing flexibility for designing novel materials and optimizing their sorption performance. The following outlines these different characteristics and their impact.

Classification

Supported amine sorbents are usually separated into three classes [73]. The first one (class 1) includes materials with porous supports (such as silica, mesoporous materials, carbon fibers or polymers) that are impregnated with monomeric or polymeric amines by stirring the support with the amine in the organic dispersant. The impregnation binds the amines physically to the surface of the support [48, 30, 100]. The preparation of class 1 sorbents is rather simple and they tend to exhibit high amine loading and sorption capacity [30] which makes them attractive for commercial-scale DAC systems [42]. However, the binding strength of the physical bounds between amines and support is rather low, which is why the performance of these sorbents tends to decrease after multiple cycles, due to amine leaching. Another challenge is the limited diffusive transport of CO_2 molecules to the active amine sites [100, 30, 8]. The performance of the sorbent can depend, amongst other properties, on the choice of the amine type. Generally, small amines are preferred to avoid pore blockage and thus to keep the diffusion resistance low, which enables more effective mass transfer within the porous material [100].

Sorbents where amines are linked to the support structure through covalent bonds fall in class 2 [48] and are typically referred to as amine-grafted sorbents [100]. Class 3 describes adsorbents where amine-containing monomers are polymerized in situ on a porous support structure, yielding chemically grafted polyamine components. Both classes exhibit similar properites, as amine polymers are chemically attached to the support. They were developed to overcome the problem of degradation after adsorption and desorption cycles of amine-impregnated materials as they have a higher thermal stability, typically up to $200 - 250°$C [39, 11]. They typically achieve a lower sorption capacity but higher amine efficiency, as well as a better stability over consecutive cycles [30]. Furthermore, hybrid class 1/2 materials were proposed for example by Didas et al. [17].

Primary, Secondary, Tertiary and Quaternary Amines

Similar to ammonia, amine groups consist of a nitrogen atom with a lone pair and three attachments. They are distinguished in the amount of hydrogen atoms of ammonia that are replaced by substituent groups. In primary amines, one hydrogen atom is replaced, in secondary two, and in tertiary amines all three hydrogen atoms are replaced [52]. If there are four organic substituent groups attached to the nitrogen atoms, one speaks of quaternary amines or quaternary ammonium cations, as they are permanently positively charged [36]. The differences in their composition leads to differences in their binding mechanisms with CO_2. While primary and secondary amines follow the same mechanisms, tertiary and quaternary do not form carbamates, but can only bind CO_2 through the catalysis of CO_2 hydration. The chemical reactions of the formation of carbamates and bicarbonates will be explained in the following chapter. The correlation between the humidity level and CO_2 adsorption is positive for primary, secondary and tertiary amines, while it is negative for quaternary [36].

Supports

In general, sorbent materials should possess a high surface area-to-volume ratio to enable high sorption capacities.

A suitable support for sorbents should exhibit the following criteria:

1. **Large Pore Volume:** The support should have a large pore volume, facilitating high amine loading and, consequently, high sorption capacities.
2. **Uniform Amine Distribution:** A uniform distribution of amines on the support is crucial for effective sorption and must be enabled by the support structure.
3. **Strong Bond with Amines:** To ensure durability over many cycles, a robust and strong bond between the amines and the support is favorable.

4. **Resistance to Humidity:** The support should be resistant to humidity to maintain performance under varying environmental conditions.
5. **Wide Temperature Range:** A suitable support should be able to withstand a wide temperature range, making it applicable in ambient conditions [100].

For class 1 sorbents, support materials such as silica, polymers, aluminia, carbon and metal organic frameworks have been tested, where siliceous material have been most studied due to their favourable properties regarding tunability in pore structure and amine-containing ability. Moreover, they are readily available and demonstrate high thermal stability [100]. One extensively studied material is a divinylbenzene (DVB) crosslinked polymer, commercially available as Lewatit ®VP OC 1065, and functionalized with primary amines [97, 91, 9].

Amine Loading

The amine loading is a critical factor influencing the sorption capacity of a material. While it might seem intuitive that higher amine loading leads to increased capacity, this relationship only holds up to a certain point. Excessive amine loading can result in elevated diffusion resistance due to pore blockage, ultimately lowering the capacity [19, 33]. This phenomenon is particularly noticeable for class 1 sorbents. As a result, there exists an optimum amine loading that balances this trade-off, theoretically calculable through the multiplication of amine density and pore volume [12]. However, this theoretical calculation may not accurately represent the actual optimum loading, possibly due to some parts of the porous structure being inaccessible for amines. Typically, the optimum amine loading falls between 30 and 70 wt% [100]. Lou et al. [50] compared a typical silica sorbent to a sorbent with an arranged amine assembly. They found that the reduction in pore volume after vs. before the amine functionalization for the arragend assembly was lower and the sorbent kept its cylindrical pore shape. The beneficial sorption kinetics found for this sorbent indicate that the amine sites have a higher accessibility due to the arranged amine assembly.

2.1.2. Performance Measurement

The primary objectives in evaluating the performance of a sorbent include determining the adsorption isotherm and breakthrough curve. An adsorption isotherm relates the amount of adsorbed species to the concentration in the surrounding phase in equilibrium, while a breakthrough curve refers to the adsorption kinetics by monitoring the concentration at the outlet of a fixed-bed reactor over time [13]. From these two measurements, essential parameters such as capacity, adsorption time, and working capacity can be derived [94].

The breakthrough curve is commonly established through fixed-bed experiments [74, 95]. This involves measuring the concentration at the outlet of a packed bed reactor through which a feed stream is passed. "Breakthrough" occurs when the concentration surpasses a predefined value, signifying a certain degree of saturation in the sorbent material. From the breakthrough curve, the broad shape of the adsorption curve (adsorbed amount vs. time) can be derived. However, it is crucial to acknowledge that this methodology is influenced by factors like heat of adsorption, axial diffusion and adsorption isotherm [94].

For a more precise determination of adsorption curves, techniques such as thermal gravimetric analysis (TGA) are employed. TGA is a technique used to study changes in a material's weight as a function of temperature. A sample is subjected to a controlled temperature ramp in a controlled atmosphere while its weight is continuously monitored. The temperature can also be held at a certain value to obtain equilibrium data [72]. The adsorption curve provides insights into both adsorption time and capacity [94]. At the same time, TGA can give insights about the thermal stability of the sorbent.

The working capacity is typically estimated from isotherms at different temperatures [94], often obtained through volumetric or gravimetric analysis methods [28].

2.2. Adsorption Cycles

To implement Direct Air Capture effectively, a cycle capable of adsorbing CO_2 from the air and subsequently desorbing it for storage or utilization is necessary. The type of process and its design employed to achieve the capture by adsorption and desorption of CO_2 directly impact the efficiency and performance of DAC. An ideal process should maximize working capacity, which is a measure for the harvested quantity of CO_2 per cycle, while minimizing energy consumption.

Various cycles have been investigated in the past, including pressure-swing adsorption (PSA), temperature-swing adsorption (TSA) and vacuum-swing adsorption (VSA). In VSA and PSA cycles, CO_2 is adsorbed as ambient air passes through the packed bed, followed by a pressure reduction until desorption occurs [70]. TSA involves a cycle where the transition between adsorption and desorption is achieved by a temperature change; the reactor is heated after adsorption. Combinations like pressure-temperature-swing adsorption (PTSA), temperature-concentration-swing adsorption (TCSA) with an inert or CO_2 gas purge, and temperature-vacuum-swing adsorption (TVSA) are promising in order to avoid extreme pressures or temperatures. The introduction of a gas purge results in an outlet stream that may not be pure CO_2, which can be undesirable depending on the application [78]. Additionally, cycles involving a steam purge have been investigated, such as steam-assisted TSCA (S-TSCA), where the inert gas is replaced by steam [100]. Following the desorption step, steam can be easily separated from CO_2 through condensation, facilitating high purity of the CO_2 product [99]. The steps of a TVSA or S-TVSA cycle are displayed schematically in Figure 2.1.

A VSA process is not suitable for Direct Air Capture, as the desorption requires impractical low pressures [99]. Elfving et al. [21] found that within realistically achievable pressure bounds, it is not possible to achieve an equilibrium working capacity higher than $0.5\,\mathrm{mmol_{CO_2}/g_{sorbent}}$ with a PSA process, while exceeding $0.7\,\mathrm{mmol_{CO_2}/g_{sorbent}}$ for TSA. Bos et al. [9] also reported impractically low working capacities in the PSA cycle. Comparisons of TSA and TVSA processes [21, 51, 78] showed that TSA leads to higher equilibrium working capacities ($+13\%$ [78]), but TVSA exhibits a lower energy penalty. As an effective desorption in TSA required $25\,\mathrm{min}$ at $120\,^{\circ}\mathrm{C}$ or in VSA $30\,\mathrm{min}$ at $0.145\,\mathrm{bar}$, but only $7.5\,\mathrm{min}$ at $120\,^{\circ}\mathrm{C}$ and $0.145\,\mathrm{bar}$ in a TVSA cycle [51], TVSA is advantageous regarding consumed energy, cycle time, and thus productivity. Additionally, Elfving et al. found that the CO_2 at the outlet is more pure in TVSA [21]. The introduction of a steam purge during the desorption step (S-TVSA) provides an additional pressure swing through purge by displacement. Steam enters the reactor at the desorption temperature and evacuation pressure [83]. As the temperature can be rather low in this process, solar energy or waste heat can be used for the supply [100]. This makes S-TVSA a very promising process for application in DAC [99].

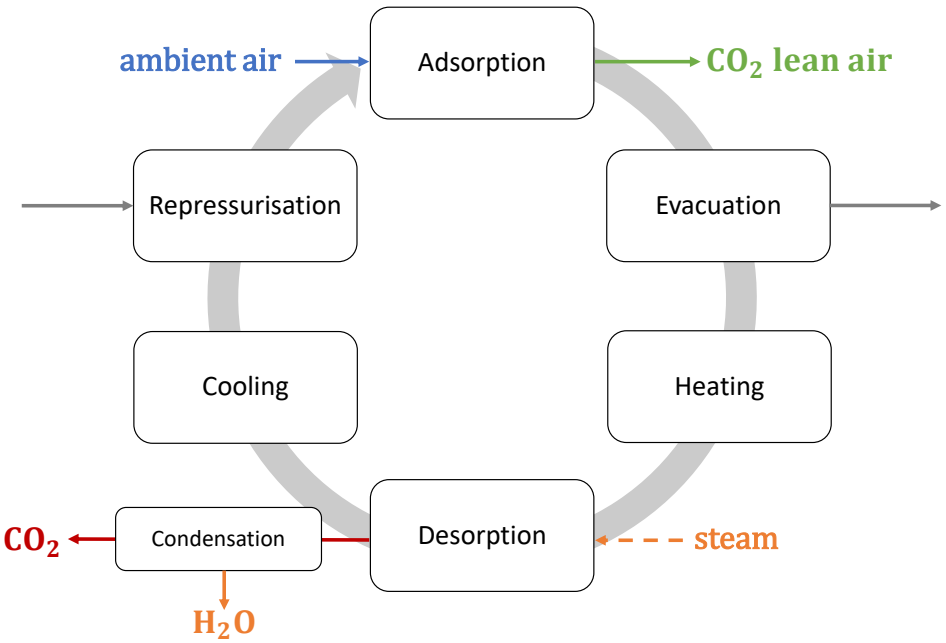

Figure 2.1: Schematics of a TVSA or S-TVSA cycle

2.3. Modeling Approaches in Literature

Models in literature representing the adsorption reactions can be classified in isotherm and kinetic models. An adsorption isotherm relates the amount of adsorbent in the surrounding phase to the adsorbate adsorbed to the sorbent and thus describes the sorption behaviour in equilibrium, while the kinetics refer to the dynamic uptake behaviour.

In the case of CO_2 adsorption on amine functionalised sorbents, the adsorption phenomena differ depending on whether water is present or if the system is in dry conditions. In dry conditions, CO_2 is bound to the amine through the formation of a carbamate. The chemical adsorption mechanisms extend in the presence of water from only the formation of carbamates to the additional formation of bicarbonates. The difference in the stoichiometric relations of the two reactions lead to different amine efficiency in dry and humid conditions ($\Phi = 0.5$ for carbamate and $\Phi = 1$ for bicarbonate) leading to an overall higher CO_2 adsorption capacity in the presence of water. The adsorption of CO_2 in dry conditions is typically modeled with a Toth model [28], while pure water adsorption is well described by the Guggenheim-Anderson-de Boer (GAB) isotherm [95, 65, 87]. Several different isotherm models for the co-adsorption of CO_2 and H_2O have been introduced. Stampi-Bombelli [83] develop an empirical model of an adjusted Toth isotherm to describe the effects occurring. Jung et al. [35] as well as Elfving et al. [21] propose kinetic approaches to predict the equilibrium behaviour. Young et al. [97] propose two models; a mechanistic and a weighted average dual site Toth (WADST) co-adsorption model. Kaneko and Lackner [36] introduce a generalized model that can be applied to primary, secondary, tertiary as well es quaternary amines. Details of the different models are presented in Section 7.

Previous kinetic models made use of various driving force models, where relationships between the current and the equilibrium CO_2 loading are approximated. Examples are the pseudo first- and second-order linear driving force models, Avrami's model [79], or the Toth rate equation [9]. These models do not explicitly model intra-particle mass transfer, which is why kinetic constants include the effects of mass transfer as well as reaction kinetics. Ge et al. developed a dynamic model to describe the mass transfer processes of the adsorption of CO_2 on an amine impregnated mesoporous silica on a particle scale [27]. They include different mass transfer phenomena in the particle, such as film diffusion, pore diffusion, surface diffusion and chemical reaction. Ge et al. solely focus on dry conditions, not regarding the effects of co-adsorption. Lee et al. [45] model the kinetic reactions of carbamate and bicarbonate formation under the assumption of negligible intra-particle mass transfer. Suh and San extend the model considering pore diffusion and chemical reactions under dry as well as under humid conditions [86]. They however disregard desorption conditions as well as multi-component mass transfer.

3

Model description

In a typical solid sorbent DAC system, the air passes through a packed bed reactor of porous particles, consisting of an amine functionalized material. In the process until adsorption and saturation of the material, several mass transfer mechanisms play a role [27, 86]. The numerical model of this work consists of a diffusion-reaction model on the scale of one particle of a sorbent, which is then included in a contactor model. Due to the dilute conditions of CO_2 in air, large volumes of air must be processed in the contactor to capture a substantial amount of CO_2. While the contactor typically utilized is a packed bed, other structures such as monolith have gained attention for the application in DAC [84, 89]. Monoliths offer the advantage of a low pressure drop, which decreases the electrical energy of the fan required to blow the air through the contactor. Hence, examples of a packed bed reactor and a monolith are considered in this study. For modeling the monolith, the particle-scale model is adjusted to cartesian coordinates, modeling the penetration of the gas phase into the wall. In this chapter, the setup of the particle-scale model is described, followed by an explanation of the contactor models.

3.1. Particle-scale model

Before CO_2 can be adsorbed, the air is transported from the bulk towards and into the particle, through the pores and to the surface of the amine functionalized sorbent. During desorption, CO_2 and H_2O detach from the sorbent, diffuse away from the amine layer and exit the particle. This transport process is governed by various mass transfer mechanisms, each potentially prolonging the adsorption or desorption steps of the process. Therefore, a comprehensive understanding of mass transfer phenomena within the system and its associated constraints is crucial.

The mass transfer in porous materials can be divided in external and internal mass transfer. The connection between different mass transfer phenomena is commonly represented by a resistor network model [37] (see Figure 3.1). External mass transfer includes all transfer steps relevant outside the porous particle, such as a flow through a reactor or the diffusion in the boundary layer of a particle. Inside the porous system, mass transfer can occur through the following mechanisms:

1. **Viscous Flow** When a pressure gradient exists along the pore, bulk flow occurs following Poiseuille's law. The contribution of this flow to the overall mass transfer can be quantified using a diffusion coefficient derived from Poiseuille's law.

   $$D_{vis} = \mathrm{Pr}^2/8\mu \tag{3.1}$$

   Viscous flow occurs simultaneously to diffusive contributions and will thus add to the mass transfer rate.

   $$D_{tot} = D_{vis} + D \tag{3.2}$$

2. **Molecular Diffusion** The effect is also called bulk-diffusion and describes the phenomenon of inter-molecular collisions. These become relevant when the diffusing gas contains multiple species, and the pore size is big in relation to the molecule's mean free path, which makes molecule-wall collisions negligible over molecule-molecule interactions.

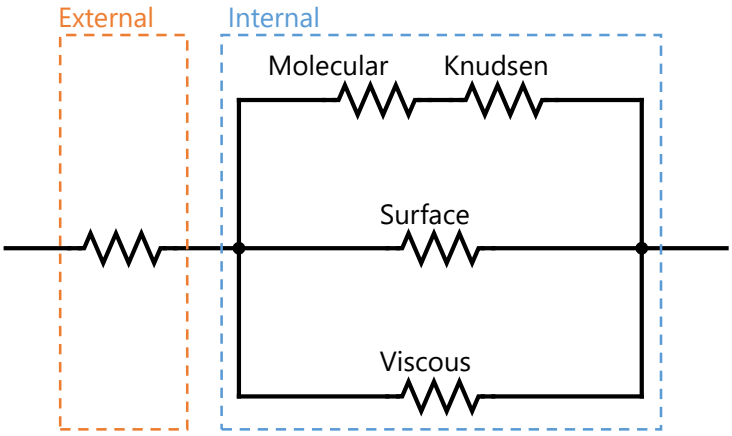

Figure 3.1: Resistor network model of the mass transfer processes [37].

3. **Knudsen Diffusion** When the pore size is smaller than the mean free path of the gas molecules, molecule-wall interaction becomes the dominating effect. This tends to occur in small pores and at low pressures [37, 40]. In the transition to higher pressure or larger pore size, when the pore size is of similar size as the mean free path, Knudsen diffusion and molecular diffusion both occur simultaneously [37]. In order to determine whether Knudsen or molecular diffusion is dominant, the Knudsen number Kn is defined as the ratio of the mean free path of the diffusing species and the pore diameter [13].

$$\mathrm{Kn} = \frac{\lambda}{d_p} \tag{3.3}$$

For the mean free path of gases the relation

$$\lambda = \frac{4k_B T}{\pi \sigma^2 p} \tag{3.4}$$

holds, where σ is the collision diameter of the species. If the Knudsen number is small ($\mathrm{Kn} \ll 1$), molecular diffusion is dominant, while Knudsen diffusion becomes relevant at high values ($\mathrm{Kn} \gg 1$).

4. **Surface Diffusion** When the molecule does not leave the force field of the solid pore wall, so the molecules diameter is of similar size as the pore diameter, the dominant phenomenon of diffusion is described as surface diffusion or microporous diffusion, or for zeolitic materials as configurational diffusion. It can occur in parallel to molecular and Knudsen diffusion and can have a significant impact on the total diffusion rate [40]. In the case of physical adsorption of the diffusive species, the molecules are highly mobile. If the molecules adsorb chemically their adsorption energy is greater which makes them less mobile. However, they can still move through the adsorbate [13]. This is often described by hopping mechanisms from one to the next site, or Fickian models [54]. Hopping mechanism models consider distinct sites with energy barriers between them that a molecule needs to overcome in order to move from one to the other. Fickian models define surface diffusion as the excess mass transfer of bulk diffusion, and split the diffusion flux in two parts, accordingly:

$$J_{tot} = J_b + J_s. \tag{3.5}$$

The surface diffusion flux J_s is quantified by subtracting the bulk diffusion J_b from the total mass transfer. This leads to an overestimation of the surface diffusion, as the possibility of desorption, bulk diffusion and re-adsorption is not included [54].

As the regime transitions between Knudsen and molecular diffusion depending on the conditions, these are displayed in series in the resistor model, while surface diffusion and viscous flow can independently add to the mass transfer and are thus in parallel to the other two.

The mass transfer phenomena occuring around one single particle are presented in Figure 3.2. The species diffuse from the bulk through the film that is surrounding a particle, where the dominant mechanism is molecular diffusion. After diffusing through the film and reaching the particle, some molecules

will be adsorbed on the surface. With rising CO_2 concentration in the solid phase, other molecules travel inwards the particle, where mass transfer is governed by molecular diffusion or Knudsen diffusion depending on pore size, pressure and temperature. Inside the pores of the particle, more molecules will adsorb to the surface by physical adsorption or chemical reactions. After adsorption, surface diffusion in the solid structure might still occur.

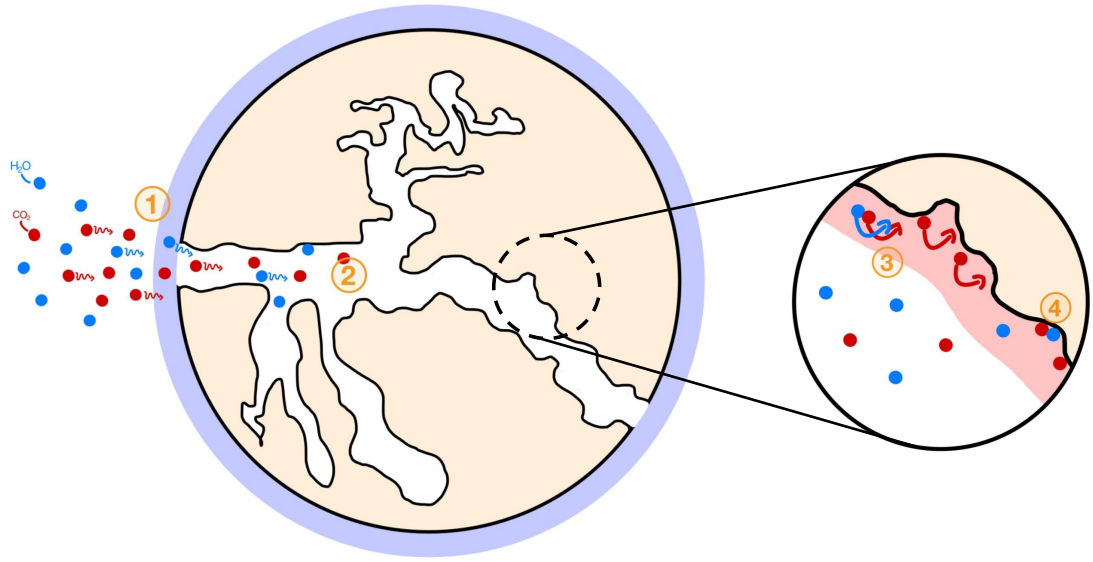

Figure 3.2: Schematics of a porous particle and relevant mass transfer processes during adsorption, (1) film diffusion, (2) pore diffusion, (3) surface diffusion, (4) chemical reaction

3.1.1. Parametrization of pore structures

Porous sorbents inherently possess a complex structure. To facilitate quantitative comparison and description, various parameters have been established, as summarized in Table 3.1 and further explained in this section.

Table 3.1: Parameters describing porous sorbents

Symbol	Unit	Meaning
ρ_b	kg/m^3	bulk density
ρ_p	kg/m^3	particle density
ε	-	porosity
$D_{p,eq}$	m	equivalent particle diameter
τ_p	-	Tortuosity
S_{BET}	m^2/g	BET surface area
d_p	m	average pore diameter
V_p	m^3/g	pore volume
$f(r)$	m	BJH pore size distribution

Porosity describes the ratio between voids, i.e. pore volume in a solid, and the solids total volume. It is often expressed as a fraction and can be calculated as

$$\varepsilon = \frac{V_v}{V_t}, \tag{3.6}$$

where V_v is the void volume and V_t is the total volume [49]. The porosity can be defined for the porous material itself (ε_p) as well as for a packed bed of particles (ε_b) The bulk density refers to the density that

the porous material typically assumes when placed in a container. Therefore, it encompasses the voids between the particles as well as the pores within the individual particles. However, the bulk density can vary based on surrounding conditions and the duration that the material (e.g., powder) has been settling in the container [62]. The particle density or sorbent density describes the density of a single particle and is defined by the ratio of the particle's mass (m_p) to its volume (V_p), including the voids due to pores:

$$\rho_s = \frac{m_p}{V_p}. \tag{3.7}$$

The bulk density and particle density are related by the void fraction of the bed, denoted as ε_b, according to the equation:

$$\rho_b = \rho_s \left(1 - \varepsilon_b\right). \tag{3.8}$$

Considering that particles are typically not perfectly spherical and can have different shapes, the diameter commonly referred to is an equivalent diameter. This is defined as the length of a line bisecting an image of the particle [62].

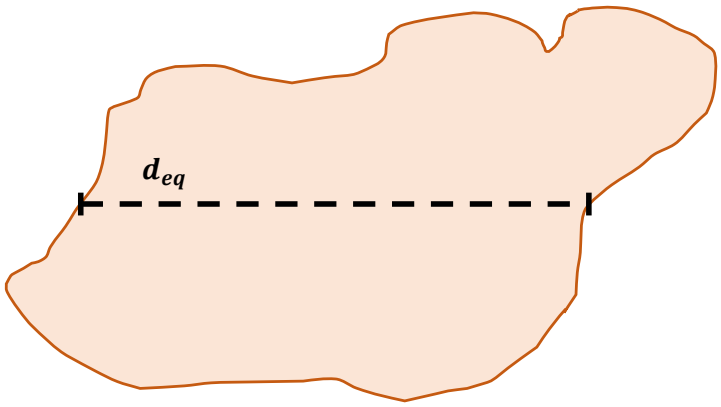

Figure 3.3: Equivalent diameter for an arbitrary particle [62].

The tortuosity relates the length of the porous medium to the average length of a pore, and thus accounts for the additional path length thought the medium [55]. The pores are considered as sinusoidal but parallel pores with an average length. Tortuosity is defined as the ratio of the average pore length L_e and the length of the porous solid L [22];

$$\tau_p = {}^{L_e}/_{L}. \tag{3.9}$$

It is $\tau_p > 1$ as $L_e > L$, for perfectly cylindrical pores the tortuosity would equal 1.

The specific surface area gives the ratio of total surface area to mass or volume of the porous material. A well established method of determining that value is a gas adsorption measurement proposed by Stephen Brunauer, Paul Hugh Emmett, and Edward Teller and is referred to as the BET method [49]. The method is based on the measurement and analysis of an adsorption isotherm, typically conducted with nitrogen at low temperatures and can measure specific surface areas in the range of $0.001 - 1000\,\mathrm{m^2/g}$. From the results of the BET method, an equivalent pore diameter d_p can be determined. In order to characterize pore sizes and pore size variations of a material, the Barrett - Joyner - Halenda (BJH) pore size distribution is commonly given [3].

3.1.2. Assumptions

For the development of the model, the material Lewatit ®VP OC 1065 (in the following referred to as Lewatit) is considered. It consists of sphere-like particles, with effective sizes ranging between $300\,\mathrm{mm}$ and $1250\,\mu\mathrm{m}$, the average (by particle volume) effective particle diameter being $D_{p,eff} = 520\,\mu\mathrm{m}$ [46, 97]. The average pore diameter results from the BET surface area as explained and is given by the manufacturer as $d_{p,avg} = 57\,\mathrm{nm}$. Veneman et al. and Young et al. [91, 97] measure the density of a single particle to be $\rho_s = 880\,\mathrm{kg/m^3}$ and estimate a particle voidage of $\varepsilon_s = 0.238$ with a tortuosity of $\tau_p = 2.3$. The material contains primary amines (benzyl amines) [1], the loading of which can be estimated from the nitrogen loading, which was measured to be $q_{am} = 6.7\,\mathrm{mol/kg}$ by Alesi and Kitchin [1]. The concentration of amines over the particle volume is calculated from the amine loading and the particle density, and is found to be $C_{am,p} = 5896\,\mathrm{mol/m^3}$. In this model, the particle is assumed to be spherical with a diameter of the effective particle size $D_{p,eff}$ and a pore size equal to the average pore size $d_{p,avg}$. For adjustment to the application in the monolith, the same material parameters are assumed. The conditions over the domain are assumed to be isobaric and isothermal, and the ideal gas law is applied for the gas phase. The model considers film diffusion, pore diffusion due to molecular diffusion as well as Knudsen diffusion and the chemical reaction kinetics. Surface diffusion is not included in the model, as it is assumed to be not rate limiting. This assumption is made after the work of Ge et al. [27] and estimations of the magnitude of surface diffusion in radial direction in the particle which can be found in the Appendix 8 of this work.

3.1.3. Species balance equation

To evaluate the mass transfer over one particle, a balance for each species i is drawn. The balance is drawn in terms of concentration and reads for each diffusing species i

$$\frac{\rho}{M_i}\frac{\partial y_i}{\partial t} = \frac{\partial C_i}{\partial t} = \frac{\nabla \cdot J_i}{M_i} + G_i \tag{3.10}$$

ρ is the local density of the gas phase in $\mathrm{kg/m^3}$, y_i the mass fraction, C_i the concentration in the particle in $\mathrm{mol/m^3}$ and J_i denotes its flux in $\mathrm{kg/s\,m^3}$. G_i is the generation term due to adsorption and its calculation is described in Section 3.1.8.

The adsorbed species in the material do not diffuse, so the balance equation reads

$$\frac{\partial C_i}{\partial t} = G_i. \tag{3.11}$$

The concentrations used in the calculations refer to the whole control volume, i.e. the particle volume or the volume of the wall increment. The total concentration in the particle can be determined as

$$C_{tot} = \varepsilon_s \cdot C_{gas} + (1 - \varepsilon_s) \cdot C_{ads,s}, \tag{3.12}$$

where the gas concentration is found with the ideal gas law, and the concentration of the adsorbed phase refers to the solid volume of the particle. The concentration of the adsorbed phase is the sum of all concentrations of immobile species on the solid phase.

$$C_{ads,s} = C_{am,s} + C_{pr,s} + C_{cm,s} + C_{H2O,ads,s} + C_{bi,s} \tag{3.13}$$

The gas concentrations per particle volume are found with the ideal gas law and the porosity of the particle,

$$C_{gas} = \frac{P}{RT} \quad \text{and} \quad C_{\mathrm{CO_2}} = \varepsilon_s \cdot x_{\mathrm{CO_2}} C_{gas} \tag{3.14}$$

and the concentrations of the adsorbed phase per particle volume are calculated as

$$C_{am} = (1 - \varepsilon_s) \cdot C_{am,s} \tag{3.15}$$

From this, the molar fractions of the total domain can be calculated

$$x_i = \frac{C_i}{C_{tot}} \tag{3.16}$$

where the concentrations are with respect to the whole volume of the particle.

The species mass fraction is then

$$y_i = \frac{x_i M_i}{M}, \tag{3.17}$$

where $M = \sum_i x_i M_i$ for $i = \mathrm{CO_2}, \mathrm{H_2O}, am, pr, cm, \mathrm{H_2O_{ads}}, bi$.

The CO_2 loading on the material is calculated from integrating the concentration of adsorbed species containing CO_2 over the particle, and dividing it by the mass of one particle.

$$\frac{\partial N_{\mathrm{CO_2},p}}{\partial t} = 4\pi \int_0^{\frac{D_p}{2}} \left(\frac{\partial C_{cm}}{\partial t} + \frac{\partial C_{bi}}{\partial t} \right) \cdot r^2 dr \tag{3.18}$$

$$m_p = \frac{4}{3}\pi \left(\frac{D_p}{2} \right)^3 \rho_p \tag{3.19}$$

where ρ_p is the density of the particle.

In the case of modeling an increment of the monolith wall instead of a particle, the model is adjusted to cartesian coordinates. The total number of moles adsobed in the control volume is then

$$\frac{\partial N_{\mathrm{CO_2},w}}{\partial t} = dh \cdot b_1 \int_0^{\frac{dw}{2}} \left(\frac{\partial C_{cm}}{\partial t} + \frac{\partial C_{bi}}{\partial t} \right) dx \tag{3.20}$$

$$m_w = dh \cdot b_1 \cdot \frac{dw}{2} \rho_w \tag{3.21}$$

where dh, b_1 and $dw/2$ are the dimensions of the wall increment, and ρ_w is the density of the porous wall, which is equivalent to the particle density ρ_p. The loading per mass sorbent is then

$$\frac{\partial q_{\mathrm{CO_2},p}}{\partial t} = \frac{1}{m_p} \frac{\partial N_{\mathrm{CO_2},p}}{\partial t} \tag{3.22}$$

for the particle or

$$\frac{\partial q_{\mathrm{CO_2},w}}{\partial t} = \frac{1}{m_w} \frac{\partial N_{\mathrm{CO_2},w}}{\partial t} \tag{3.23}$$

for a wall increment of the monolith.

3.1.4. Diffusion equation

To calculate the diffusive fluxes J, two models are implemented and compared. The first model makes use of Fick's law of diffusion, while the second model includes multicomponent effects and is based on the Maxwell-Stefan equations, implemented in the dusty gas model. The diffusion coefficients for the continuum diffusion are calculated by the correlation for binary diffusion coefficients [26]

$$D_{ij} = \frac{10^{-7} T^{1.75} \left(\frac{1}{M_i} + \frac{1}{M_j} \right)^{0.5}}{P \left[\left(\sum V_i \right)^{\frac{1}{3}} + \left(\sum V_j \right)^{\frac{1}{3}} + \right]^2}. \tag{3.24}$$

T is the temperature in K, M_i and M_j the molar masses of the species in $\mathrm{kg/mol}$, P the total pressure in atm and V_i and V_j the diffusion volumes of the respective species. For CO_2, H_2O and N_2 the values are given as 26.9, 12.7 and 17.9, respectively [26]. The diffusion coefficient for Knudsen diffusion can be derived from the kinetic theory [37]

$$D_{\mathrm{Kn}} = \frac{d_p}{3} \sqrt{\frac{8RT}{\pi M_i}}, \tag{3.25}$$

where d_p denotes the pore diameter, R the universal gas constant, T the temperature and M_i the molecular mass of the diffusing species i. In a transition region, where both Knudsen diffusion and molecular

diffusion are relevant, the overall diffusion coefficient for the Fickian model can be calculated according to [37]

$$\frac{1}{D_{tot}} = \frac{1}{D_m} + \frac{1}{D_{\mathrm{Kn}}}. \tag{3.26}$$

The exact morphology of porous materials is arbitrary and and difficult to describe. The most simple model is a straight, cylindrical pore, which is usually far from reality. Pore sizes can vary, and the structure might be hierarchical, with interconnecting pores and channels smaller than the gas molecules. To represent the hindering of mass transfer in the pore structure, the diffusion coefficients are adjusted by accounting the porosity and tortuosity of the particles [58]:

$$D^e = \frac{\varepsilon_s}{\tau_p} D. \tag{3.27}$$

Fick's law of diffusion

Fick's law of diffusion is widely accepted and applied for various diffusion problems. It relates the diffusive flux of a species $\mathbf{J}_i$ $[\mathrm{mol}/\mathrm{m}^2\,\mathrm{s}]$ linearly to the gradient of its concentration C_i $[\mathrm{mol}/\mathrm{m}^3]$, with the total (3.26), effective diffusion coefficient D_i $[\mathrm{m}^2/\mathrm{s}]$ [13]:

$$\mathbf{J}_i \equiv -D_i \nabla C_i. \tag{3.28}$$

The second law describes how the concentration changes with respect to time:

$$\frac{\partial C_i}{\partial t} = D_i \nabla \cdot (\nabla C_i)\,. \tag{3.29}$$

However, Fick's law is only valid for binary, ideal mixtures or multicomponent mixtures with dilute species [13]. Depending on the conditions in ambient air, this might be given for the adsorption process. During desorption however, carbon dioxide and water are present in non-dilute conditions to each other. Consequently, relying solely on Fick's law to describe the process may lead to inaccuracies.

Maxwell-Stefan equations and the dusty gas model

The Maxwell-Stefan equations offer a general approach for the description of diffusion problems [40]. The equations originate from the consideration of the mechanics of molecular collisions between the involved species. Therefore the force exerted on a molecule of a species is set equal to the friction between that and the other present species. The sum of momentum exchange thus depends on the amount of momentum exchanged per collision and the number of collisions per unit volume.

Considering a binary mixture, the momentum transferred from a molecule of species 1 is proportional to the velocity of molecule 1 and the velocity of molecule 2 $(\mathbf{v}_1 - \mathbf{v}_2)$. The number of collisions per unit volume and unit time depends on the number of molecules present and is thus proportional to the molar fractions of the species x_i. Accordingly, the driving force of diffusion has to be equal to these terms and a proportionality factor f_{12} [37].

$$\mathbf{d}_1 = -f_{12} x_1 x_2 \left(\mathbf{v}_1 - \mathbf{v}_2\right) \tag{3.30}$$

Maxwell and Stefan establish this proportionality factor by defining the Maxwell-Stefan diffusion coefficient D_{12} which is equivalent to an inverse drag coefficient.

$$\mathbf{d}_1 = -\frac{x_1 x_2 \left(\mathbf{v}_1 - \mathbf{v}_2\right)}{D_{12}} \tag{3.31}$$

It is important to note that the Maxwell-Stefan diffusion coefficient matrix is symmetrical, thus it holds that $D_{12} = D_{21}$ [88]. To get a more useful form of the equation the diffusion fluxes **J** are introduced, which eliminates the molecular velocities:

$$\mathbf{d}_1 = \frac{\left(x_2 \mathbf{J}_1 - x_1 \mathbf{J}_2\right)}{c_t D_{12}} \tag{3.32}$$

where c_t is the total concentration.

To treat multicomponent systems, the equations can be extended as follows

$$\mathbf{d}_i = -\sum_{j=1}^{n} \frac{(x_j \mathbf{J}_i - x_i \mathbf{J}_j)}{c_t D_{ij}}. \tag{3.33}$$

$\mathbf{d}_i$ is the driving force for diffusion of species i at constant temperature and pressure. For non-ideal fluids it is defined with the chemical potential μ_i as

$$\mathbf{d}_i \equiv \frac{x_i}{RT} \nabla_{T,P}\, \mu_i \tag{3.34}$$

and for ideal gas mixtures

$$\mathbf{d}_i = \nabla x_j. \tag{3.35}$$

To model Maxwell-Stefan diffusion in a porous system, the Dusty-Gas Model (DGM) is a convenient choice. It can incorporate different mass transfer mechanisms such as continuum diffusion, Knudsen diffusion and viscous flow [16, 58]. The dusty gas model is based on the principle of adding a species of big 'dust' particles representing the porous structure. The central equation reads

$$\sum_{\substack{j=1 \\ j\neq i}}^{j=N} \underbrace{\frac{x_j x_i \mathbf{v}_i - x_i x_j \mathbf{v}_j}{D_{ij}^e}}_{\substack{\text{Maxwell-Stefan} \\ \text{equations}}} + \underbrace{\frac{x_i}{D_{iK}^e}\mathbf{v}_i}_{\substack{\text{Knudsen} \\ \text{flow}}} + \underbrace{\frac{x_i}{D_{iK}^e}\frac{B_0}{\mu}\nabla P}_{\substack{\text{Viscous} \\ \text{flow}}} = \underbrace{-\nabla x_i - \frac{x_i}{P}\nabla P}_{\substack{\text{Driving force of} \\ \text{continuum diffusion}}}, \tag{3.36}$$

where B_0 is a characteristic of the pore structure, x denotes the mole fraction of a species, $\mathbf{v}_i$ the diffusion velocity and D_{ij}^e and D_{iK}^e are the effective binary diffusion coefficient (also referred to as Maxwell-Stefan diffusion coefficient) and the effective Knudsen diffusion coefficient. They are adjusted to the pore structure through the porosity ε_s and tortuosity τ_p. In this work, it is assumed that there is no pressure gradient over the regarded particle [27], thus viscous flow is not of relevance and will not be considered. This assumption reduces the equation to

$$\sum_{\substack{j=1 \\ j\neq i}}^{j=N} \underbrace{\frac{x_j x_i \mathbf{v}_i - x_i x_j \mathbf{v}_j}{D_{ij}^e}}_{\substack{\text{Maxwell-Stefan} \\ \text{equations}}} + \underbrace{\frac{x_i}{D_{iK}^e}\mathbf{v}_i}_{\substack{\text{Knudsen} \\ \text{flow}}} = \underbrace{-\nabla x_i}_{\substack{\text{Driving force of} \\ \text{continuum diffusion}}}, \tag{3.37}$$

From this, the flux-diffusion matrix Γ which is later applied to determine the diffusive flux is calculated. Equation 3.37 can be written in matrix form as

$$\sum_j F'_{ij} \mathbf{v}_j = -\nabla x_i, \tag{3.38}$$

with

$$F'_{ij} = \begin{cases} \sum_{l\neq i} \frac{x_i x_l}{D_{il}^e} + \frac{x_i}{D_{iK}^e} & \text{if } i = j \\ -\frac{x_i x_j}{D_{ij}^e} & \text{if } i \neq j \end{cases}. \tag{3.39}$$

The equation is transformed to mass fractions instead of mole fractions by using a conversion matrix $\tilde{\mathbf{M}}$, defined by [63]:

$$\nabla x_i = \sum_j \tilde{M}_{i,j} \nabla y_j. \tag{3.40}$$

It is defined as

$$\widetilde{M}_{ij} = \begin{cases} \frac{M}{M_i}\left(y_i - x_i + \sigma\right) & \text{if } i = j \\ M\left(\frac{y_i}{M_i} - \frac{x_i}{M_j}\right) & \text{if } i \neq j \end{cases}. \tag{3.41}$$

where $\sigma = \sum_i y_i \equiv 1$.

To express the Maxwell-Stefan equations in the flux form, matrix $\mathbf{H'} = \mathbf{F'}\,\mathbf{R}^{-1}$ with $\mathbf{R} = \text{diag}(\rho y_i)$ is defined:

$$H'_{ij} = \begin{cases} \sum_{l \neq i} \frac{\sigma M}{\rho M_i}\left(\frac{x_l}{D^e_{il}}\right) + \frac{\sigma M}{\rho M_i D^e_{iK}} & \text{if } i = j \\ -\frac{\sigma M}{\rho M_j}\frac{x_i}{D^e_{ij}} & \text{if } i \neq j \end{cases}. \tag{3.42}$$

Now, the equation can be expressed as

$$\sum_j H'_{ij}\mathbf{J}_j = -\sum_j \tilde{M}_{ij}\nabla y_j, \tag{3.43}$$

and total flux for species i is then

$$\mathbf{J_i} = \frac{1}{M_i}\sum_j -\Gamma_{ij}\nabla y_j \tag{3.44}$$

with $\mathbf{\Gamma} = \mathbf{H'}^{-1}\tilde{\mathbf{M}}$.

When this model is incorporated in a mass balance with a source term like Equation 3.10, the model definitions require that the sum of the source terms (in this case due to chemical reaction) is equal to zero. Thus, all involved species, including the adsorbed phase, are considered.

In order to validate the implementation of the model, the same isobaric test case as described in Mousavi et al. [58] was replicated. The fluxes calculated in this work matched the numerically and experimentally [66] determined ones, which makes the model suitable to be applied in the further proceedings.

3.1.5. Solution

The partial differential equations describing the system, are solved by the application of the Method Of Lines (MOL) [76]. Herein, spatial discretization and approximation is applied to replace the spatial derivatives of the Partial Differential Equations (PDEs). Thus, the problem is transformed to a system of Ordinary Differential Equations (ODEs) and solved for time as the independent variable. The discretization methods and boundary conditions used in this work are explained in the following.

The resulting system of ODEs is solved in `Python` with the module `SciPy` [92], applying the solver `solve_ivp`. The method `LSODA` was found to be most efficient for the problem of this work.

The particle scale model exhibits mesh-independece from a resolution of 40 gridpoints. The particle-scale cases were ran with 100 gridpoints to ensure mesh independence through all conditions.

3.1.6. Discretization

The mass balance is spatially discretized using central differences [25]. The particle is assumed to be symmetric, and the balance in radial direction reads

$$\left(\frac{\partial C_i}{\partial t}\right)_k = \left[\frac{1}{r^2}\frac{\partial}{\partial r}\left(r^2 J_i\right)\right]_k + \left(G_i\right)_k \tag{3.45}$$

where k is the spatial index in radial direction. In the following, the index i describing the species is left out for simplicity. The flux needs to be evaluated at the boundaries of the cells $r = r + {}^{\Delta r}/_2$ and $r = r - {}^{\Delta r}/_2$, so that the diffusive term can be calculated. To calculate the flux, central differences are applied as well, so that $J_{k+0.5}$ is dependent on the gridpoints k and $k+1$.

$$\left[\frac{1}{r^2}\frac{\partial}{\partial r}\left(r^2 J\right)\right]_k \approx \left[\frac{1}{r_k^2}\left(\frac{r^2_{k+0.5}J_{k+0.5} - r^2_{k-0.5}J_{k-0.5}}{\Delta r}\right)\right] \tag{3.46}$$

When using Fick's law, the flux becomes

$$J_{k+0.5} = -D^e \frac{C_{k+1} - C_k}{\Delta r}, \tag{3.47}$$

while Maxwell-Stefan's law depends on a flux diffusion matrix Γ, and the flux is then calculated with

$$J_{j,k+0.5} = \frac{1}{M_j} \sum_j -\Gamma_{i,j} \frac{y_{j,k+1} - y_{j,k}}{\Delta r}. \tag{3.48}$$

The discretization for the model of the wall increment follows the same schemes, and is adjusted to cartesian coordinates.

3.1.7. Boundary and initial conditions

At the center of the particle ($r = 0$) or the mid-point of the monolith wall ($x = 0$), a non-gradient boundary condition is applied due to assumed symmetry. Thus, the flux at the boundary is set to zero.

$$J_{j,k=-0.5} = 0. \tag{3.49}$$

At the interface of the sorbent to the surrounding gas, a boundary condition is given that represents the mass transfer from the bulk to the surface, $i.e.$ film diffusion. A mass transfer coefficient h which represents the convective effects is calculated. For the packed bed reactor the correlation

$$\mathrm{Sh} = \frac{D_p \cdot h}{D_m} = 2.0 + 1.1 \mathrm{Sc}^{1/3} \mathrm{Re}^{0.6} \tag{3.50}$$

is used, for the monolith

$$\mathrm{Sh} = \frac{D_p \cdot h}{D_m} = 2.696 \left(1 + 0.139 \left(\frac{b_1}{L}\right) \mathrm{Re}\,\mathrm{Sc}\right)^{0.81} \tag{3.51}$$

is applied [67]. D_m represents the molecular diffusion coefficient of the respective species, D_p is the diameter of the particle. The Schmidt number and the Reynolds number are calculated according to Equation 3.73. The concentration gradient at the boundary is defined as

$$\left(\frac{\partial C}{\partial r}\right)_{r=D_p/2} = \frac{h}{D_m}(C^\infty - C_{r=R}), \tag{3.52}$$

When external mass transfer is not considered, a constant value condition can be applied, which assumes the concentration of the ghost cell outside the particle to be equal to the bulk concentration. For the model of the monolith wall, only the spatial variable r and thus Δr are exchanged with x and Δx.

For the initial conditions, the gas phase concentration in the particle is assumed to be zero. The initial conditions of the adsorbed species are case dependent and given in Table 3.3

3.1.8. Chemical reaction

In elucidating the mechanisms underlying Direct Air Capture (DAC) technology, understanding the binding mechanisms of CO_2 on amine groups is crucial. Thus, the main chemical reactions are explained in the following. To illustrate the chemical reactions, the example of primary amines is used [36].

Depending on the humidity level of the air and the type of amines, carbamates and bicarbonates are formed [60]. When no water molecules are present, CO_2 is chemically adsorbed by the formation of carbamates as shown in Figure 3.4, where carbamic acid is formed in the first step:

$$CO_2 + RNH_2 \longleftrightarrow RNHCOOH, \tag{3.53}$$

and can split into a proton and a carbamate as:

$$RNHCOOH \longleftrightarrow RNHCOO^- + H^+. \tag{3.54}$$

To be stabilized, the resulting proton reacts with another amine:

$$H^+ + RNH_2 \longleftrightarrow RNH_3{}^+ \tag{3.55}$$

Through these reactions, an ammonium carbamate ion pair is formed and the overall reaction is

$$CO_2 + 2\,RNH_2 \longleftrightarrow RNH_3{}^+ + RNHCOO^-. \tag{3.56}$$

As one amine group is needed to bind the CO_2 and one to stabilize the produced proton, two amine sites are used for the adsorption of one CO_2 molecule in total. Hence this adsorption route gives an amine efficiency of $\Phi = 0.5$, with the amine efficiency being defined as the quantity of adsorbed CO_2 molecules per amine site.

The presence of water introduces another reaction that can occur alongside the formation of carbamates and leads to the formation of bicarbonates. This occurs by:

$$RNH_2 + H_2O + CO_2 \longleftrightarrow RNH_3{}^+ + HCO_3{}^-. \tag{3.57}$$

Consequently, the amine efficiency of the formation of bicarbonates is $\Phi = 1$, as only one amine site is required to bind one CO_2 molecule. This highlights how the presence of water in the adsorption process can be beneficial, as a higher amine efficiency leads to a higher adsorption capacity.

The displayed reactions can occur both for primary as well as for secondary amines. It is important to note that for tertiary amines, the formation of carbamates as described above does not occur. Thus, for the adsorption on tertiary amines the presence of water is necessary [36].

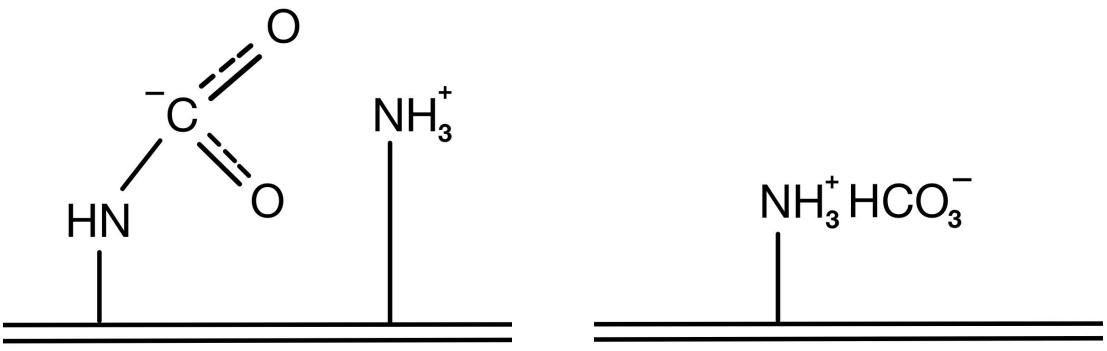

(a) absence of water: carbamate **(b)** presence of water: carbonate

Figure 3.4: Species forming in the different binding mechanisms in dry and humid conditions [97]

It should be noted that the mechanisms of CO_2 adsorption in humid conditions is still topic of current research and other routes have been proposed. Li et al. [47] propose that the formation of bicarbonates

is rather unlikely and suggest that hydronium carbamates play an important role. They also state that carbamates are formed through a step of zwitterions, that can be stabilized through amines or water which is another favourable reaction in terms of amine efficiency. However, as the described reactions are the effects predominantly described in literature, they are considered as the basis for the model in this work.

The adsorption process is modeled in terms of reaction rates, which means that the process can be described using only thermodynamic and kinetic parameters of the reactions. This makes it possible to describe the process in a general way, intra-particle mass transfer can be considered separately and the model is adjustable to different materials.

The rates of the reactions of carbamate and bicarbonate formation, as well as of the physisorption of water are described through the following equations [45, 86, 27]. The physisorption of carbondioxide prior to chemical reactions is assumed to be of negligible impact as shown by Ge et al. [27]. The exponents on the water concentration in R_{ph} and R_{bi} were added to improve the model's predictions.

$$R_{cm} = \frac{\partial C_{cm}}{\partial t} = k_d \left(C_{am}^2 C_{\mathrm{CO_2}} - \frac{C_{cm} C_{pr}}{K_d} \right) \tag{3.58}$$

$$R_{ph} = \frac{\partial C_{H_2O_{ph}}}{\partial t} = k_{ph} \left(C_{\mathrm{H_2O}}^2 - \frac{C_{H_2O_{ph}}}{K_{ph}} \right) \tag{3.59}$$

$$R_{bi} = \frac{\partial C_{bi}}{\partial t} = k_{bi} \left(C_{am} C_{H_2O_{ph}}^n C_{\mathrm{CO_2}} - \frac{C_{bi} C_{pr}}{K_{bi}} \right) \tag{3.60}$$

with the kinetic factors

$$k_j = A_j \cdot \exp\left(\frac{-\Delta E_i}{RT} \right), \quad j = cm, ph, bi. \tag{3.61}$$

A_i and ΔE_i with $i = cm, ph, bi$ are the kinetic constants and activation energies of the carbamate reaction, physical adsorption, and bicarbonate reaction, respectively. K_i are the equilibrium constants defined in terms of the concentrations of the species. These approximate the thermodynamic definition of the equilibrium constants, which are defined as

$$K_j = \exp\left(\frac{-\Delta G_j}{RT} \right), \quad j = cm, ph, bi. \tag{3.62}$$

ΔG_j refers to the respective Gibbs free energy of the reaction, and is temperature dependent as

$$\Delta G_j = \Delta H_j - T \cdot \Delta S_j, \tag{3.63}$$

where ΔH_j and ΔS_j are the enthalpy and entropy change of the forward reaction, and are expected to be negative in the considered reactions as heat is released together with a reduction in entropy. The thermodynamic equilibrium constants can also be defined in terms of activities a_i of reactants and products. The activity can be expressed via the concentration and a reference concentration (c_i°) and the activity coefficient γ_i. If the quotient of the activity coefficients as well as of the reference concentrations is approximated to 1, the thermodynamic equilibrium constant can be estimated with the concentrations. With the example of the carbamate reaction:

$$K_{cm} = \frac{a_{cm} a_{pr}}{a_{am}^2 a_{\mathrm{CO_2}}} = \frac{\frac{C_{cm}}{C_{cm}^\circ} \gamma_{cm} \frac{C_{pr}}{C_{pr}^\circ} \gamma_{pr}}{\left(\frac{C_{am}}{C_{am}^\circ} \gamma_{am} \right)^2 \frac{C_{\mathrm{CO_2}}}{C_{\mathrm{CO_2}}^\circ} \gamma_{\mathrm{CO_2}}} \approx \frac{C_{cm} C_{pr}}{C_{am}^2 C_{\mathrm{CO_2}}} \tag{3.64}$$

The generation terms G_i due to chemical reaction can thus be calculated through the reaction rates and the stoichiometric constants for the respective species and reaction $\nu_{i,j}$

$$G_i = \sum_j R_j \cdot \nu_{i,j}. \tag{3.65}$$

3.1.9. Calibration of model parameters

The model described here requires the input of parameters for the chemical reaction, including both equilibrium parameters (enthalpy and entropy of reaction) and kinetic parameters (Arrhenius constants and activation energies). The following sections detail the methodology and results of the estimations for the model.

Thermodynamic parameters

To calculate the equilibrium state using the model as described above, values for the difference in enthalpy (ΔH) and entropy (ΔS) are required for each reaction. The parameters for the carbamate reaction and the pyhsical adsorption of water can be fitted to pure component adsorption measurements of CO_2 and H_2O, respectively. The values for the bicarbonate reaction can then be estimated from co-adsorption measurements.

The experimental data used for the fitting is reported by Young et al. [97], which covers the low pressure region in detail. An error function between the experimental values (q_{ex}) and the model of this study in equilibrium (q_m) is defined. The error function is minimized using the least-square method.

$$f = q_m - q_{ex} \tag{3.66}$$

To calculate the loading in dry conditions with the model of this study, the carbamate reaction is evaluated in equilibrium which gives the constraint of the reaction rate being equal to zero. From this and stochiometric constraints, the carbamate concentration is calculated, which determines the CO_2 loading on the material as

$$q_{\mathrm{CO_2},m} = \frac{C_{cm}}{\rho_p}, \tag{3.67}$$

where ρ_p is the density of one particle. From this, the parameters ΔH_{cm} and ΔS_{cm} can be fitted. For the wet reaction, the same procedure is conducted to fit ΔH_{ph} and ΔS_{ph}.

The fit for the carbamate parameters was done in the low pressure region, including only data points measured at a partial pressure of CO_2 below $1{\cdot}10^4\,\mathrm{Pa}$. The temperature in the experiments was varied between 289 and 381 K. The same temperature range was considered to fit the water adsorption equation, and the partial pressure of H_2O is calculated from the relative humdity RH of air at $P = 1\,\mathrm{atm} = 101325\,\mathrm{Pa}$, which was varied between $\mathrm{RH} = 0 - 60$ %.

The parameter fitting was done using the least squares method with a Levenberg-Marquardt algorithm. To evaluate the quality of the model and the fit, the relative standard deviation σ_{rel} was calculated for each fitted parameter. It is derived based on a linear approximation to the model function around the optimum and is defined as

$$\sigma_{rel} = \sqrt{\frac{S(\boldsymbol{\theta})}{n-p}}, \tag{3.68}$$

where $S(\boldsymbol{\theta})$ is the square of the error sum of the squares function dependent on the parameter vector $\boldsymbol{\theta}$, n is the number of data points and p is the number of parameters [93]. All fitted values together with their relative standard deviation are reported in Table 3.2.

Table 3.2: Fitting results of thermodynamic parameters

Case	Carbamate	H_2O
ΔH [kJ/mol]	-72.0	-82.65
rel. std. dev [%]	5.43	0.98
ΔS [J/mol K]	-225.63	-179.54
rel. std. dev [%]	5.49	1.40
Number of Datapoints	23	56

To estimate the parameters of the bicarbonate reaction, co-adsorption isotherms are considered. Under these conditions, with experimental isotherm data from Young et al., the least-square method did not provide satisfactory results, however, a qualitative solution was found. A difference in enthalpy of the

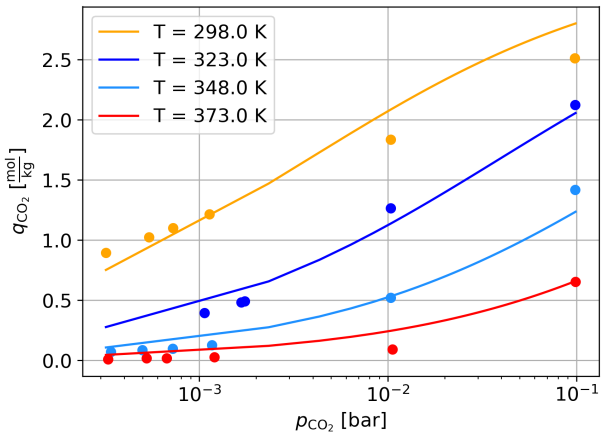

(a) Fitted isotherm model for pure CO_2. Comparison to data for low partial pressures of CO_2.

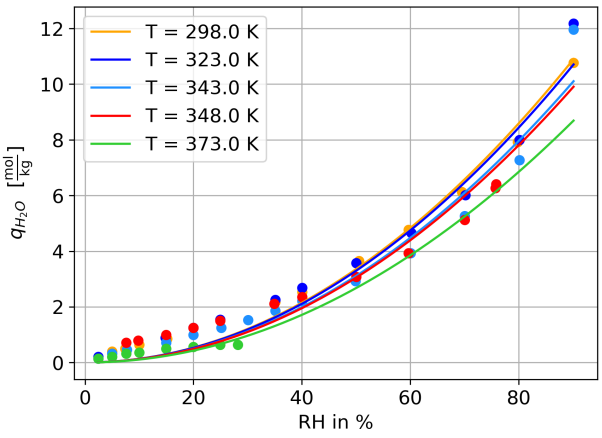

(b) Fitted isotherm model for pure H_2O. Comparison to data at different partial pressures of H_2O, corresponding to given RH in air at ambient pressure and respective temperature.

Figure 3.5: Comparison of the fitted pure-component isotherms of this model to the experimental isotherms from Young et al. [97]. Lines represent the model, experimental data represented by dots.

bicarbonate reaction of $\Delta H_{bi} = -50\,\mathrm{kJ/mol}$, a difference in entropy of $\Delta S_{bi} = 130\,\mathrm{J/mol\,K}$, and the exponent $n = 0.7$ were chosen. The model follows the shape of the isotherm, predicts an increase of adsorption in humid conditions, and a decrease with higher temperature. Besides a comparison to experimental data from Young et al. [97], data from Elfving et al. [20] on a polymeric, amine-functionalised sorbent is shown together with the model's predictions (Figure 3.6). To account for the different material, only the density of the sorbent material was adjusted. It can be seen that the model describes neither of the data quantitatively, but gives a good qualitative estimation of the isotherms.

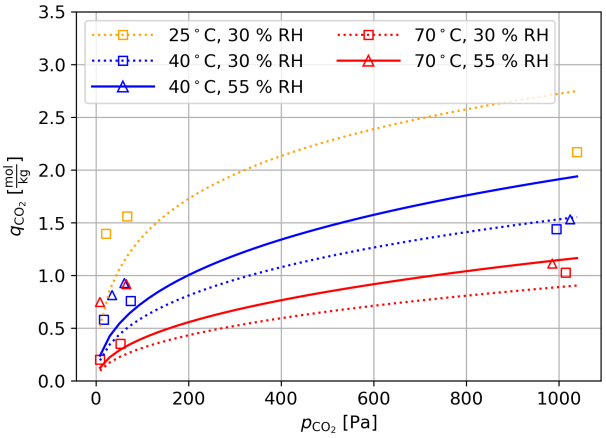

(a) Datasets from Young [97] with constant partial pressure of H_2O corresponding to given RH of air at ambient pressure and respective temperature.

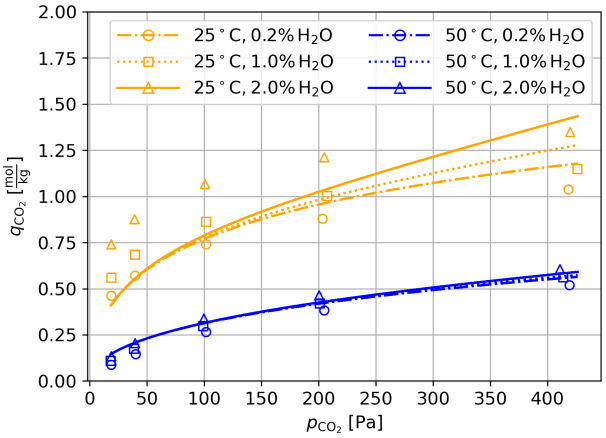

(b) Datasets from Elfving [20] with constant percentage of H_2O in the gas mixture.

Figure 3.6: Comparison of co-adsorption isotherms from the model estimations (lines) and experimental isotherm data (symbols) on a low partial pressure range of CO_2. Data for different temperatures and H_2O content.

Kinetic parameters

The kinetics of the reaction model are represented through the kinetic factors k_i (i = cm, ph, bi). These are temperature dependent, and characterized by the Arrhenius prefactor A_i and the activation energy of the forward reaction ΔE_i. To approximate the kinetic factor for the carbamate reaction, data of experiments in dry conditions is used. Bos et al. [9] measure the uptake of CO_2 at pure conditions with low partial pressures. They show that the diffusive effects are minimized at pure conditions for small particles ($D_p \approx 200\,\mu\mathrm{m}$), which makes the data suitable to fit the kinetic factors of the reaction equation. Data of experiments at a partial pressure $p_{CO_2} = 1 \cdot 10^4\,\mathrm{Pa}$ and temperatures between $T = 278 - 313\,\mathrm{K}$ was used to fit the parameters A_{cm} and ΔE_{cm}. The resulting values are $A_{cm} = 22.0489 \cdot 10^{-3}\,\mathrm{m^3/mol^3}$ with a standard deviation of $133.83\,\%$ and $\Delta E_{cm} = 24501\,\mathrm{J/mol\,K}$ with a standard deviation of $12.78\,\%$. While the standard deviation on the Arrhenius prefactor is high, the values yield a good approximation of the experimental data in the regarded conditions. The result of the model compared to the experimental data is shown in Figure 3.7a. Young et al. report data of a TGA experiment on the same material at $T = 75°\mathrm{C}$ in pure CO_2 a partial pressure of CO_2 of $p_{CO_2} = 20\,\mathrm{Pa}$. The model approximates the uptake of CO_2 with good accuracy under the assumption of a particle size equal to the effective size given by the manufacturer ($D_{p,eff}$). The prediction of the model vs. the experimental data can be seen in Figure 3.7b.

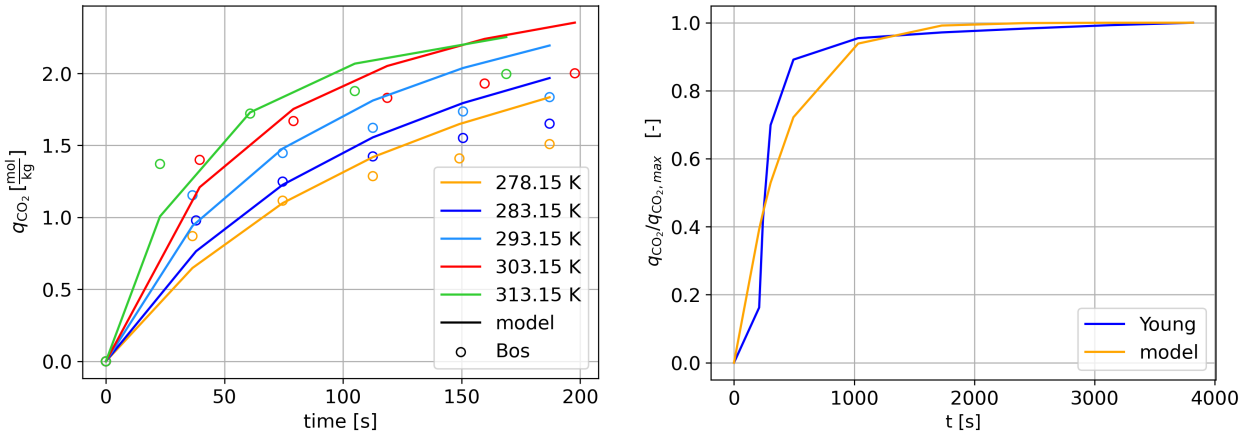

(a) Comparison to experiments from Bos et al. [9], conditions with pure CO_2 at a partial pressure of $p_{CO_2} = 1 \cdot 10^4\,\mathrm{Pa}$ and different T

(b) Comparison to experiments from Young et al. [97], conditions with pure CO_2 at $p_{CO_2} = 20\,\mathrm{Pa}$ and at $T = 75\,°\mathrm{C}$

Figure 3.7: Loading over time from the model and experimental data from Bos et al. [9] and Young et al.[97]

It is assumed that the physical adsorption of water is not rate limiting [45, 86], and an accordingly high value for the kinetic factor is applied. The effects of the kinetic parameters of the bicarbonate reaction can be evaluated with co-adsorption data. To avoid significant external mass transfer effects, dynamic data from TGA experiments under non-dilute conditions is most suitable. Young et al. [97] report data of an experiment on Lewatit under $T = 25°\mathrm{C}$ and a partial pressure of H_2O equivalent to $30\,\%\,\mathrm{RH}$ in air at ambient conditions. With the assumption of the particle diameter being equal to the equivalent diameter $D_{p,eq}$ and the pore size equal to the average pore size $d_{p,av}$, the kinematic factor of the bicarbonate reaction is estimated by comparing the model's prediction to the experimental results from Young's experiment at a partial pressure of $p_{CO_2} = 20\,\mathrm{Pa}$. Young et al.'s study is the only available data source of a suitable co-adsorption TGA experiment, with reported dynamic uptake. As the data is only given for a single temperature, it is only possible to fit the kinematic factor k_{bi}, without distinguishing between the Arrhenius factor A_{bi} and the activation energy ΔE_{bi}. Thus, their ratio is estimated from data in literature [86]. The absolute value of the kinematic factor given in literature are lower than what is found in this work, which is why those values are not directly applied. The results of the estimation are $A_{bi} = 3.5\,\mathrm{mol^3/m^3}$ and $E_{bi} = 60\,\mathrm{kJ/mol\,K}$.

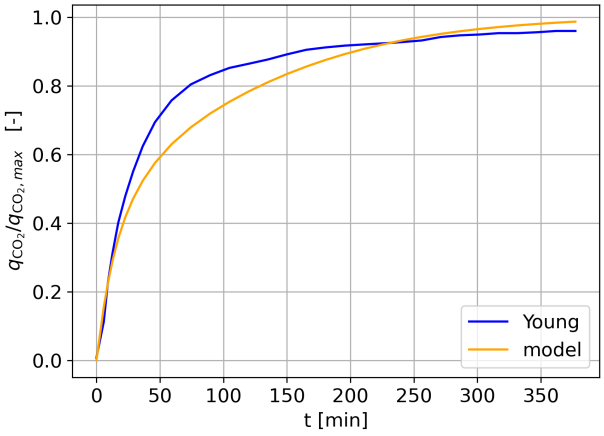

Figure 3.8: Comparison of the loading over time from experimental data by Young et al. [97] to the model's prediction. Conditions of p_{CO_2}, $\mathrm{RH} = 0.3$ and $T = 25\,^{\circ}\mathrm{C}$.

3.2. Contactor model

The schematics of the contactors are displayed in Figure 3.9. The packed bed consists of a cylinder with many spherical particles of the sorbent with a bed porosity ε_b. The monolith is assumed to have a square cross-section with square channels and unit cells of width b_2. The wall between two channels consists of the porous sorbent material of width dw, yielding a channel width of b_1. The porosity of the monolith ε_{mon} follows directly from the dimensions of the channels and the wall. The assumption is made that all channels behave the same, thus one channel is considered for the calculations. Both reactor models are set up as one-dimensional in axial direction and the ideal gas law is applied for all fluid phases.

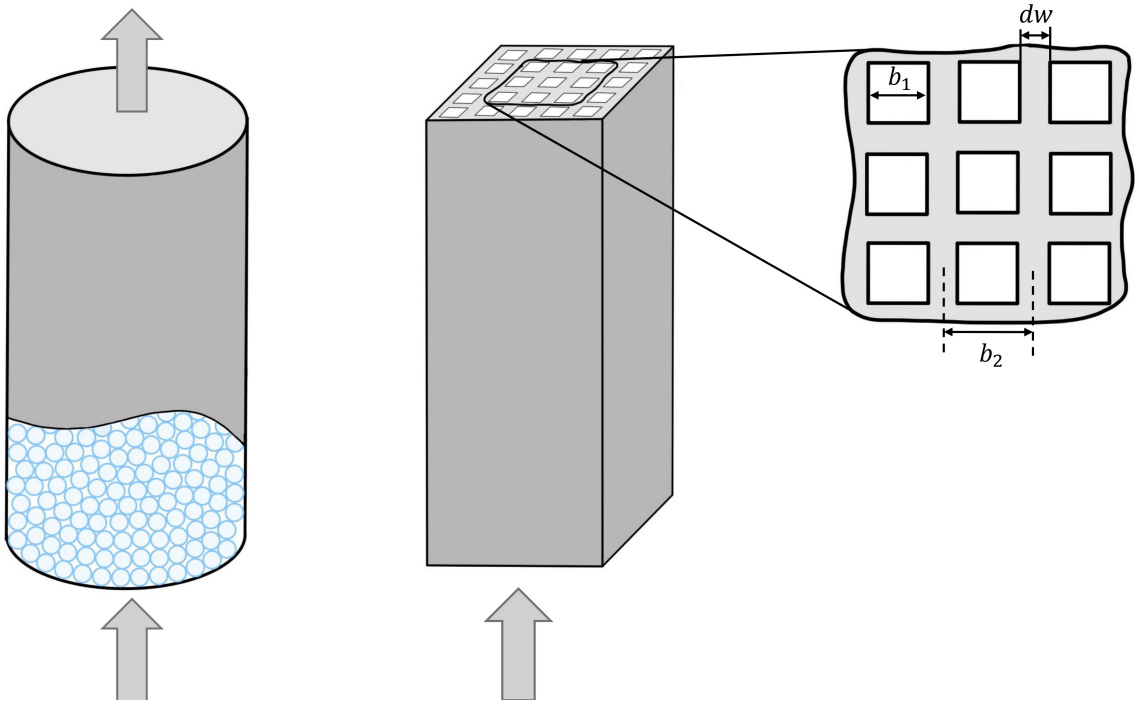

(a) Packed bed **(b)** Monolith

Figure 3.9: Schematics of the two considered contactors with dimensional parameters of the cross section of the monolith.

3.2.1. Species balance equation

The model is set up after the models from Elfving et al. [20] and Stampi-Bombelli et al. [85]. The balance equation over the interstitial control volume of the gas phase reads

$$\frac{\partial C_i}{\partial t} = D_L \frac{\partial^2 C_i}{\partial z^2} - \frac{v_s}{\varepsilon_j}\frac{\partial C_i}{\partial z} - \frac{1-\varepsilon_j}{\varepsilon_j}\rho_s \frac{\partial q_i}{\partial t} \tag{3.69}$$

for each species i and both reactors. The right most term is the change in loading of the material and is calculated in the particle-scale model, which will be explained in the following section. C_i is the concentration of species i, ε_j is the porosity of the bed or the monolith, ρ_s is the density of the sorbent (and thus of one particle or the material of the wall of the monolith) and D_L denotes the axial dispersion coefficient. v_s the superficial velocity of the gas phase. It is assumed to be constant in the adsorption cases, where air is pushed through the column with a blower. The changes in velocity over the column length due to molecules adsorbing is neglected, as it is done in similar models in literature [20, 84, 75]. In the case of desorption, pressure is reduced and the influence of the released molecules on the velocity in the column might not be negligible. Thus, an equation for the calculation of the local velocity is added [75]

$$\left(\frac{1}{\varepsilon_j}\frac{p}{RT}\right)\frac{\partial v_s}{\partial z} = \frac{(1-\varepsilon_j)}{\varepsilon_j}\rho_s \sum_{i=n}^{n}\frac{\partial q_i}{\partial t}, \tag{3.70}$$

which couples the change in loading on the sorbent with the velocity in the column, under the application of ideal gas law. The dispersion coefficient D_L differs for the two contactors and can be calculated as follows. For the packed bed, a correlation from Reazei [67] is used as

$$D_{L,pb} = \frac{v_s}{\varepsilon_b} D_p \left(\frac{0.45 + 0.55\varepsilon_b}{\mathrm{Re}\,\mathrm{Sc}} + 0.5\right), \tag{3.71}$$

with the interstitial velocity v_i. For the monolith the following is applied [64]

$$D_{L,mon} = D_m + \frac{\left(\frac{v_s}{\varepsilon_{mon}}\right)^2 b_1^2}{192 D_m}. \tag{3.72}$$

with R_P being the averaged radius of the adsorbent particles, Re the Reynolds number and Sc the Schmidt number according to

$$\mathrm{Re} = \frac{D_p v_s}{\nu} \quad \text{and} \quad \mathrm{Sc} = \frac{\nu}{D_m} \tag{3.73}$$

using the kinematic viscosity of the inlet gas mixture. D_m is the molecular diffusion coefficient, and b_1 the width of one channel in the monolith structure.

3.2.2. Solution

Just like for the particle model (see Section 3.1.5), the PDEs are solved by the application of the method of lines and the ODE solver `solve_ivp` from `SciPy`, under the application of the method `LSODA` [92]. A mesh independence study was conducted for an exemplary case, and its results presented in Appendix 8.

3.2.3. Discretization

The contactor is discretized with N control volumes in one dimension over its length L. In the center of each control volume, a calculation point k is located, with $k = 0$ in the first cell at the inlet and $k = N$ at the last cell before the outlet of the column. In the following, the discretization is shown for the concentration of a species i where the index i not written for the sake of simplicity. All convective terms are approximated through first order upwind differences [25]:

$$\left.\frac{\partial C}{\partial z}\right|_k \approx \frac{C_k - C_{k-1}}{\Delta z}. \tag{3.74}$$

For the diffusive terms, central differences are applied

$$\left.\frac{\partial^2 C}{\partial z^2}\right|_k \approx \frac{C_{k+1} - 2C_k + C_{k-1}}{\Delta z^2}. \tag{3.75}$$

3.2.4. Boundary and initial conditions

The boundary condition at the end of the column (z = L) is a zero-gradient boundary condition

$$\left.\frac{\partial C}{\partial z}\right|_{z=L} = 0. \tag{3.76}$$

At the lower boundary ($z = 0$), a Danckwert's boundary condition is applied

$$D_L \left.\frac{\partial C}{\partial z}\right|_{z=0} = -v_i \left(C^\infty - C|_{z=0}\right), \tag{3.77}$$

where C^∞ is the concentration in the feed gas.

The initial concentrations of CO_2 and H_2O in gas phase in the column and in the particle are chosen to be zero. The initial conditions for the adsorbed species in the material are dependent on the case and given in Table 3.3. Generally, for the adsorption cases no prior binding of CO_2 and H_2O is assumed, and the equilibrium state after adsorption is applied as the initial conditions for desorption cases.

3.2.5. Performance indicators

To compare the performance of the reactors, two performance indicators are calculated. The energy consumption of the blower providing the mass flow of air W_{fan} is calculated as

$$W_{fan} = \frac{1}{\eta_{fan}} \int_0^{t_{ads}} \dot{V} \Delta P \, dt, \tag{3.78}$$

and gives an indication of the difference in electrical energy required for the adsorption step. η_{fan} is the efficiency of the blower and assumed to be $\eta_{fan} = 0.5$, t_{ads} is the time considered until evaluation, $\dot{V}$ is the volumetric flow rate of air and ΔP is the pressure drop over the considered contactor. To calculate ΔP, the Ergun equation [24] is applied for the packed bed

$$\frac{\Delta P}{L} = 150 \frac{(1-\varepsilon_b)^2}{\varepsilon_b^3} \frac{\mu}{D_p^2} v_s + 1.75 \frac{1-\varepsilon_b}{\varepsilon_b^3} \frac{\rho}{D_p} v_s^2 \tag{3.79}$$

where ρ and μ are the density and viscosity of the air passing through the contactor. For the monolith, the Hagen-Poiseuille equation is applied [15]

$$\frac{\Delta P}{L} = \frac{32\mu}{D_c^2 \varepsilon_{mon}} v_s \tag{3.80}$$

where D_c is the hydraulic diameter of one channel in the monolith, which is equal to the channel width b_1. The productivity is calculated as

$$P_{ads} = \frac{q_{ads}}{t_{ads}}, \tag{3.81}$$

where q_{ads} is the loading CO_2 on the sorbent.

3.3. Considered cases and dimensions

Table 3.3 summarizes the conditions for the simulated cases, which include four adsorption scenarios and one desorption scenario. In all adsorption cases (Dry, Low RH, Medium RH and High RH), the pressure is maintained at $101325\,\mathrm{Pa}$, the temperature at 25°C, and the partial pressure of CO_2 at $40.54\,\mathrm{Pa}$. The relative humidity varies among these cases: 0% for the dry case, 30% for the low RH case, 55% for the medium RH case and 90% for the high RH case, resulting in corresponding partial pressures of water vapor. The Low RH case is considered the base case in this study, and is evaluated when different parameters are varied. The initial concentrations for the adsorption cases reflect the amine loading of the material, with the assumption that no water or CO_2 is adsorbed initially.

For the desorption case, the pressure is significantly reduced to $5\,\mathrm{Pa}$, and the temperature is increased to 55°C. The partial pressure of CO_2 is lowered to $0.5\,\mathrm{Pa}$. Unlike the adsorption cases, the desorption scenario does not involve relative humidity but considers a specific partial pressure of water vapor. The initial concentrations of adsorbed species for the desorption case are based on the equilibrium outcomes of the Low RH adsorption case, with specific values for amines, carbamates, bicarbonates, and adsorbed water. Thermophysical properties of air like the density ρ, and the viscosity μ are obtained from the python module `coolProp` [4].

Table 3.3: Conditions of the considered adsorption and desorption cases

Parameter	Ads. dry	Ads. low RH	Ads. medium RH	Ads. high RH	Desorption
$P\,[\mathrm{Pa}]$	101325	101325	101325	101325	5
$T\,[^\circ\mathrm{C}]$	25	25	25	25	55
$p_{\mathrm{CO_2}}\,[\mathrm{Pa}]$	40.54	40.54	40.54	40.54	0.5
RH [%]	0	30	55	90	N/A
$p_{\mathrm{H_2O}}\,[\mathrm{Pa}]$	0	946.50	1735.23	2839.46	4.5
$\rho\,[\frac{\mathrm{kg}}{\mathrm{m^3}}]$	1.185	1.181	1.177	1.172	not considered
$\mu\,[\mathrm{Pa\cdot s}]$	$1.844\cdot10^{-5}$	$1.839\cdot10^{-5}$	$1.834\cdot10^{-5}$	$1.828\cdot10^{-5}$	not considered
$C_{am,0}\,[\frac{\mathrm{mol}}{\mathrm{m^3}}]$	5896	5896	5896	5896	4440.58
$C_{cm,0}\,[\frac{\mathrm{mol}}{\mathrm{m^3}}]$	0	0	0	0	603.97
$C_{bi,0}\,[\frac{\mathrm{mol}}{\mathrm{m^3}}]$	0	0	0	0	247.48
$C_{pr,0}\,[\frac{\mathrm{mol}}{\mathrm{m^3}}]$	0	0	0	0	851.45
$C_{\mathrm{H_2O,ads},0}\,[\frac{\mathrm{mol}}{\mathrm{m^3}}]$	0	0	0	0	1062.60

To evaluate the influence of intra-sorbent mass transfer on the overall adsorption and desorption process, a parameter study is conducted with varying sorbent characteristics. In the evaluation on a particle scale, the particle size, pore size and tortuosity are varied from the values given for Lewatit. The considered particle sizes are $D_p = 150\,\mu\mathrm{m}$, $200\,\mu\mathrm{m}$, $520\,\mu\mathrm{m}$ and $1000\,\mu\mathrm{m}$. Values for the average pore size are considered to be $15\,\mathrm{nm}$, $20\,\mathrm{nm}$, $57\,\mathrm{nm}$, $100\,\mathrm{nm}$ and $150\,\mathrm{nm}$. The tortuosity of the material is varied from its original value 2.3 to 1, 3 and 6.

To evaluate the differences between the packed bed and the monolith, different dimensions of the reactors are considered. Estimations of a feasible channel size and wall-thickness for the monolith are taken from Stampi-Bombelli et al.'s work [84], in which a commercially available monolith is studied. The size of one cell in the cross-section of the monolith is taken to be $b_2 = 3,\mathrm{mm}$, with $N_{ch} = 144$ channels arranged in a square pattern. To maintain the same diffusion length within the sorbent, the wall thickness dw is chosen to be equal to the particle size D_p in the packed bed, and the width of a channel b_1 follows from that. The cross-sectional area of both contactors is kept the same for all configurations, leading to identical superficial velocities for a given flow rate. Additionally, the total mass of sorbent $M_{sorbent} = 0.1\,\mathrm{kg}$ is consistent between the two reactors, ensuring the same maximum quantity of adsorbed carbon dioxide. From the given cross-sectional area, the radius of the packed bed is calculated. The porosity ε_b is estimated from literature [97], the porosity of the monolith ε_{mon} follows from the chosen dimensions of the width of the channel and the walls as

$$\varepsilon_{mon} = \left(\frac{b_1}{b_2}\right)^2 \tag{3.82}$$

The length of each reactor is calculated from the given sorbent mass, the cross-sectional area and the porosity. Two configurations are considered in this study, one with a particle size and wall thickness of the effective particle size of Lewatit ($D_p = dw = 520\,\mu\mathrm{m}$; standard dimensions), and one with an increased intra-sorbent diffusion length ($D_p = dw = 1000\,\mu\mathrm{m}$; variation). In order to associate the different mass transfer mechanisms to their influence on the results, a variation to a very small intra-sorbent diffusion length ($D_p = dw = 100\,\mu\mathrm{m}$; control) is considered. This configuration is not realistically feasible, for example in terms of stability of the monolith, but serves the purpose of comparison. Tables 3.4 and 3.5 summarize the dimensions of the contactors. In addition to the variation of the contactor dimensions, the volumetric flow rate of air is varied from a chosen standard rate of $\dot{V} = 51.84\,\mathrm{L/s}$ to a reduced rate of

$\dot{V} = 6.48\,\mathrm{L/s}$. Lastly, a case where the fan power required to blow the air through the contactors is held constant to $\dot{W}_{fan} = 6.86\,\mathrm{W}$ is evaluated.

Table 3.4: Considered dimensions for the packed bed

Parameter		fixed	
$M_{sorbent}$ [kg]		0.1	
R_{col} [mm]		20.31	
	std. dim.	variation	control
D_p [μm]	100	520	1000
ε_b [-]	0.4	0.4	0.4
L_b [mm]	146.13	146.13	146.13

Table 3.5: Considered dimensions for the monolith

Parameter		fixed	
$M_{sorbent}$ [kg]		0.1	
b_2 [mm]		3.0	
N_{ch} [$-$]		144	
$N_{ch,row}$ [$-$]		12	
	std. dim.	variation	control
dw [μm]	100	520	1000
ε_{mon} [-]	0.683	0.444	0.934
L_{mon} [mm]	276.9	157.8	1337.5

4

Results

4.1. Particle-scale model

In the first part of this section, the effects of film diffusion on the adsorption process is evaluated. Following this, the low RH adsorption case and the desorption case are analyzed, with a detailed evaluation of the differences between the Fickian and Maxwell-Stefan models. Next, the influence of humidity is assessed by comparing the adsorption cases at different humidity levels. Following, the results of the parameter sensitivity analysis of the particle size, pore size, and tortuosity representing the pores structure are reported.

4.1.1. Film diffusion

The effects of diffusion through the boundary layer around the particle are added through a boundary condition as described in Section 3.1.7. The influence of the external mass transfer is evaluated with the Fickian model. The implementation of film diffusion in the Maxwell-Stefan model is not straightforward, and bears source of inaccuracies. This is because the flux-diffusion matrix is set up in terms of the effective diffusion coefficients that apply within the porous material. Additionally, the mass fractions can only be calculated by considering the concentrations of the adsorbed species at the surface of the particle, which can lead to inaccuracies when the concentrations at the boundary are dynamic over time and the gradients are steep. The relevance of film diffusion is the same for both models, which is why the conclusions from the analysis with the Fickian model can be applied to the Maxwell-Stefan model.

The predictions of the model are calculated by including the influence of external mass transfer and compared to the outcomes of the model disregarding this effect. The results are evaluated for the adsorption case under low RH and the material parameters for Lewatit. The CO_2 concentration profiles over the particle radius is the displayed in Figure 4.1a for the case of an external velocity $v = 0\,\mathrm{m/s}$ and under neglecting external mass transfer. The loading over time on the particle is shown for in Figure 4.1. The largest effects of film diffusion are expected when the external mass transfer coefficient is small, which occurs at low bulk velocities. This is exemplified in the limiting case of stationary gas at $v = 0\,\mathrm{m/s}$. The concentration profiles indicate that due to film diffusion, the concentrations at the surface of the particle ($r = R$) increase over time. However, even in the limiting case of $v = 0\mathrm{m/s}$, the effect is minimal. The differences are low both at the surface and in the center of the particle, which is why the particle size is not expected to change the observation. Therefore, external mass transfer has a negligible influence on the change in loading on the material, as illustrated in Figure 4.1b. Due to these findings, external mass transfer is excluded from the model for the following analysis, and the constant value boundary condition is applied.

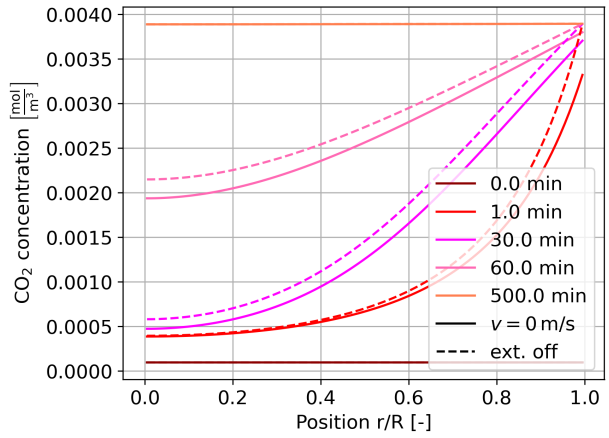

(a) Comparison on the gaseous CO_2 concentration profiles over the particle

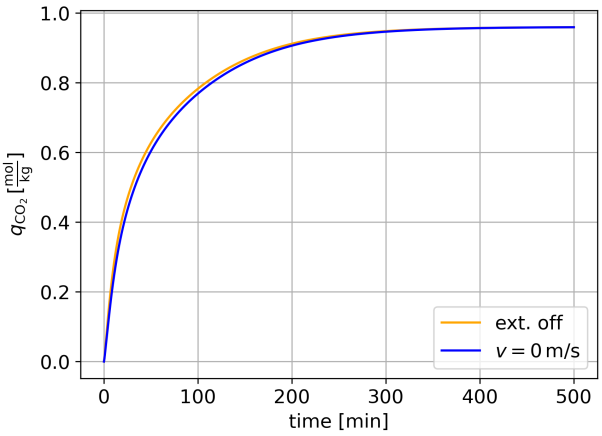

(b) Comparison on the CO_2 loading over time

Figure 4.1: Results with external mass transfer boundary condition under zero bulk velocity v compared to the outcomes disregarding external mass transfer.

4.1.2. Example case and comparison of diffusion models

Comparison loading over time

The adsorption case with low RH ($30\,\%$) as well as the desorption case are evaluated until equilibrium is reached, which is verified as at the end of the simulated time, the total loading changes less than $0.05\,\%$ within $30\,\mathrm{min}$. The resulting loading over time is shown in Figure 4.2. The adsorption time is $t_{ads} = 253.3\,\mathrm{min}$, which is defined as the time after which the loading has reached $98\,\%$ of the equilibrium value. The desorption time $t_{des} = 112.5\,\mathrm{min}$ is defined as the time after which $98\,\%$ of the total desorbed quantity have been desorbed. The results show a steeper decrease of the loading in the beginning compared to the increase during adsorption. This is due to the elevated temperature and the decreased pressure, which elevate the reaction rates and decrease the diffusion resistances. The two models (Maxwell-Stefan and Fick) predict only slightly different uptakes in the adsorption case, and the curves coincide fully for desorption. The Knudsen number (Section 3.1) refers to the intra-particle diffusion regime and indicates whether Knudsen diffusion or molecular diffusion is governing. According to literature, Knudsen diffusion dominates at values of $\mathrm{Kn} > 10$, while continuum diffusion dominates at $\mathrm{Kn} < 0.1$. Between 0.1 and 10, the regime is in transition and both effects influence the diffusion [37]. For CO_2, it is $\mathrm{Kn} = 1.527$ for the adsorption case, and $\mathrm{Kn} = 3.4 \cdot 10^4$ for the desorption case. Due to the low pressure and elevated temperature at desorption, the Knudsen number is high and the diffusion is expected to be governed by Knudsen diffusion. The adsorption process takes place in the transition regime, making both mechanisms relevant. The fact that the models do not differ in their descriptions of Knudsen diffusion, explains that they coincide for the desorption case.

The Maxwell-Stefan model is computationally more expensive. For the considered adsorption case and a simulated time of $8\,\mathrm{h}$, the simulation time is ~ 30 times longer than for the Fickian model.

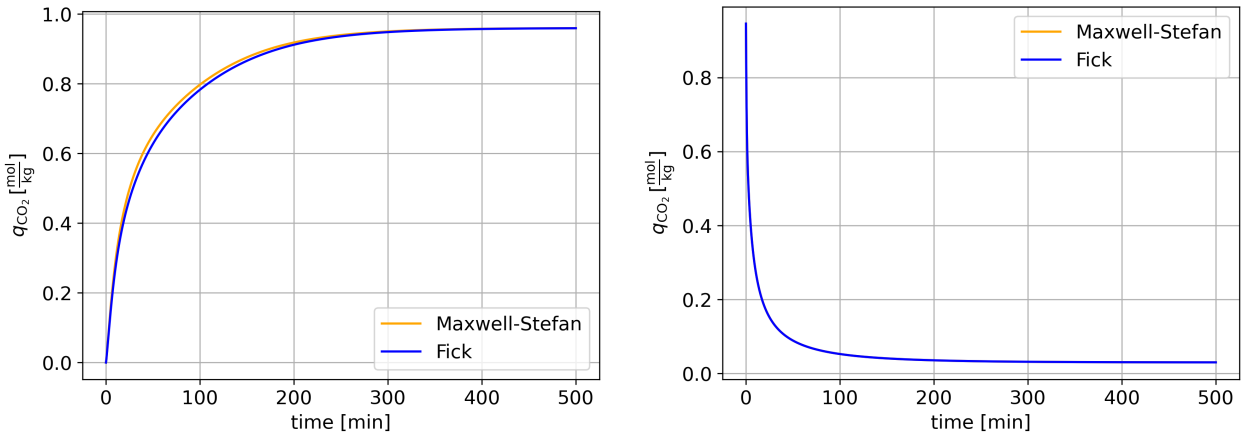

(a) Loading over time for adsorption under $30\,\%$ RH

(b) Loading over time for desorption

Figure 4.2: CO_2 loading on the material over time during the adsorption process under 30% RH and the desorption process

Concentration profiles adsorption case

Figure 4.3 shows the the concentration profiles of the gaseous CO_2 and H_2O vapour over the particle. It can be seen that the profiles show significant differences between the surface ($r = R$) and the center of the particle ($r = 0$). This demonstrates the diffusion effects and indicates that intra-particle diffusion is relevant for the adsorption rate. Differences between the Fickian and Maxwell-Stefan model are present in the concentration profiles at the center of the particle $r = 0$, where diffusion effects are relevant. Close to the surface of the particle (at $r = R$), the concentrations of adsorbed species is the same for both models, which verifies that the models only differ in the diffusive effects. The Maxwell-Stefan model predicts the diffusion to be faster than the Fickian model, at most time steps. The profiles of the H_2O concentration however show a change in that behaviour at later time steps (evident in the Figure at $t = 30.0\,\mathrm{min}$). This shows that the different species influence each other during diffusion in the Maxwell-Stefan equations. The overall faster diffusion leads to quicker adsorption and thus an earlier rise in the concentration of adsorbed species as can be seen in Figure 4.4. This Figure illustrates the concentration profiles of carbamates, bicarbonates and their sum, the total adsorbed CO_2 concentration, for the adsorption case at the center of the particle. The bicarbonate concentration exceeds the equilibrium value, and then declines after reaching an initial peak. This is due to the fact that the bicarbonate reaction in the model is faster than the carbamate reaction. Generally, a delay in rise in concentration can be seen, which is due to diffusion effects. This shows that the diffusion through the particle is limiting the adsorption process to some extent. Comparing the whole domain of the particle, diffusive effects are most important here as the gases need to travel the longest distance to the center of the particle. The evaluation of the adsorbed species at the surface of the particle ($r = R$) shows instant and fast adsorption. Here, $98\,\%$ of the equilibrium value of adsorbed CO_2 is reached ~ 90 minutes earlier than at the center of the particle (at $r = R$ after $213\,\mathrm{min}$, at $r = 0$ after $302.5\,\mathrm{min}$), which is $35.5\,\%$ of the total adsorption time.

While the two models show differences over the radius of the particle, the differences between the two models in the prediction of the loading is minor (see Figure 4.2). This is due to the fact that diffusive effects in the regions close to the surface of the particle do not or only slightly differ. These regions contribute more to the total loading, due to the spherical shape of the particle.

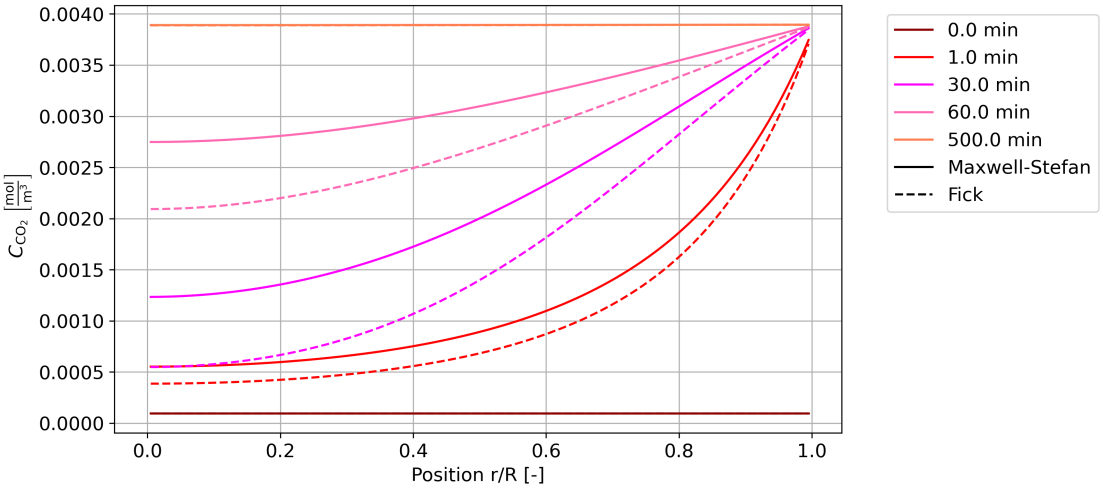

(a) Gaseous CO_2 concentration over the particle predicted by the Maxwell-Stefan and the Fickian model

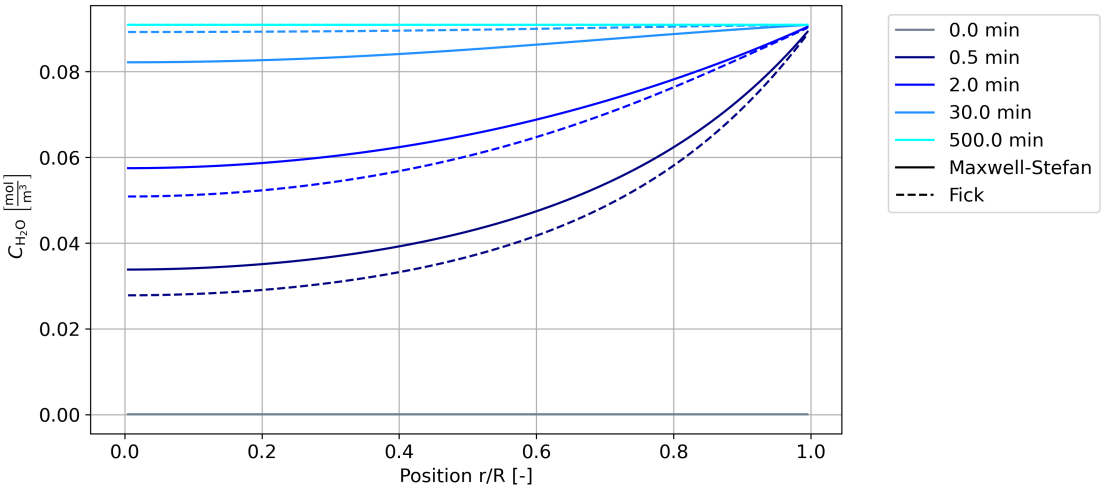

(b) H_2O vapour concentration over the particle predicted by the Maxwell-Stefan and the Fickian model

Figure 4.3: Concentration profiles of gaseous CO_2 and H_2O vapour over the particle during the adsorption process

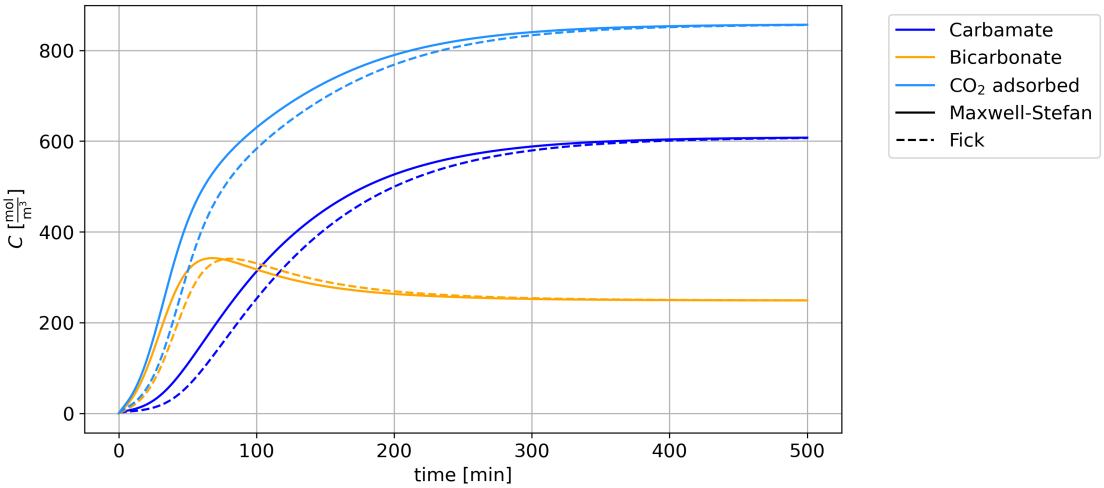

Figure 4.4: Concentrations of Carbamates, Bicarbonates and total adsorbed CO_2 at the center of the particle over time, predicted by the Maxwell-Stefan and Fickian model

Concentration profiles desorption case

Results for CO_2 profiles over the particle during the desorption case are displayed in Figure 4.5. The carbon dioxide level rises first and decreases as CO_2 is transported outside the particle. The concentration of gaseous CO_2 equalizes with the boundary condition significantly earlier than during adsorption. This is due to higher reaction rates elevated temperatures and lower diffusion limitations at reduced pressure. As the difference of the two diffusion models lies in the continuum diffusion effects, they predict the same results for the desorption case, which is governed by Knudsen diffusion. Only a slight difference in CO_2 concentration profiles at $t = 1\,\mathrm{min}$ is visible (Figure 4.5), which is attributed to numerical inaccuracies or slight influences of molecular diffusion that are not of relevance in the overall results.

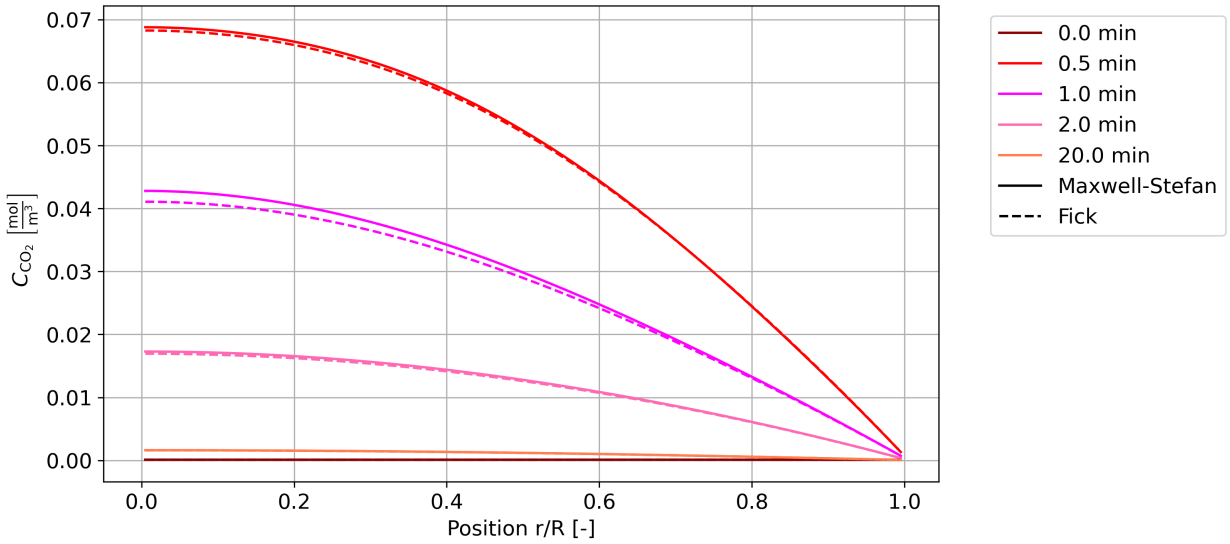

Figure 4.5: CO_2 concentration over the particle during desorption, predicted by the Maxwell-Stefan and the Fickian model

4.1.3. Humidity

To evaluate the influence of water on the adsorption process, the results of four adsorption cases are compared. Figure 4.6 displays the loading of the particle over time in the different cases. As illustrated in Figure 4.6a, the amount of CO_2 captured by the particle increases with the humidity level in the air. This behavior is expected due to the difference in stoichiometry between the carbamate and bicarbonate reactions. Figure 4.6b shows the loading normalized to the equilibrium loading for each case, allowing for a comparison of the uptake dynamics. The humid cases exhibit faster uptake in the early stages than the dry case, followed by a decrease in the uptake rate. This can be attributed to the faster kinetics of the bicarbonate reaction, followed by a transition to the carbamate reaction dominating. In all cases, equilibrium loading is reached after approximately 300 minutes, as the final stages of uptake are governed by the carbamate reaction kinetics. The high humidity case shows a similar, and at times slower uptake rate compared to the case with medium humidity. Furthermore, Fick's law overpredicts the uptake rate slightly in this case, while it shows a constant unprediction of the diffusion rate in the other cases. Still, both models yield very similar results, making both models valid to represent the adsorption process.

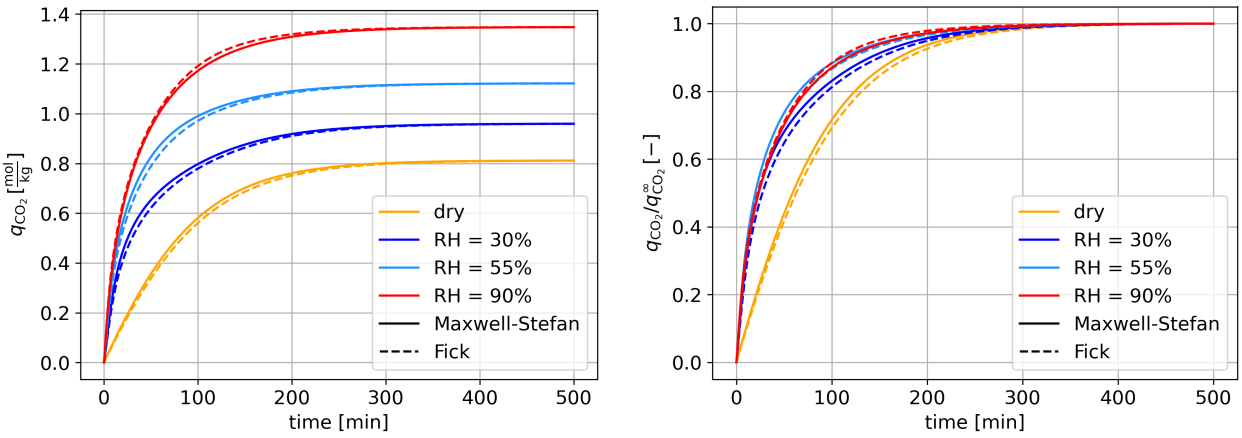

(a) Absolute loading

(b) Loading normalized with equilibrium loading

Figure 4.6: CO_2 loading on the material over time for different humidity levels on an absolute and normalized scale

To explore the reason for the difference in rate prediction under high humidity, the concentrations of the adsorbed species at the center of the particle is displayed in Figure 4.7. It can be seen that in this case, more bicarbonates are formed than carbamates, while carbamates dominate for the lower humidity levels considered. This gives the diffusion of water in the particle a higher relevance. While the Fickian model predicts the bicarbonate level to exceed its equilibrium value (like in the case with low RH), the Maxwell-Stefan model does not predict such behaviour at the center of the particle. Figure 4.8 shows that the Maxwell-Stefan model arrives at higher diffusion limitations of water at $t = 100\,\mathrm{min}$, which is when the predictions on the bicarbonate levels of the two models intersect. In conclusion, the Fickian model still underpredicts the overall diffusion rate, however shows an overprediction of the diffusion of water at later time steps. This is due to the Maxwell-Stefan model taking multicomponent effects into account, and thus giving a more accurate representation of the interaction of reaction diffusion effects.

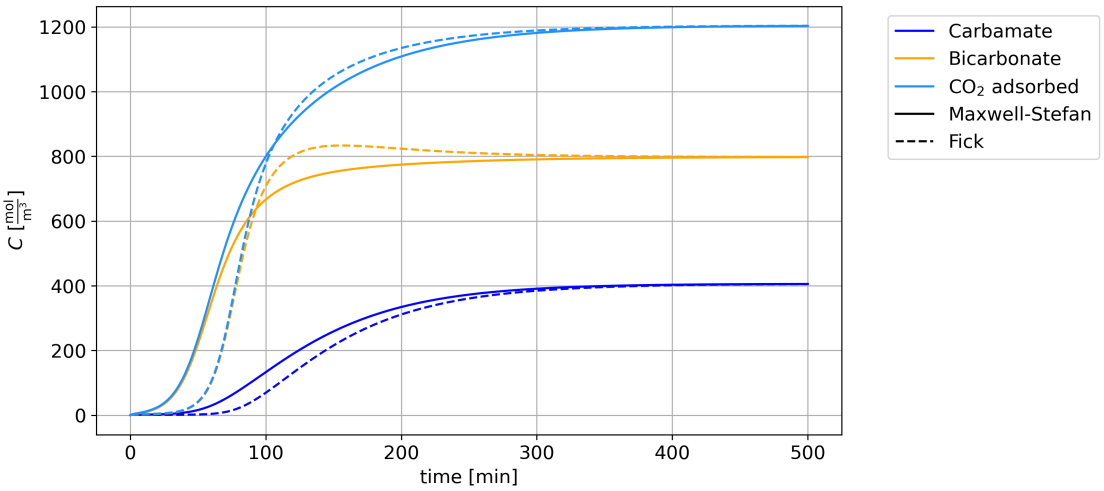

Figure 4.7: Concentrations of Carbamates, Bicarbonates and total adsorbed CO_2 at the center of the particle over time, for the adsorption case under 90% RH. Results predicted by the Maxwell-Stefan and Fickian model.

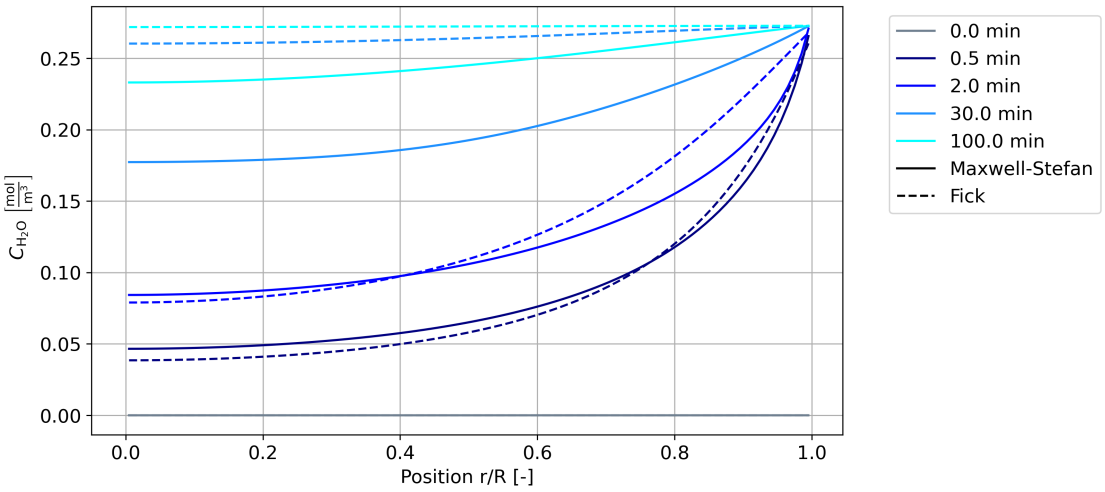

Figure 4.8: Gaseous CO_2 concentration over the particle, for the adsorption case under 90% RH. Results predicted by the Maxwell-Stefan and the Fickian model.

4.1.4. Particle size

The dynamic uptake of CO_2 is compared for different particle sizes for the adsorption case under low humidity and the desorption case. The results of the variations are illustrated in Figure 4.9, in form of the loading on the particle over time. The time until the equilibrium loading is reached increases with the particle diameter which reveals the influence of the intra-particle mass transfer on the adsorption process. The curves for particle diameters of $D_p = 150\,\mu\text{m}$ and $D_p = 200\,\mu\text{m}$ coincide, which shows that the diffusion limitations become insignificant from $D_p \lesssim 200\,\mu\text{m}$. The curves show a change in gradient after around 20 minutes, which corresponds directly to the transition from the bicarbonate to the carbamate reaction dominating. These findings are in agreement with the conclusion Bos et al. [9] draw from their experiments, and validates the magnitude of the diffusive part of the model. The same evaluation was done under the conditions of Bos et al.'s experiments, which revealed the same correlation and is shown in Figure 8.3. With the increase in relevance of diffusion on the adsorption process, the differences between the Maxwell-Stefan model and the Fickian model increase as well. The desorption case (Fig. 4.9b) shows an increase in time until equilibrium as well and thus confirms the trend. The Fickian and Maxwell-Stefan model predict the same results as only Knudsen diffusion is relevant.

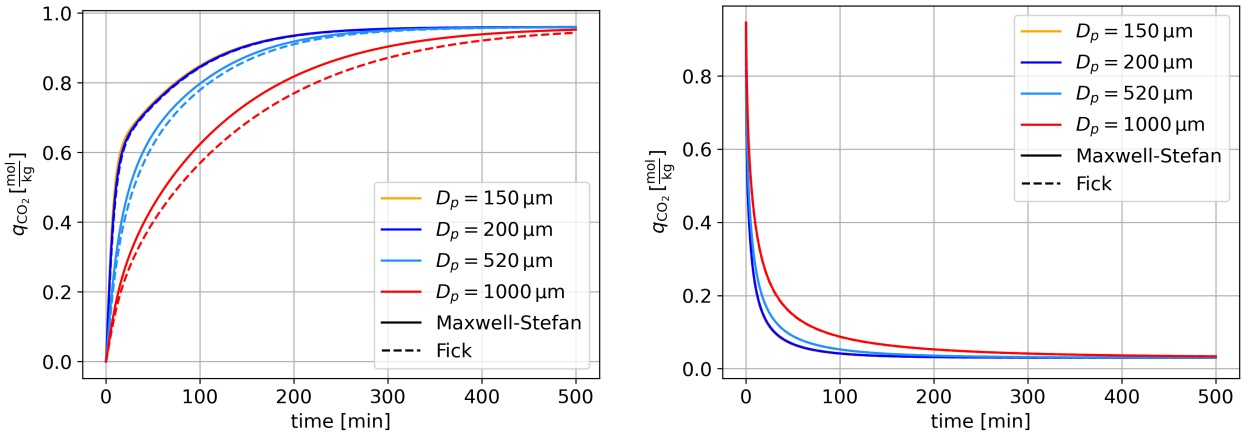

(a) For adsorption under RH = $30\,\%$

(b) For desorption

Figure 4.9: CO_2 loading over time for different particle sizes during adsorption under 30% RH and desorption. Results calculated by the Maxwell-Stefan and Fickian model.

4.1.5. Pore size

With an increase in pore size, the pore resistance decreases and diffusion to the center of the particle faster. On a particle of a diameter of $D_{p,eff}$, the results of different pore sizes are evaluated on the example of the adsorption case. As expected, the rate of change in loading rises with the pore size. From around a pore size of $d_p = 100\,\mathrm{nm}$, the behaviour does not change with further increase. This shows that from this size, the process becomes reaction limited. Furthermore it can be seen that at a pore size of $d_p = 15\,\mathrm{nm}$, the Maxwell-Stefan model and the Fickian model do not differ anymore, which indicates that the diffusion is now mainly governed by Knudsen diffusion. The Knudsen number for CO_2 for this pore size is $\mathrm{Kn} = 5.8$ which supports the conclusion.

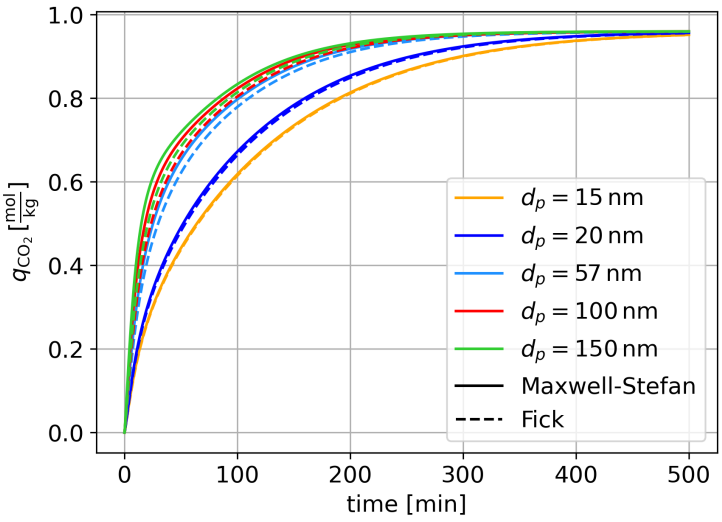

Figure 4.10: CO_2 loading over time during adsorption under 30% RH for different pore sizes. Results calculated by the Maxwell-Stefan and Fickian model.

4.1.6. Pore structure

In this model, the pore structure is represented by the tortuosity, a parameter that is notoriously difficult to measure accurately. The tortuosity can be significantly influenced by the arrangement of amines on the material, making it a variable of considerable interest. Given these complexities, examining different tortuosity values provides insights into how variations in the effective pore structure affect the adsorption process. In literature, typical values for the tortuosity lie between 2 and 6, with an average of 3 [13]. Thus, the values considered here are the tortuosity of Lewatit measured by Veneman [91] ($\tau_p = 2.3$), the average tortuosity $\tau_p = 3$ and an elevated value $\tau_p = 6$. For comparison, a tortuosity of $\tau_p = 1$ is considered, which corresponds to straight pores. The results in terms of the CO_2 loading on the particle are displayed in Figure 4.11. It can be seen that for a tortuosity equal to unity, the influence of diffusion becomes very small, as the loading curve adapts the shape resulting from the chemical reaction kinetics, and the Maxwell-Stefan and the Fickian model coincide. The tortuosity of the material ($\tau_p = 2.3$) shows a change, indicating the influence of diffusion. An elevation of the tortuosity factor only becomes relevant for a significant rise, as a value of $\tau_p = 3$ gives similar results, while the behavior changes significantly for $\tau_p = 6$.

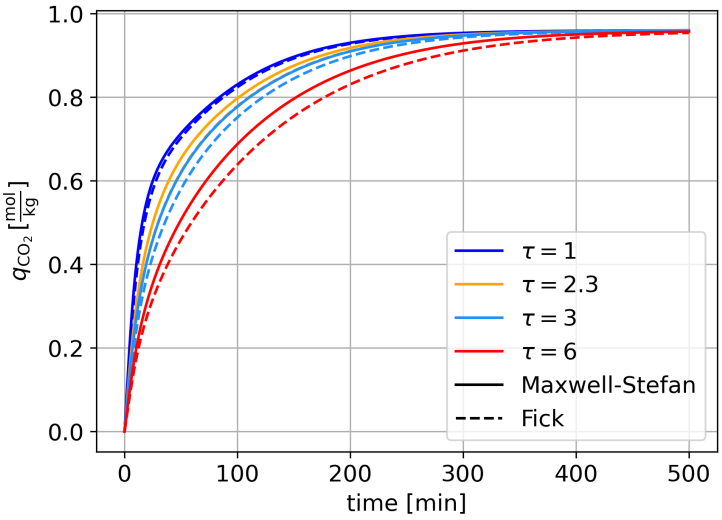

Figure 4.11: CO_2 loading over time during adsorption under 30% RH for different pore sizes. Results calculated by the Maxwell-Stefan and Fickian model.

4.2. Contactor model

In the first part of this section, the results of the packed bed model are compared to experimental data from breakthrough experiments. After that, the exemplary case with low relative humidity is analysed and the outcomes for both reactors are compared. That is followed by an evaluation of the effect of different humidity levels, a variation of the intra-sorbent diffusion length, *i.e.*, the particle size in the packed bed and the wall thickness in the monolith and a variation of the inflow rate. The parameter analysis is followed by an evaluation of the effect of the Maxwell-Stefan model vs. the Fickian on the contactor scale. The conducted simulations are then analysed by the evaluation of the previously defined performance indicators. Lastly, a desorption case is examined.

4.2.1. Comparison to breakthrough experiments

In this section, the predictions of the packed bed model are compared to experimental data from Shi et al. [81]. They conduct breakthrough experiments with a column filled with $\sim 600\,\mathrm{mg}$ Lewatit particles of a diameter of $D_p = 500 - 550\,\mu\mathrm{m}$, which is approximated in the simulation to the effective particle size $D_p = 520\,\mu\mathrm{m}$. The bed porosity is reported to be $\varepsilon_b = 0.464$ and with the inner diameter of the column, the bed length is estimated. Although the same material is used, the properties reported by Shi et al. differ from those found in other literature [91, 97] and considered in the development of this model. Shi et al. estimate the material density to be $\rho_s = 744\,\mathrm{kg/m^3}$ and a particle porosity of $\varepsilon_s = 0.338$ ($\rho_s = 880\,\mathrm{kg/m^3}$ and $\varepsilon_s = 0.238$ is considered in this study). The breakthrough experiment is conducted with a dry CO_2/N_2 mixture at ambient pressure and $T = 298\,\mathrm{K}$, with a CO_2 content of $400\,\mathrm{ppm}$, which corresponds to the dry adsorption case considered in this study. The superficial velocity is $v_s = 0.3\,\mathrm{m/s}$. The resulting breakthrough curve predicted by the model is displayed in Figure 4.12.

The shape of the curve is typical for a breakthrough experiment. t_5 and t_{95} mark the times of 5% and 95% breakthrough, respectively. The model predicts to reach 5% of the breakthrough (meaning the outlet concentration being equal to 5% of the inlet concentration) after $t_5 = 246\,\mathrm{min}$ and 95% of the breakthrough to be reached after $t_{95} = 549\,\mathrm{min}$. These times differ significantly form Shi et al.'s conclusions. They measure $t_5 = 93\,\mathrm{min}$ and $t_{95} = 278\,\mathrm{min}$. Thus, the modeled breakthrough curve is offset by $\Delta t_5 = +153$ minutes and the breakthrough of 95% is reached $\Delta t_{95} = +271$ minutes later than in the experiment. The lagging period, which is until t_5 is reached, takes up 44.8% of t_{95} in the simulation, while 33.45% in the experiment. Consequently, the breakthrough period between t_5 and t_{95} takes up 55.2% and 66.55% in the simulation and the experiment, respectively. Hence, the curves show slight differences in their slope. Conclusions on the total uptake of CO_2 can be drawn from the area above the breakthrough curve and below the equilibrium value. This differs significantly for the two curves, suggesting that the capacity of

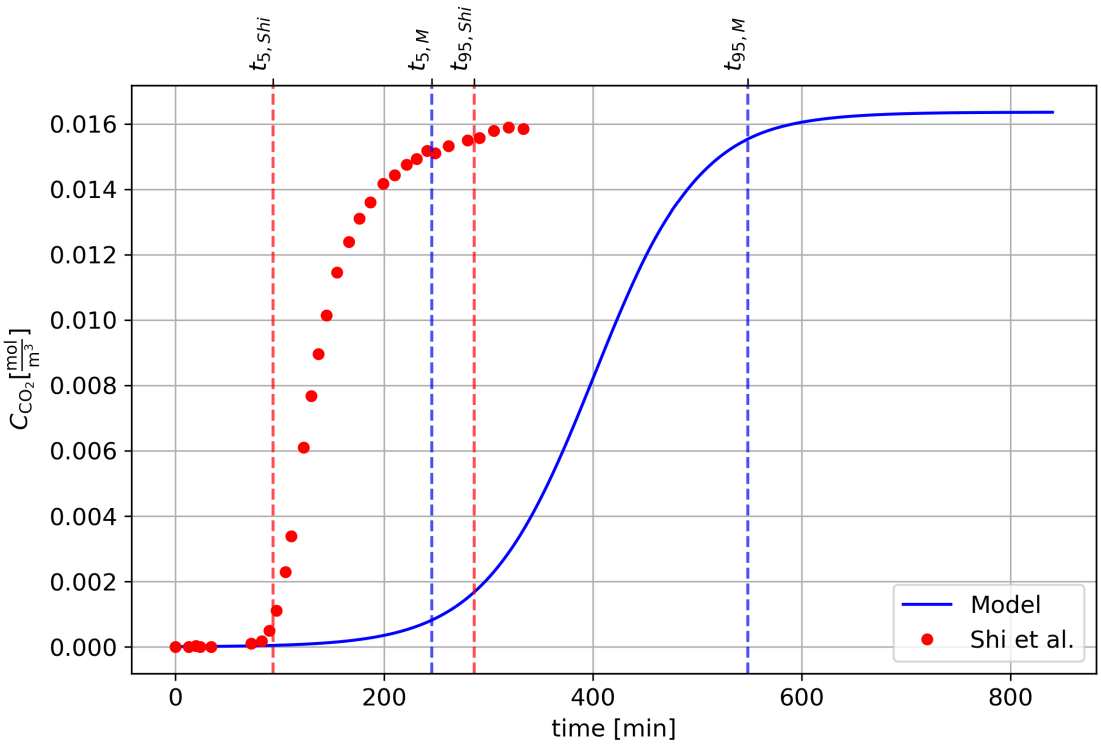

Figure 4.12: Breakthrough curves from experimental data from Shi et al, and predicted by the model under conditions from Shi et al.'s experiments [81]. t_5 and t_{95} mark the times of 5% and 95% breakthrough, respectively

the considered columns is not equal. Possible reasons for these discrepancies will be further discussed in Chapter 5.

While the time required for breakthrough does not match the experiment by Shi et al. [81], it can still be expected that qualitative conclusions from variations of geometries and conditions can be drawn from the model.

4.2.2. Comparison packed bed and monolith

The exemplary case of adsorption under low humidity is evaluated for both reactor models. In Figure 4.13, the breakthrough curves of both reactors with standard dimensions are shown. The monolith considered in this study has a higher porosity than the packed bed, resulting in increased length and lower interstitial velocity. It can be seen that the packed bed reactor exhibits a steeper breakthrough curve compared to the monolith. Additionally, the curves show a slight offset, with the monolith reaching the turning point later than the packed bed. This can be accredited to the difference in length of the contactors.

A steeper breakthrough curve generally indicates higher mass transfer efficiency, as the sorbent quickly saturates from initial breakthrough [13]. To estimate whether the flow in the contactor is dominated by convection or dispersion the Péclet number evaluated. It is a dimensionless number and defined as

$$\mathrm{Pe} = \frac{L v_s}{D_L} \tag{4.1}$$

with L being the reactor length, v_s the superficial velocity and D_L the dispersion coefficient. A high Péclet number indicates that the system is dominated by convective mass transfer, while the Péclet number is low for systems dominated by dispersion. In typical fixed bed adsorption columns convection dominates over dispersion and the Péclet number ranges between $50 - 500$ [71]. In the considered case, with the velocity $v_s = 0.04\,\mathrm{m/s}$, the Péclet number is ~ 275 for the packed bed and ~ 700 for the monolith, showing that dispersion is minor compared to convective transport. Thus, the difference in steepness of the two

reactors is not due to disperse effects, but to mass transfer limitations, which have a higher impact on the adsorption rate in the monolith due to a lower surface area of the sorbent.

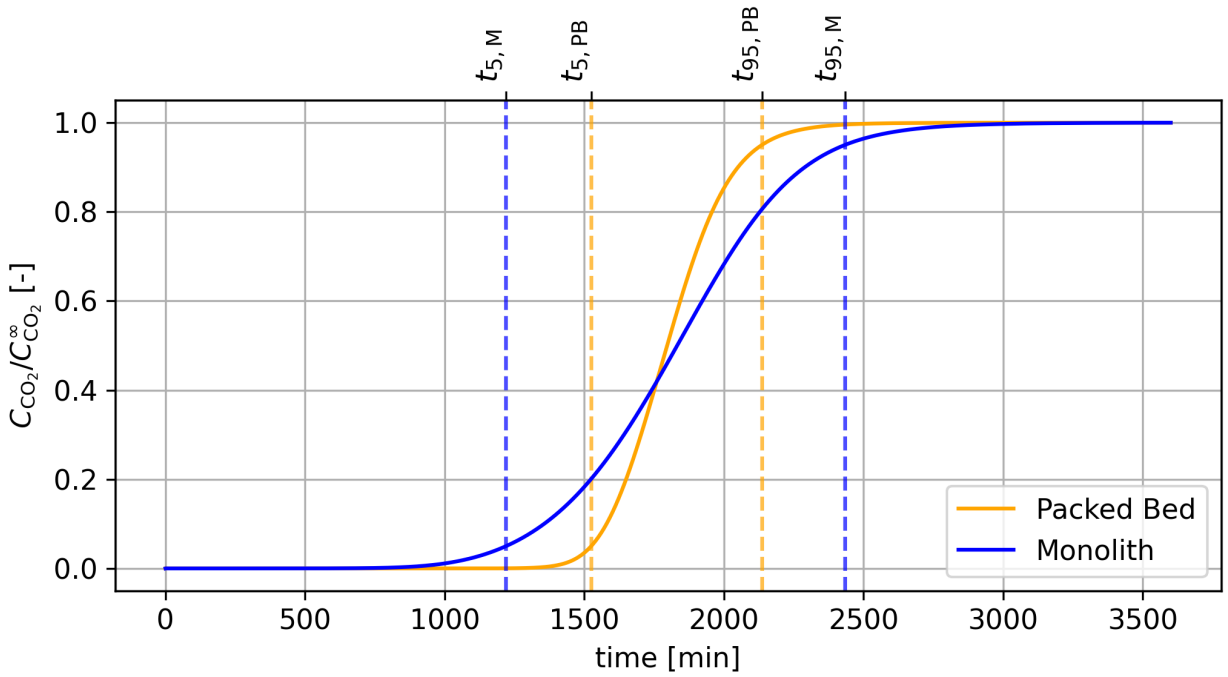

Figure 4.13: Normalized breakthrough curves of the packed bed and the monolith for the low RH adsorption case, indicated times mark 5% and 95% breakthrough.

To evaluate the efficiency of the usage of the sorbent, it is common to normalize the time with the stoichiometric time t_s which represents the time required to pass the amount of CO_2 equal to the total adsorption capacity through the column [71]. It is defined as

$$t_s = \frac{N_{tot}}{\dot{V} C_{\infty}} \tag{4.2}$$

where N_{tot} is the total adsorption capacity in mol, $\dot{V}$ the volumetric flow rate in $^{\mathrm{m}^3}/_{\mathrm{s}}$ and C^{∞} the inlet concentration in $^{\mathrm{mol}}/_{\mathrm{m}^3}$. The non-dimensionalised time scale is then defined as

$$\tau = \frac{t}{t_s}. \tag{4.3}$$

As the values defining the stoichiometric time is equal for both reactors considered, the normalisation only influences the absolute values. In an ideal reactor, breakthrough would start at $\tau = 1$, which means adsorption of its full capacity before breakthrough occurs, minimizing leakage and thus the energy required for maintaining the gas supply. Figure 4.14 shows the breakthrough curve on the stoichiometric time scale. Early breakthrough occurs at $\tau = 0.75$ in the packed bed reactor, while at $\tau = 0.5$ in the monolith. This indicates a more efficient utilization of the sorbent in the packed bed.

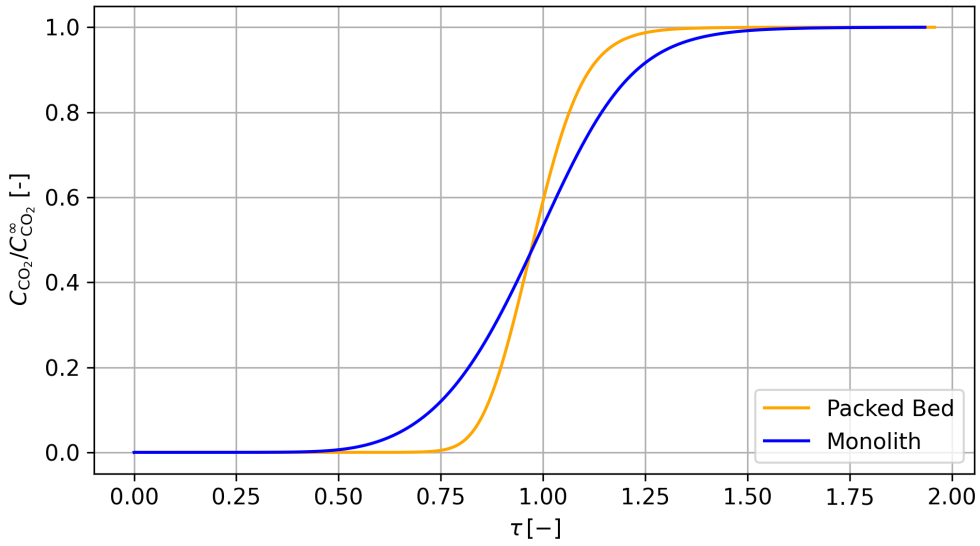

Figure 4.14: Normalized breakthrough curves of the packed bed and the monolith for the low RH adsorption case on a time scale normalized with the stoichiometric time.

4.2.3. Variation of humidity

The breakthrough curves for the different humidity levels in the packed bed reactor are shown in Figures 4.15a. They show that the breakthrough time increases with the humidity level. As humidity enhances the adsorption capacity, the total amount of carbon dioxide adsorbed is higher. The flow rate is constant for all the cases, which implies the same supply of carbon dioxide. As more CO_2 is adsorbed in the column, the breakthrough time increases. The slope of the curves is very similar, however shows a slight increase with the rise of humidity level. This difference is most clear in the period of early breakthrough, and indicates an influence of the chemical reaction rate, which is slower for the dry carbamate reaction. This difference is more relevant in the beginning of the process, as the CO_2 can adsorb in the outer regions of the particles, without being hindered by intra-particle diffusion. The same analysis is done for the results in the monolith, shown in Figure 4.15b. The offset between the curves of different humidity levels are similar to the behaviour in the packed bed. Differences in the slopes can not be identified, indicating less influence of the reaction rate on the overall uptake process, and thus a higher relevance of intra-sorbent diffusion.

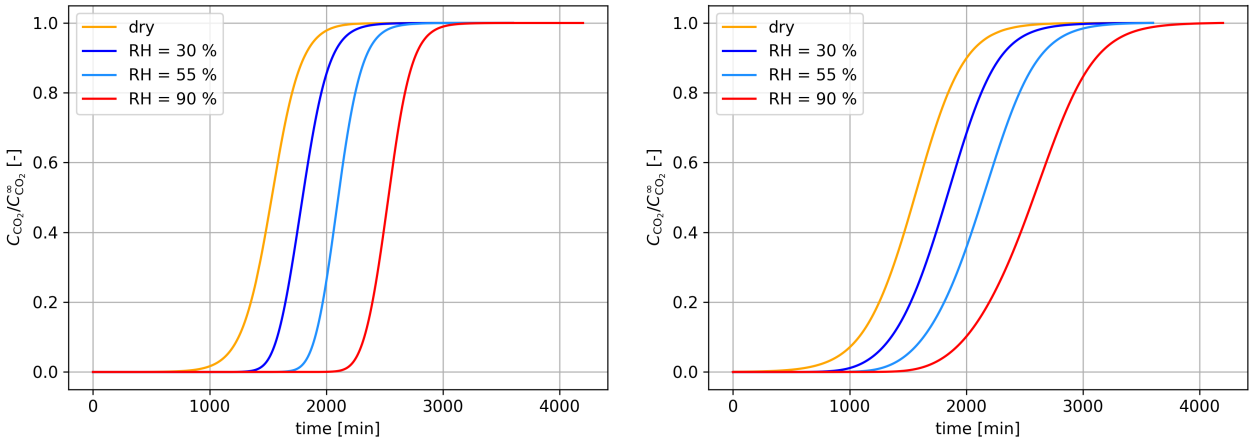

(a) Normalised breakthrough curves of the packed bed at dry conditions, low RH, medium RH and high RH

(b) Normalised breakthrough curves of the monolith at dry conditions, low RH, and high RH

Figure 4.15: Breakthrough curves of the packed bed and the monolith under the different considered humidity levels.

4.2.4. Variation of diffusion length

The diffusion length is varied to evaluate the influence of intra-sorbent mass transfer on the whole breakthrough behaviour. Figure 4.16 shows the breakthrough curves of the packed bed and the monolith of the exemplary case of low RH on the stoichiometric time scale for different intra-sorbent diffusion lengths *i.e.* varied particle size and wall thickness. The Figure shows that an increase of D_p and dw leads to a reduction of the slope of the breakthrough curves. It can further be seen that the increase has a stronger affect on the monolith, indicating that intra-sorbent diffusion is more important for this reactor. For a diffusion length of $D_p = dw = 100\,\mu\mathrm{m}$, intra-sorbent mass transfer effects become irrelevant and the adsorption process on the material is reaction limited. The breakthrough curves of the monolith and the packed bed coincide despite their difference in length and interstitial velocity, demonstrating that these differences are irrelevant for the overall uptake process.

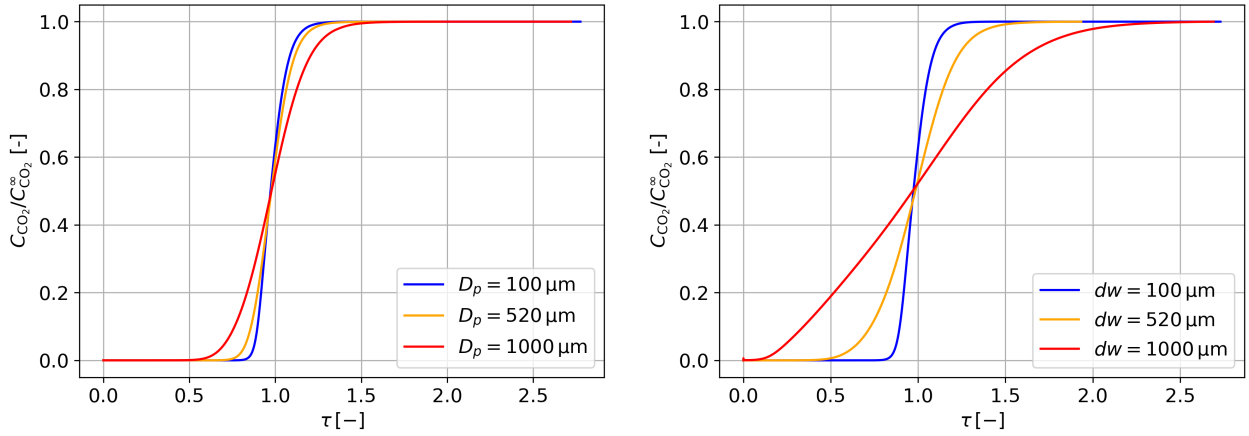

(a) Results for the packed bed reactor

(b) Results for the monolith

Figure 4.16: Normalised breakthrough curves of the low humidity case on the stoichiometric timescale τ for different diffusion lengths.

Evaluation of performance indicators

In this section, the performance indicators productivity and required electrical energy for the fan, as defined in Section 3.2.5 are evaluated. The values are calculated for $50\,\%$, $70\,\%$ and $95\,\%$ breakthrough.

Figure 4.17 illustrates the productivity of the packed bed and the monolith evaluated at different times, for the intra-sorbent diffusion lengths $D_p = dw = 520\,\mu\mathrm{m}$ and $D_p = dw = 1000\,\mu\mathrm{m}$. The values indicate a generally higher productivity of the packed bed compared to the monolith. The differences are more prominent for the evaluation at later stages of breakthrough, close to saturation of the sorbent, as the productivity of the monolith declines more compared to the packed bed. This follows from the steeper breakthrough curve of the packed bed. The differences are enhanced for the higher diffusion length.

The required energy for the fan is compared in Figure 4.18. It can be seen that the energy requirements for maintaining the flow through the packed bed are massively higher than for the monolith. For better visibility, the findings for the monolith are displayed on a different scale in Figure 8.4. To reach $95\,\%$ breakthrough, $4597.4\,\mathrm{J}$ are required for the packed bed, while only $23.5\,\mathrm{J}$ to power the fan for the monolith, which is a ~ 200 times higher energy consumption for the packed bed. With rising the particle size to $1000\,\mu\mathrm{m}$, the energy required for the fan until $95\,\%$ breakthrough in the packed bed is reduced by $95\,\%$, arriving at an energy consumption of $1410.9\,\mathrm{J}$. The energy saving is due to a significant reduction of the pressure drop over the bed. The energy required for the flow through the monolith increases with an increase of the intra-sorbent diffusion length, originating from slight increase in pressure drop due to a reduction in channel size, and the increase in time required to reach the breakthrough times considered. The required energy for $95\,\%$ breakthrough rises to $43.8\,\mathrm{J}$, which is an increase of $35\,\%$. Despite this, the energy consumption for achieving 95% breakthrough for the monolith remains substantially lower, being 32 times less than that of the packed bed.

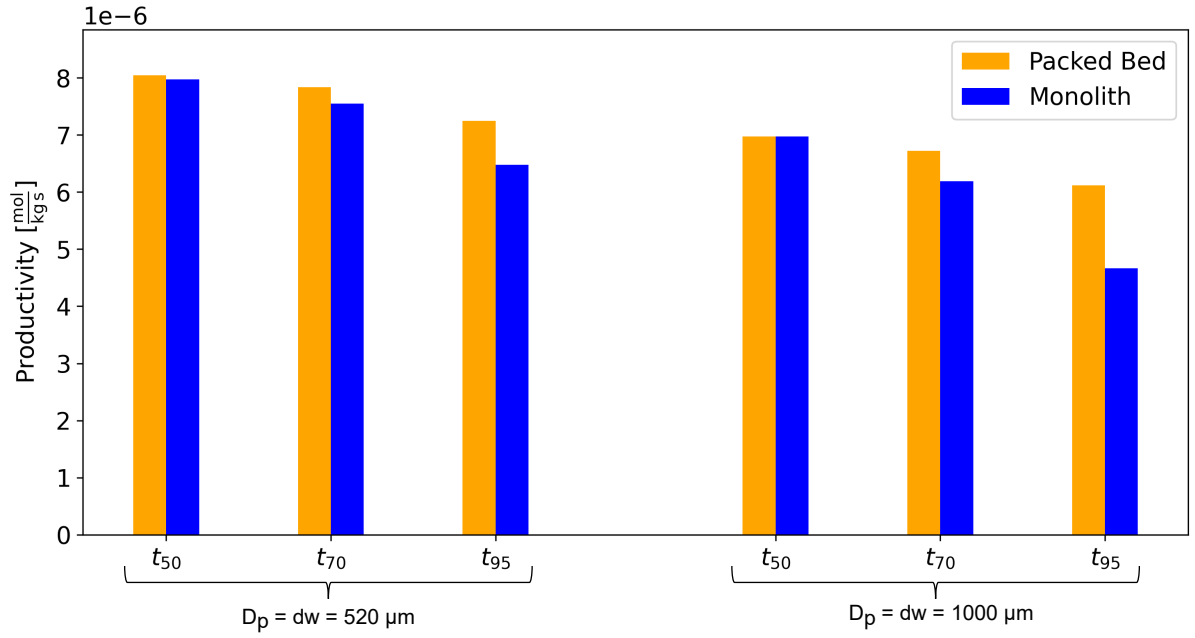

Figure 4.17: Productivity of the packed bed and monolith after reaching 50%, 70% and 95% breakthrough. Diffusion lengths $D_p = dw = 520\,\mu\text{m}$ and $D_p = dw = 1000\,\mu\text{m}$ are evaluated.

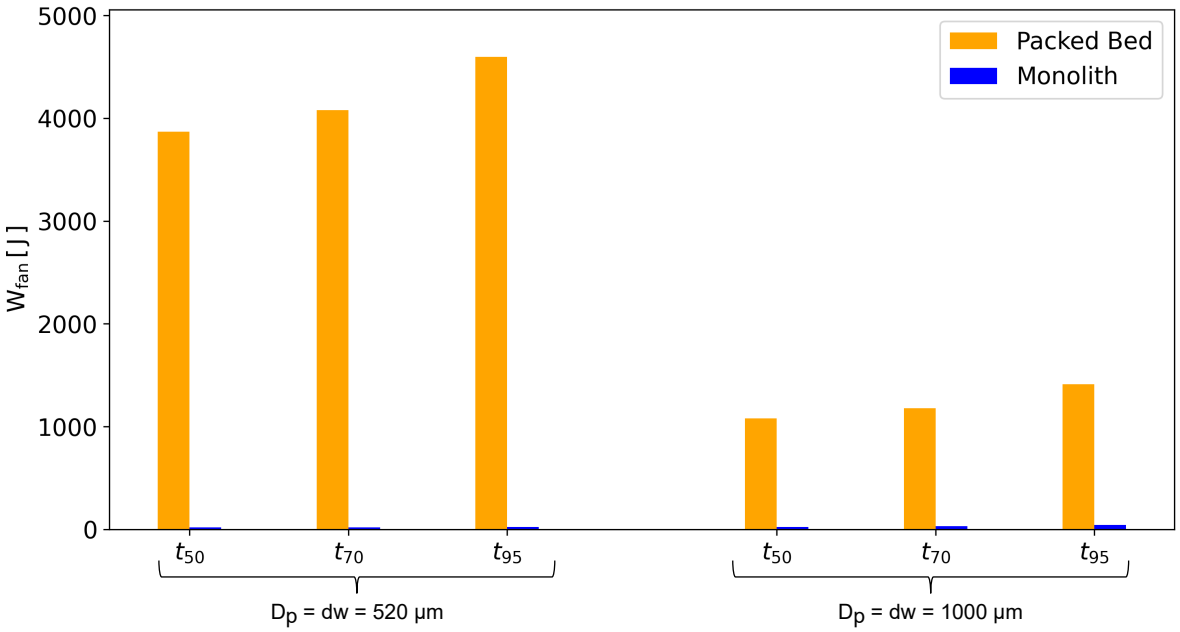

Figure 4.18: Energy consumed by the fan for the packed bed and monolith after 50%, 70% and 95% breakthrough. Diffusion lengths $D_p = dw = 520\,\mu\text{m}$ and $D_p = dw = 1000\,\mu\text{m}$ are evaluated.

4.2.5. Variation of velocity

For further evaluation of the differences between the contactors, two cases of different velocities are presented. The conditions considered correspond to the exemplary adsorption case under low RH.

Lower velocity

In the cases considered so far, dispersion does not play a role. This was shown by the evaluation of the Péclet number. In this section, the inflow rate is lowered so that dispersion plays a minor role in the column. It is chosen to be $\dot{V} = 6.48\,\mathrm{L/s}$, corresponding to a superficial velocity of $v_s = 5 \cdot 10^{-5}\,\mathrm{m/s}$. This corresponds to Péclet numbers $\mathrm{Pe} = 59.26$ in the packed bed, and $\mathrm{Pe} = 122.44$ in the monolith, making dispersion more relevant in the packed bed compared to the monolith. The breakthrough curves shift significantly to later times, which can be directly attributed to the lower flow rate.

They are presented on the stoichiometric time scale in Figure 4.19. The graph reveals that the lower flow rate increases the overall mass transfer efficiency in the column, as breakthrough occurs closer to $\tau = 1$. This is due to the lower velocity in the column increasing the residence time of the gas and thus the contact time of the gas and the sorbent. The differences between the monolith and the packed bed decrease suggesting that the uptake is limited by the supply rate instead of reactor specific processes.

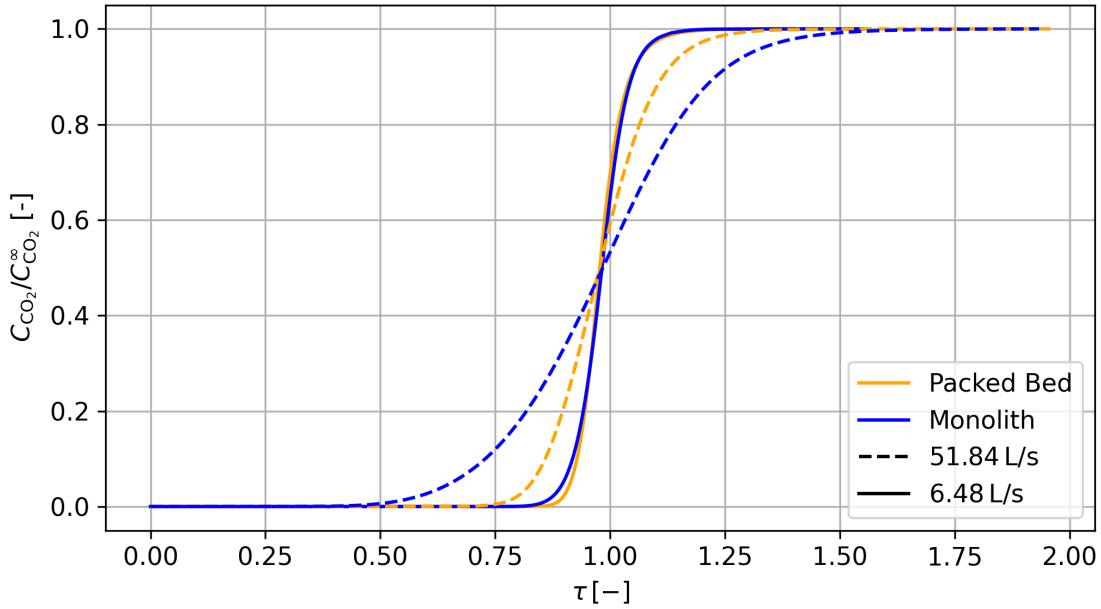

Figure 4.19: Breakthrough curves of the packed bed and the monolith under the standard volumetric flow rate in this work and the reduced one. The time scale is normalized with the stoichiometric time.

Constant fan power

As DAC involves significant energy costs to extract CO_2 from the atmosphere, energy savings are crucial. Additionally, unlike other adsorption column applications, the efficient use of the feed gas is less critical because the feed gas in DAC is simply ambient air, which is abundantly available. Therefore, an industrial perspective is adopted by maintaining a constant fan power between the monolith and packed bed reactors, rather than keeping the supply rate constant, allowing for a more practical comparison of their performance. The fan power required to maintain the volumetric flow rate of $\dot{V} = 51.84\,\mathrm{L/s}$ is $\dot{W}_{fan} = 6.89\,\mathrm{W}$ and is considered for this comparison. As the pressure drop over the monolith is substantially lower than over the packed bed, this fan power generates an increased volumetric flow rate of $\dot{V} = 772.21\,\mathrm{L/s}$, which corresponds to a superficial velocity of $v_s = 0.596\,m/s$. The standard dimensions for the reactors are used for this comparison. Figure 4.20 displays the breakthrough curve of the packed bed and the monolith under the fan power of $\dot{W}_{fan} = 6.89\,\mathrm{W}$. It can be seen that the effluent reaches the feed concentration 2.5 times earlier for the monolith than for the packed bed. The time after which $95\,\%$ breakthrough is reached is $t_{95,M} = 488.25\,\mathrm{min}$ for the monolith, and $t_{95,pb} = 2136.0\,\mathrm{min}$ for the packed bed, resulting in a 4.38 times higher energy consumption for the packed bed. This illustrates the energetic

advantage the monolith provides. The advantageous behaviour of the monolith can also be seen from its higher productivity compared to the monolith. The productivity at 50%, 70% and 95% breakthrough is illustrated in Figure 4.21. The differences between the values decreases for increasing considered breakthrough time, which is due to the steeper breakthrough curve of the packed bed. The productivity after 95% is 4.2 times higher in the monolith compared to the packed bed.

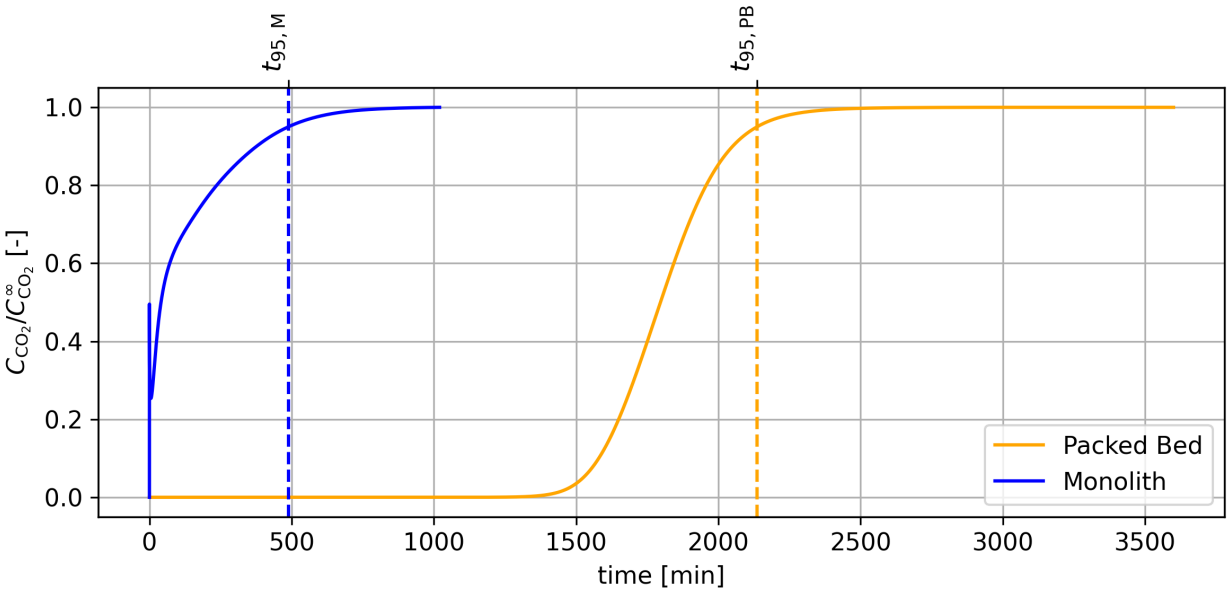

Figure 4.20: Breakthrough curves of the packed bed and the monolith under a constant fan power of $\dot{W}_{fan} = 6.89\,\mathrm{W}$, for the low RH adsorption case.

The result for the monolith shows immediate breakthrough up to a value of 0.5 times the feed concentration, stabilizing at $0.25 \cdot C^{\infty}_{CO_2}$. Then, the concentration slowly approaches the feed concentration, where it shows a change in slope after $100\,\mathrm{min}$. Here, the regime changes to being solely governed by intra-sorbent diffusion and reaction limitations, and the concentration profiles over the reactor length adapt a linear shape. This happens because the residence time in the column is short, and the CO_2 concentration inside the particles lags behind the concentration in the bulk fluid.

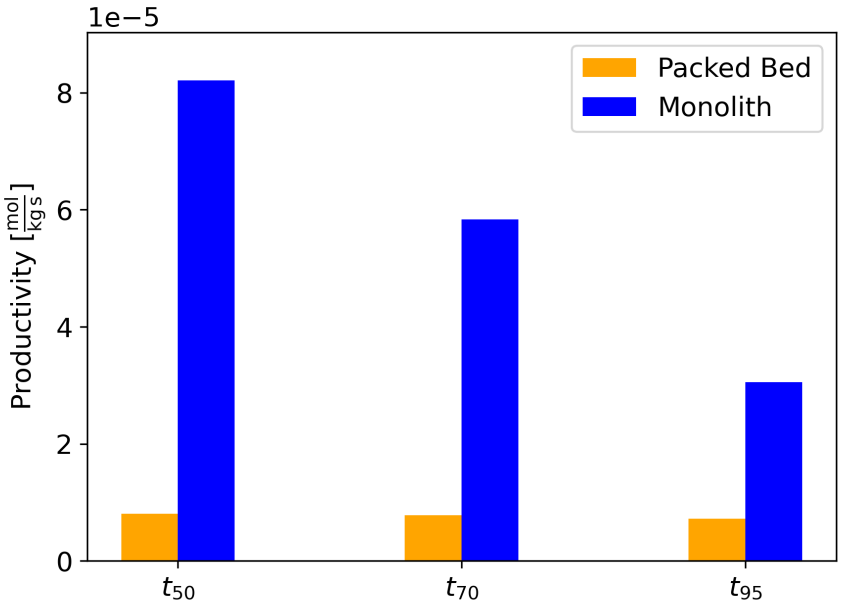

Figure 4.21: Productivity of the packed bed and the monolith after 50%, 70% and 95% breakthrough, at a constant fan power of $\dot{W}_{fan} = 6.89\,\mathrm{W}$. Results are for the low RH adsorption case.

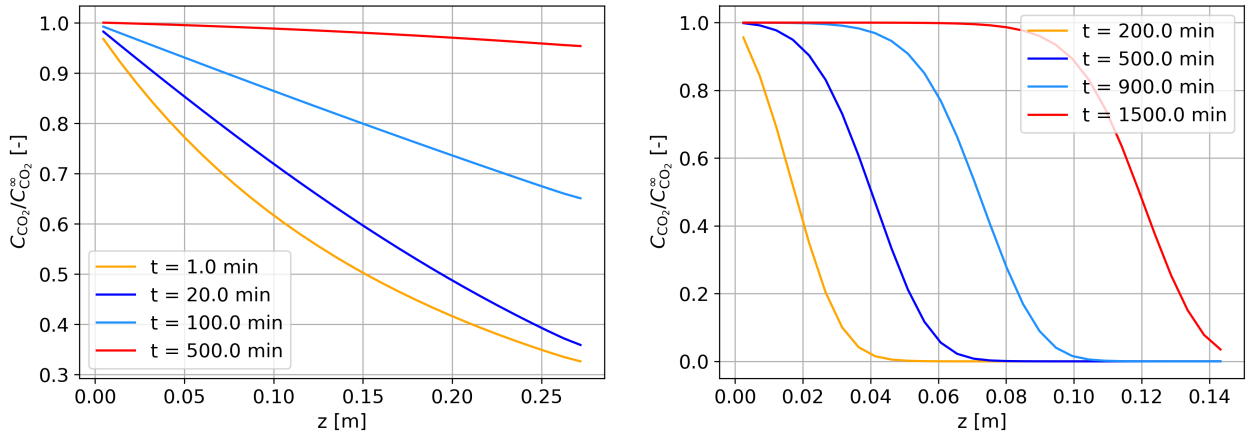

(a) monolith reactor

(b) packed bed reactor

Figure 4.22: Concentration profiles over the reactor length during adsorption under a constant fan power of $\dot{W}_{fan} = 6.89\,\mathrm{W}$. Results are for the low RH adsorption case.

4.2.6. Maxwell-Stefan model

In this section, the results of the contactor models applying the Fickian and the Maxwell-Stefan model on the intra-sorbent scale are compared. The comparison is done on the case with elevated particle size and wall thickness ($D_p = dw = 1000\,\mu\text{m}$), as intra-sorbent diffusion is more relevant here, and differences between the models thus larger. The results of the breakthrough curves for the packed bed and the monolith can be seen in Figure 4.23. They show that the curves are steeper under the application of Maxwell-Stefan equations compared to Fick's law. This is coherent with the observation in the particle model, that Fick's law underestimates the intra-sorbent diffusion. It can further be seen that the differences between the models are larger for the monolith, confirming the hypothesis that intra-sorbent diffusion is of higher importance compared to the packed bed.

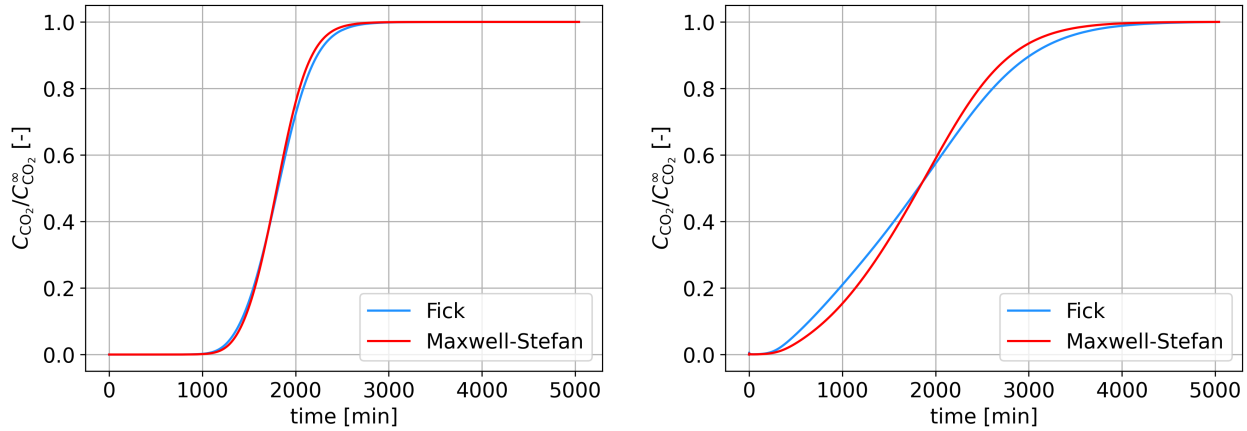

(a) Results for the packed bed reactor

(b) Results for the monolith reactor

Figure 4.23: Normalised breakthrough curves predicted by the Maxwell-Stefan and the Fickian model for adsorption under low RH

4.2.7. Desorption

While a constant gas velocity in the column is assumed for the adsorption model, the velocity in the desorption model is calculated based on the change in loading of the material. Typical desorption conditions are reduced pressure and elevated temperature. Purge gas might be applied to increase transport through convection. Numerical issues arise in the calculations, when the conditions of the desorption case considered in the particle model are applied. Due to the very low pressure, values become too small and the tolerances are too big for the solver to proceed. Also the consideration of a steam purge led to numerical difficulties, with instabilities prolonging the calculation and decreasing the quality of the results.

To demonstrate the principle of the model, a desorption case is run in dry conditions and under the consideration of nitrogen purge gas. While this is not a useful application for direct air capture, it is applied here for demonstrative reasons and as a starting point for future work. The pressure in the considered case is set to $P_{des} = 1 \cdot 10^4\,\text{Pa}$, the temperature is $T = 328\,\text{K}$ and the constant inlet velocity corresponds to a volumetric flow rate of nitrogen of $\dot{V} = 0.68\,^{\text{L}}/_{\text{s}}$.

Figure 4.24 shows the development of CO_2 concentration at the outlet of the packed bed over time. The development of the concentration profile is typical for a desorption process [13]. After a steep rise during the inital desorption, the concentration slowly decreases and approaches zero. Figure 4.25 shows the profiles of the interstitial velocity over the packed bed at different time steps. It can be seen that the velocity rises initially, exhibiting a linear rise over the column length. At around $t = 0.01\,\text{s}$ a peak in velocity is reached, after which the profiles decline until a constant value of the initial velocity is established throughout the column. In this study, desorption is modeled by applying the equilibrium conditions from the adsorption phase, while adjusting for changes in temperature and pressure, without explicitly simulating the heating and evacuation processes. Consequently, molecules that would normally desorb gradually during these phases are instead assumed to desorb instantaneously at the start of the desorp-

tion simulation. This immediate desorption results in a significant initial velocity peak. The magnitude of this peak increases under lower pressure conditions, which is why the low-pressure desorption scenario could not be solved. A similar issue arises when considering humidity; the rapid physical adsorption reaction of water leads to steep gradients in the simulation, causing numerical difficulties.

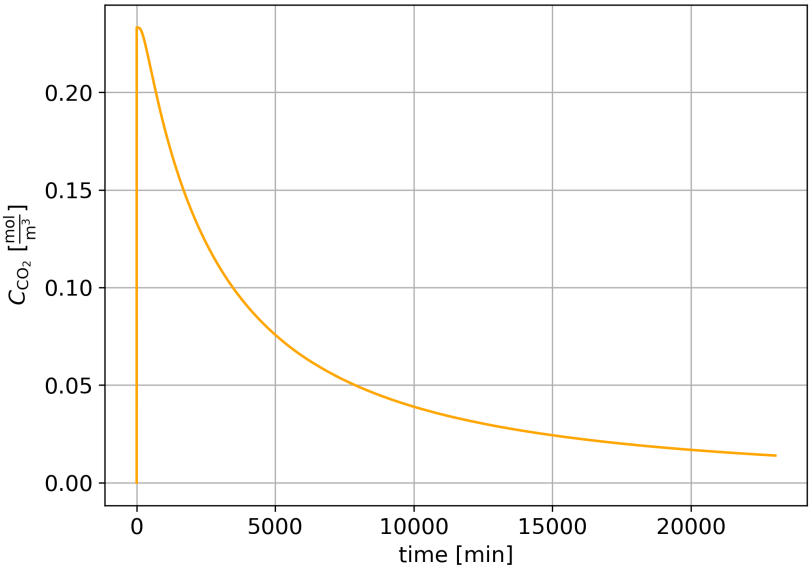

Figure 4.24: CO_2 concentration at the outlet of the packed bed during desorption with a nitrogen purge.

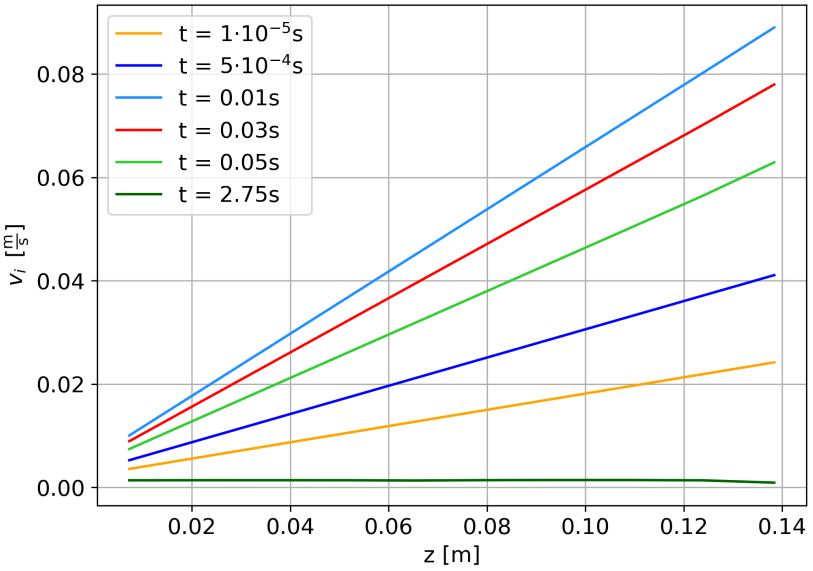

Figure 4.25: Interstitial velocity profiles over the packed bed at different time steps during desorption with a nitrogen purge.

5

Discussion

5.1. Particle model

The model on the particle scale was evaluated for different cases, varying the adsorption conditions in terms of humidity, as well as the characteristics of the sorbent in terms of particle size, pore size and pore structure.

While the model gives a good quantitative prediction of the adsorption isotherm in dry conditions (based on carbamate formation), it is limited to qualitative predictions for the isotherm under humid conditions. This leads to the presumption that more or other effects are relevant in the process of co-adsorption of carbon dioxide and water than considered. Li et al. [47] suggest the formation of hydronium carbamates dominating over bicarbonates, and accredit a critical role for the kinetics to the formation and solid-diffusion of different intermediates stabilizing water molecules after physical adsorption. Meanwhile, Kaneko and Lackner [36] extend the mechanisms considered in this study by taking hydration water around ions and, subsequent to the formation of bicarbonates, the reaction to carbonates into account. Both mechanisms are new suggestions for the chemical pathways of CO_2 adsorption under humid conditions and have not yet [36] or only in a limited study considering one material [47] been validated.

While appropriate data was available to fit the kinetics of the carbamate reaction, the kinetic parameters of the bicarbonate reaction bear uncertainties due to the limitation in available data of dynamic TGA measurements on co-adsorption. The diffusion effects could not be excluded when adjusting the kinetic parameters, and the fit relies on the predictions of the diffusion model. Furthermore, the temperature dependency could only be estimated from literature. Rigorous experimental data on small particles - and thus excluding diffusion limitations - under various humidity levels and temperatures would provide the basis to obtain accurate kinetic parameters describing the co-adsorption effects.

Under the considered conditions, the model reflects the increase in CO_2 loading on the material with increased humidity in the air well, and predicts a higher uptake rate under humid conditions. Pressure and temperature considered in this study correspond to the data used for the approximation of the thermodynamic parameters, giving confidence in the equilibrium loadings calculated. The particle size, pore size and tortuosity, which directly influence the diffusion rate, have significant influence on the uptake rate of carbon dioxide, which demonstrates the influence of intra-sorbent diffusion on the process. The model predicts the same threshold for the particle size from which intra-particle diffusion becomes relevant for the overall uptake process as experimental results [9], which validates the magnitude of the diffusion model. However, literature reports varying values for the structural properties of Lewatit (such as pore size), yielding uncertainty when comparing model predictions to experimental data. The current diffusion model assumes an average pore size and effective particle size, which represents an averaged estimation. The consideration of a pore size distribution (for example by including a parallel pore model, see Appendix 7) and particle size distribution would increase the accuracy of the model, and its applicability to different materials.

Differences between the Maxwell-Stefan and the Fickian model are present only in the adsorption case which is due to the chosen conditions. The differences between the models scale with the relevance of intra-sorbent diffusion on the whole process. Thus, the differences between the model might become relevant for different materials with differently shaped or bigger particles. Furthermore, they behave differently depending on the concentration of water, as the Maxwell-Stefan model considers multi-component effects, while Fick's law does not. The effect of the differences between the models however is small on the adsorbed species and the loading. For Lewatit, as considered in this work, the difference between the two models is near negligible and considering the larger computation time of the Maxwell-Stefan model, the application of the Fickian model is preferred. The application of the Maxwell-Stefan model might become relevant for larger or differently shaped sorbent structures.

The desorption case considered is close to vacuum and governed by Knudsen diffusion. In practice, desorption might be conducted under higher pressures, and under the application of a steam purge. Those conditions were not regarded in this work, as a mixture of steam and the desorbed CO_2 will show non-idealities, making the results on the particle scale with the assumption of ideal gases inappropriate.

5.2. Contactor model

The contactor model could not be validated with the experimental results from Shi et al. [82]. Although the experimental conditions as stated were adapted to the simulation, the model predicts delayed breakthrough together with a slightly more gradual breakthrough curve. The differences suggest a discrepancy in the capacity of the column between the experiment and the simulation. Possible reasons are uncertainties in the material parameters as well as the true experimental conditions. Shi et al. report different values in material-intrinsic properties such as sorbent density, sorbent porosity and tortuosity than reported by the manufacturer and other literature [46, 97, 91]. The sorbent density is directly connected to the loading calculated in the model, while the porosity and tortuosity have influence on the diffusion and thus uptake dynamics as shown in Section 4.1. The properties are adjusted for the validation case in the model, however they do not correspond to the values used in the development on the model. The lower density of the material reported by Shi et al. [82] leads to predictions of higher loading at the given concentration, disrupting the essential, intrinsic consistency between concentration and carbon dioxide loading of the model.

Due to the fact of only minor differences between the Maxwell-Stefan equations and Fick's law in the particle model, and the significant difference in computation times (~ 12 times higher for the Maxwell-Stefan model), the analysis of the contactors were done under the application of the Fickian model. However, in cases where the influence of intra-sorbent diffusion is more significant, the results of the two models exhibit considerable differences. Hence, in the modeling of configurations with a strong influence of intra-sorbent diffusion the choice of diffusion model is relevant for the overall adsorption process.

Comparisons of the packed bed and the monolith contactor revealed a steeper breakthrough curve of the packed bed in the base case with standard dimensions and relative humidity of $30\,\%$. Variations in the humidity levels led to delayed breakthrough with similar slope of the breakthrough curves in both the monolith and the packed bed, reflecting the larger total uptake under humid conditions. A variation of the intra-sorbent diffusion length shows that the monolith exhibits a higher dependency on this parameter, indicating a higher relevance of intra-sorbent diffusion. This observation can be explained by the intrinsic geometry of the sorbent in the two reactor configurations. In a packed bed, the spherical shape of the sorbent results in a significant portion of its volume being concentrated in the outer regions. This configuration reduces the diffusion length for the gas, allowing it to access a large fraction of the adsorption sites more efficiently. In contrast, the sorbent in a monolith is structured as a straight wall, where the increase in accessible material is linear with respect to the distance of intra-sorbent diffusion. Generally, the sorbent in the monolith exhibits a lower specific surface area compared to that in the packed bed. This is a general phenomenon connected to the penetration theory, applicable for heat and mass transfer, and addressed for instance in Bird et al. [7].

In the cases considered in this study, this effect causes significant differences between the breakthrough curves of the contactors for a sorbent thickness $D_p = dw = 520\,\mu\mathrm{m}$, and increases to higher differences for $D_p = dw = 1000\,\mu\mathrm{m}$. Larger particle sizes in the packed bed lead to a slight decrease of efficiency and

productivity, while an increase of the wall thickness of the monolith showed more significant effects on the breakthrough time. Increasing the particle size in the packed bed also leads to a substantial decrease of pressure drop over the reactor, leading to significant savings in electricity costs for the blower. This demonstrates a trade-off between productivity and electricity costs, where the reduction in required electricity is higher ($\times 3$ lower) than the penalty in productivity ($\times 0.16$ lower) for the considered particle sizes. The model developed in this work generally offers a suitable method for determining the optimal particle size to balance this trade-off, thereby supporting reactor design. Constructing monoliths with very thin walls bears challenges to maintain stability and might not be feasible. The considered thickness of $520\,\mu\mathrm{m}$ was found to be applied in a commercially available monolith with a length of $\sim 15\,\mathrm{cm}$ [84], but scaling up the total size would most likely also require thicker walls to ensure the stability of the monolith. Thus, the intra-sorbent diffusion will play a significant role in monoliths applied for Direct Air Capture. Yet, the monolith demonstrates substantially lower pressure drops, offering massive energy savings for the operation of the fan required to maintain flow through the reactor. This results in a trade-off between productivity and energy required by the fan between the two reactors. In the considered configuration, 200 times more electrical energy for the blower is required to reach 95% breakthrough in the packed bed compared to the monolith. This considerably outweighs the monolith's disadvantage in productivity, which is still 80% of the productivity of the packed bed in the case with the highest difference (after 95% breakthrough for $D_p = dw = 1000\,\mu\mathrm{m}$). Applying equal fan powers highlights the advantages of the monolith, and reveals a 4.2 times higher productivity after 95% breakthrough and a thus 4.3 times lower energy consumption with respect to the packed bed under these conditions. In this case, the monolith's breakthrough curve shows immediate breakthrough and a more gradual slope compared to the packed bed, suggesting a less efficient utilization of the feed. However, in Direct Air Capture, where ambient air is the feed and is abundantly available, the column's efficiency is less critical compared to factors such as productivity and energy costs.

The numerical challenges encountered in desorption cases within the contactor model stem from the substantial quantity of species that desorb during the heating and evacuation phases. Since these steps are not explicitly modeled in this study, the abrupt change in conditions causes a sudden release of a large number of desorbing molecules, resulting in steep concentration and velocity gradients within the column. These issues become particularly severe at very low desorption pressures and in the presence of water, due to the rapid physical adsorption and desorption of water. To prevent this rapid increase and the associated numerical difficulties, it is necessary to explicitly model the heating and evacuation steps.

6

Conclusion and Recommendations

This thesis aimed to address the challenges in modeling the adsorption and desorption processes in DAC, particularly focusing on the complexities introduced by the diverse porous structures of the sorbent materials and the effects of humidity. The motivation for this research stemmed from the limitations of existing models, which fail to incorporate the full spectrum of mass transfer processes, or do not consider the significant effects of humidity on the process. By developing a comprehensive mass transfer and reaction kinetics model at the particle scale, this work sought to bridge these gaps, providing a more accurate and adaptable framework for predicting the performance of amine-functionalized sorbents in DAC applications.

All mechanisms transporting CO_2 and water from the bulk around the particle, through the pores of the materials until reaching and adsorbing to the amine site are considered in the developed model. The findings give clarity over their relevance for adsorption and desorption.

- **Film Diffusion** The model shows that film diffusion is fast compared to diffusion within the sorbent. Thus, it does not limit the adsorption process.
- **Pore Diffusion** It was found that pore diffusion influences the uptake rate, where the magnitude of its influence depends on the pore structure and particle size. Under the considered conditions, pore diffusion is relevant for the uptake process for particles with a diameter $\gtrsim 200\,\mu\mathrm{m}$, which is coherent with experimental results [9]. The structure of the material was represented by including the effective particle size $D_{p,eff}$, the average pore size $d_{p,avg}$, porosity ε_s and tortuosity τ_p. While these parameters were sufficient to correctly predict the magnitude of diffusion through the pores, accuracy and applicability of the model to different materials can be increased by including a particle size and pore size distribution. While the representation by Fick's law is simplified compared to the Maxwell-Stefan equations, the differences between the models on the overall adsorption process are slight for the considered material and conditions, making both models appropriate. With an increase of the particle size, the pore size or the tortuosity, and thus essentially an increase of the relevance of intra-particle mass transfer, the differences between the models can become significant. Under the considered desorption conditions, Knudsen diffusion is the relevant diffusion mechanism, hence the predictions of the two models are the same. The influence of pore diffusion compared to other phenomena on the process is the same as for the adsorption process.
- **Surface Diffusion** On the basis of findings in literature [27] and estimations of the magnitude of surface diffusion, it was shown to be irrelevant for the overall process. Hence, it was not further considered in the model.
- **Chemical Reaction** The kinetics of the chemical reactions influence the uptake on a particle scale together with pore diffusion. The adsorption reaction was modeled through the consideration of physical adsorption of water, carbamate and bicarbonate formation. The respective reactions were considered and parameterized through the thermodynamic values of reaction enthalpy and entropy, and kinetic factors determined by and Arrhenius factor and the activation energy. In order to set the maximum loading of CO_2 on the material, the concentration of amine sites is considered.

The reaction model does not reflect experimental results quantitatively over large ranges of pressure and temperature (and thus does not represent an accurate isotherm model), but it was found to describe the shape of the isotherms qualitatively, applicable for different materials. The kinetics of the chemical reaction of the formation of carbamates is in coherence with the magnitude of pore diffusion, as experimental results of Bos et al. [9] were validated. The kinetic parameters of the bicarbonate reaction were estimated from experiments and values in literature, and require further validation with appropriate data.

Hence, the results of the particle model show that pore diffusion and reaction kinetics govern the uptake dynamics on the sorbent. Which mechanism dominates depends on the particle size, pore structure as well as temperature and pressure conditions. The particle scale model implemented in a packed-bed reactor model could not be validated with the experimentally obtained breakthrough curves from Shi et al. [82]. While the slope of the breakthrough curves are similar, the total capacity between the experiment and the simulation differs. Multiple reasons might contribute to the discrepancies between the model and the experimental data, including uncertainties in the material parameters and possible differences between the experimental vs. simulation conditions. A detailed experimental study on breakthrough with Lewatit is required to gain certainty in the comparison. Despite the lack of experimental validation, the contactor model remains applicable for comparing the performance of a fixed-bed reactor and a monolith, as both models are based on the same fundamental principles.

The comparison at equal volumetric flow rates indicates that the packed-bed reactor generally produces steeper breakthrough curves and consequently, offers a more efficient use of the sorbent than the monolith, as well as a higher productivity ($\sim 10 - 24\%$ at the same diffusion length). This difference is primarily attributed to greater intra-sorbent mass transfer limitations in the monolith, resulting from its geometric configuration. The reduced specific surface area and the sorbent arrangement within the monolith make diffusion limitations particularly significant. Additionally, in realistic, scaled-up reactors, the monolith walls are expected to be wider than the particles in a packed bed due to stability concerns. As a result, intra-sorbent diffusion limitations are anticipated to have a greater impact on the overall process in the monolith compared to the packed bed.

Under the considered volumetric flow rate of $51.84\,\mathrm{L/s}$, dispersive effects were minor in the contactors, making the breakthrough time limited by the supply rate, intra-sorbent diffusion and chemical reaction rate, where their relevance depend on the diffusion length. In a regime where dispersive effects are governing, the residence time is increased such that intra-sorbent diffusion effects are minor and the uptake in the reactors is limited by the supply rate. For an increased flow rate in the monolith (in the case of constant fan power), the breakthrough time was mainly governed by intra-sorbent mass transfer and chemical reaction rate.

The profoundly lower pressure drop over the monolith, offers the potential of large energy savings for the operation of the fan required to maintain the flow through the reactor. The energy savings for the monolith outweigh its disadvantage in productivity, as up to 200 times less electrical energy is required to power the process. With equal fan power for both contactors, the monolith can achieve a 4.2 times higher productivity, which highlights its advantage. Although the packed bed shows higher efficient utilization of the feed, this is less critical for the application of DAC compared to productivity and energy costs, due to the reason that the feed is ambient air which is abundantly available.

This study shows the large potential monolith reactors offer on energy savings during operation, while maintaining a similar productivity compared to the packed bed. To determine which contactor is more advantageous, the reactors must be evaluated alongside other factors, such as the feasibility of producing thin monolith structures and the cost differences in manufacturing beads for a packed bed versus a monolith. Given the degradation of amine-functionalized materials over multiple cycles, this aspect can become of significant impact. Addressing manufacturing constraints in detail, however, is beyond the scope of this study.

The explicit modeling of intra-sorbent diffusion and reaction kinetics, allows for analysis of their influences under different conditions and geometries. Although the model requires improvements in accuracy, this study demonstrates the potential of a rigorous mass transfer model for further research in sorbent and reactor design. Given the significant impact of intra-sorbent mass transfer on uptake dynamics, it should be a central focus in future research on DAC process modeling.

6.1. Recommendations

The accuracy of the model for isotherms of co-adsorption can be enhanced, once a better understanding of the chemical mechanisms is established. Given that intermediates from water adsorption [36] or the formation of hydronium carbamates [47] may influence the process, additional research is required before the isotherm model can be refined by adjusting to these mechanisms. Certainty in the reaction kinetics, specifically under the influence of water, can be obtained by gathering more suitable dynamic TGA data for the co-adsorption of carbon dioxide and water under varying temperature conditions. This data should be obtained under the consideration of small particles, to exclude intra-sorbent diffusion effects. Furthermore, the model should be extended with the consideration of heat transfer effects, accounting for changes in temperature due to heat of adsorption. The diffusion model can be improved by including the consideration of a pore size and particle size distribution, and comparing different pore structure models such as the parallel or the random pore model [37]. An experimental analysis on sorbents with larger particles and of varying shape would provide valuable data for further refinement of the diffusion model. Further detailed breakthrough experiments with different geometries and inlet conditions are required to validate the model or gain insights on the discrepancies between the model and experimental results. This way, reliability of further predictions can be enhanced.

This study highlights the large potential of using monoliths as contactors in Direct Air Capture (DAC), particularly due to their substantial energy savings on required fan power compared to packed beds. Further research should focus on the feasibility and cost-effectiveness of producing these structures, which heavily depends on their design. The issue of sorbent degradation over multiple cycles makes the cost of producing the sorbent structures especially critical. Addressing the stability and durability limitations of monoliths made from amine-functionalized sorbents is essential for their successful application in DAC. Consequently, scaling up these reactors to larger sizes, such as those required for pilot-scale operations, should be a key research priority.

To maintain low pressure drops while enhancing the sorbent surface area and overall efficiency, innovative contactor designs are essential. One approach could involve optimizing the shape of monolith walls to minimize the impact of intra-sorbent diffusion limitations, with only a marginal increase in pressure drop. Similarly, the shape of the channels could be adjusted to increase flow efficiency. Another strategy could be the development of hybrid contactors that combine the benefits of monolith and packed bed reactors, such as layered designs or parallel configurations.

The evaluation of reactor designs that cannot be adequately represented by a 1-dimensional model necessitates the application of computational fluid dynamics (CFD). Given the importance of intra-sorbent mass transfer, integrating the findings of this study into CFD models is recommended. For instance, incorporating the 1-dimensional particle-scale model into 3-dimensional CFD simulations could pave the way for predictions of the performance of complex reactor designs.

References

[1] W. Richard Alesi and John R. Kitchin. "Evaluation of a primary amine-functionalized ion-exchange resin for CO 2 capture". In: *Industrial and Engineering Chemistry Research* 51 (19 May 2012), pp. 6907–6915. ISSN: 08885885. DOI: 10.1021/ie300452c.

[2] Habib Azarabadi and Klaus S. Lackner. "A sorbent-focused techno-economic analysis of direct air capture". In: *Applied Energy* 250 (Sept. 2019), pp. 959–975. ISSN: 03062619. DOI: 10.1016/j.apenergy.2019.04.012.

[3] Elliott P Barrett, Leslie G Joyner, and Paul P Halenda. "The determination of pore volume and area distributions in porous substances. I. Computations from nitrogen isotherms". In: *Journal of the American Chemical society* 73.1 (1951), pp. 373–380.

[4] Ian H. Bell et al. "Pure and Pseudo-pure Fluid Thermophysical Property Evaluation and the Open-Source Thermophysical Property Library CoolProp". In: *Industrial & Engineering Chemistry Research* 53.6 (2014), pp. 2498–2508. DOI: 10.1021/ie4033999. eprint: http://pubs.acs.org/doi/pdf/10.1021/ie4033999. URL: http://pubs.acs.org/doi/abs/10.1021/ie4033999.

[5] Youssef Belmabkhout, Guy De Weireld, and Abdelhamid Sayari. "Amine-bearing mesoporous silica for CO2 and H2S removal from natural gas and biogas". In: *Langmuir* 25 (23 Dec. 2009), pp. 13275–13278. ISSN: 07437463. DOI: 10.1021/la903238y.

[6] Christoph Beuttler, Louise Charles, and Jan Wurzbacher. "The Role of Direct Air Capture in Mitigation of Anthropogenic Greenhouse Gas Emissions". In: *Frontiers in Climate* 1 (Nov. 2019). ISSN: 26249553. DOI: 10.3389/fclim.2019.00010.

[7] R Byron Bird. "Transport phenomena". In: *Appl. Mech. Rev.* 55.1 (2002), R1–R4.

[8] Praveen Bollini, Stephanie A. Didas, and Christopher W. Jones. "Amine-oxide hybrid materials for acid gas separations". In: *Journal of Materials Chemistry* 21 (39 Oct. 2011), pp. 15100–15120. ISSN: 09599428. DOI: 10.1039/c1jm12522b.

[9] M. J. Bos et al. "Study on transport phenomena and intrinsic kinetics for CO2 adsorption in solid amine sorbent". In: *Chemical Engineering Journal* 377 (Dec. 2019). ISSN: 13858947. DOI: 10.1016/j.cej.2018.11.072.

[10] Katherine Calvin et al. *IPCC, 2023: Climate Change 2023: Synthesis Report. Contribution of Working Groups I, II and III to the Sixth Assessment Report of the Intergovernmental Panel on Climate Change [Core Writing Team, H. Lee and J. Romero (eds.)]. IPCC, Geneva, Switzerland.* Ed. by Paola Arias et al. July 2023. DOI: 10.59327/IPCC/AR6-9789291691647.

[11] Arjun Cherevotan, Jithu Raj, and Sebastian C. Peter. *An overview of porous silica immobilized amines for direct air CO2capture*. Dec. 2021. DOI: 10.1039/d1ta05961k.

[12] Sunho Choi, Jeffrey H. Drese, and Christopher W. Jones. *Adsorbent materials for carbon dioxide capture from large anthropogenic point sources*. 2009. DOI: 10.1002/cssc.200900036.

[13] E. L. Cussler. *Diffusion : mass transfer in fluid systems*. Third edition. Cambridge ; Cambridge University Press, 2009. URL: http://catdir.loc.gov/catdir/enhancements/fy0834/2008018927-d.html.

[14] Radu Custelcean et al. "Direct air capture of CO2 with aqueous peptides and crystalline guanidines". In: *Cell Reports Physical Science* 2 (4 Apr. 2021). ISSN: 26663864. DOI: 10.1016/j.xcrp.2021.100385.

[15] Andrzej Cybulski and Jacob A Moulijn. *Structured catalysts and reactors*. CRC press, 2005.

[16] Sandipan Kumar Das. "General Dusty Gas Model for porous media with a specified pore size distribution". In: *Chemical Engineering Science* 203 (Aug. 2019), pp. 293–301. ISSN: 00092509. DOI: 10.1016/j.ces.2019.03.085.

[17] Stephanie A. Didas et al. “Amine-Oxide Hybrid Materials for CO2 Capture from Ambient Air”. In: *Accounts of Chemical Research* 48 (10 Oct. 2015), pp. 2680–2687. ISSN: 15204898. DOI: 10.1021/acs.accounts.5b00284.

[18] Stephanie A. Didas et al. “Effect of amine surface coverage on the Co-adsorption of CO2 and water: Spectral deconvolution of adsorbed species”. In: *Journal of Physical Chemistry Letters* 5 (23 Dec. 2014), pp. 4194–4200. ISSN: 19487185. DOI: 10.1021/jz502032c.

[19] Stephanie A. Didas et al. “Role of amine structure on carbon dioxide adsorption from ultradilute gas streams such as ambient air”. In: *ChemSusChem* 5 (10 2012), pp. 2058–2064. ISSN: 1864564X. DOI: 10.1002/cssc.201200196.

[20] Jere Elfving and Tuomo Sainio. “Kinetic approach to modelling CO2 adsorption from humid air using amine-functionalized resin: Equilibrium isotherms and column dynamics”. In: *Chemical Engineering Science* 246 (Dec. 2021). ISSN: 00092509. DOI: 10.1016/j.ces.2021.116885.

[21] Jere Elfving et al. “Modelling of equilibrium working capacity of PSA, TSA and TVSA processes for CO2 adsorption under direct air capture conditions”. In: *Journal of CO2 Utilization* 22 (Dec. 2017), pp. 270–277. ISSN: 22129820. DOI: 10.1016/j.jcou.2017.10.010.

[22] Norman Epstein. “On tortuosity and the tortuosity factor in flow and diffusion through porous media”. In: *Chemical Engineering Science* 44.3 (1989), pp. 777–779. ISSN: 0009-2509. DOI: https://doi.org/10.1016/0009-2509(89)85053-5.

[23] María Erans et al. *Direct air capture: process technology, techno-economic and socio-political challenges*. Feb. 2022. DOI: 10.1039/d1ee03523a.

[24] Sabri Ergun. “Fluid flow through packed columns”. In: *Chemical engineering progress* 48.2 (1952), p. 89.

[25] Joel H Ferziger and Milovan Perić. *Computational methods for fluid dynamics*. Springer, 2002.

[26] Edward N. Fuller, Paul D. Schettler, and J. Calvin. Giddings. “New method for prediction of binary gas-phase diffusion coefficients”. In: *Industrial & Engineering Chemistry* 58.5 (1966), pp. 18–27. DOI: 10.1021/ie50677a007. URL: https://doi.org/10.1021/ie50677a007.

[27] Kun Ge et al. “Modeling CO2 adsorption dynamics within solid amine sorbent based on the fundamental diffusion-reaction processes”. In: *Chemical Engineering Journal* 364 (May 2019), pp. 328–339. ISSN: 13858947. DOI: 10.1016/j.cej.2019.01.183.

[28] Christoph Gebald et al. “Single-component and binary CO2 and H2O adsorption of amine- functionalized cellulose”. In: *Environmental Science and Technology* 48 (4 Feb. 2014), pp. 2497–2504. ISSN: 0013936X. DOI: 10.1021/es404430g.

[29] *Global Thermostat unveils one of the world’s largest units for removing carbon dioxide directly from the air — web.archive.org*. https://web.archive.org/web/20231106145141/https://www.globalthermostat.com/news-and-updates/global-thermostat-colorado-headquarters. [Accessed 07-03-2024]. 2023.

[30] Alain Goeppert et al. *Air as the renewable carbon source of the future: An overview of CO 2 capture from the atmosphere*. July 2012. DOI: 10.1039/c2ee21586a.

[31] Jannis Hack, Nobutaka Maeda, and Daniel M. Meier. *Review on CO2Capture Using Amine- Functionalized Materials*. Nov. 2022. DOI: 10.1021/acsomega.2c03385.

[32] Max Hefti and Marco Mazzotti. “Postcombustion CO2 Capture from Wet Flue Gas by Temperature Swing Adsorption”. In: *Industrial and Engineering Chemistry Research* 57 (45 Nov. 2018), pp. 15542–15555. ISSN: 15205045. DOI: 10.1021/acs.iecr.8b03580.

[33] Adam Holewinski, Miles A. Sakwa-Novak, and Christopher W. Jones. “Linking CO2 Sorption Performance to Polymer Morphology in Aminopolymer/Silica Composites through Neutron Scattering”. In: *Journal of the American Chemical Society* 137 (36 Sept. 2015), pp. 11749–11759. ISSN: 15205126. DOI: 10.1021/jacs.5b06823.

[34] Christopher W. Jones. “CO2 capture from dilute gases as a component of modern global carbon management”. In: *Annual Review of Chemical and Biomolecular Engineering* 2 (July 2011), pp. 31–52. ISSN: 19475438. DOI: 10.1146/annurev-chembioeng-061010-114252.

[35] Wonho Jung and Kwang Soon Lee. “Isotherm and kinetics modeling of simultaneous CO2 and H2O adsorption on an amine-functionalized solid sorbent”. In: *Journal of Natural Gas Science and Engineering* 84 (Dec. 2020). ISSN: 18755100. DOI: 10.1016/j.jngse.2020.103489.

[36] Yuta Kaneko and Klaus S. Lackner. “A general binary isotherm model for amines interacting with CO2 and H2O”. In: *Physical Chemistry Chemical Physics* 25 (20 Apr. 2023), pp. 13877–13891. ISSN: 14639076. DOI: 10.1039/d3cp00624g.

[37] Jörg Kärger, Douglas M. Ruthven, and Doros Nicolas Theodorou. *Diffusion in nanoporous materials*. Hoboken: John Wiley & Sons, 2012. ISBN: 9783527651276.

[38] David W. Keith et al. “A Process for Capturing CO2 from the Atmosphere”. In: *Joule* 2 (8 Aug. 2018), pp. 1573–1594. ISSN: 25424351. DOI: 10.1016/j.joule.2018.05.006.

[39] Rajesh A. Khatri et al. “Thermal and chemical stability of regenerable solid amine sorbent for CO2 capture”. In: *Energy and Fuels* 20 (4 July 2006), pp. 1514–1520. ISSN: 08870624. DOI: 10.1021/ef050402y.

[40] R. Krishna and J. A. Wesselingh. *Review article number 50: The Maxwell-Stefan approach to mass tranfer*. Mar. 1997. DOI: 10.1016/S0009-2509(96)00458-7.

[41] Amrit Kumar et al. “Direct Air Capture of CO 2 by Physisorbent Materials”. In: *Angewandte Chemie* 127 (48 Nov. 2015), pp. 14580–14585. ISSN: 0044-8249. DOI: 10.1002/ange.201506952.

[42] Hyuk Taek Kwon et al. “Aminopolymer-Impregnated Hierarchical Silica Structures: Unexpected Equivalent CO2 Uptake under Simulated Air Capture and Flue Gas Capture Conditions”. In: *Chemistry of Materials* 31 (14 July 2019), pp. 5229–5237. ISSN: 15205002. DOI: 10.1021/acs.chemmater.9b01474.

[43] Klaus Lackner et al. *Title: Carbon Dioxide Extraction From Air: Is It An Option?* 1999.

[44] Masoud Jahandar Lashaki, Soheil Khiavi, and Abdelhamid Sayari. *Stability of amine-functionalized CO2 adsorbents: A multifaceted puzzle*. June 2019. DOI: 10.1039/c8cs00877a.

[45] Andrew Lee et al. “A model for the adsorption kinetics of CO2 on amine-impregnated mesoporous sorbents in the presence of water”. In: *28th International Pittsburgh Coal Conference*. 2011.

[46] *LEWATIT® VP OC 1065 — lanxess.com*. https://lanxess.com/en-us/products-and-brands/products/l/lewatit--vp-oc-1065. [Accessed 25-07-2024].

[47] Kuijun Li, Joel D. Kress, and David S. Mebane. “The Mechanism of CO2 Adsorption under Dry and Humid Conditions in Mesoporous Silica-Supported Amine Sorbents”. In: *Journal of Physical Chemistry C* 120 (41 Oct. 2016), pp. 23683–23691. ISSN: 19327455. DOI: 10.1021/acs.jpcc.6b08808.

[48] Wen Li et al. “Steam-stripping for regeneration of supported amine-based CO2 adsorbents”. In: *ChemSusChem* 3 (8 2010), pp. 899–903. ISSN: 1864564X. DOI: 10.1002/cssc.201000131.

[49] P. Liu and G.F. Chen. *Porous Materials: Processing and Applications*. Elsevier Science, 2014. ISBN: 9780124078376. URL: https://books.google.nl/books?id=KwJ0AwAAQBAJ.

[50] Feijian Lou et al. “Impacts of nano-scale pore structure and organic amine assembly in porous silica on the kinetics of CO2 adsorptive separation”. In: *Nano Research* 14 (9 Sept. 2021), pp. 3294–3302. ISSN: 19980000. DOI: 10.1007/s12274-021-3609-3.

[51] Chungsying Lu et al. “Thermodynamics and regeneration of CO2 adsorption on mesoporous spherical-silica particles”. In: *Fuel Processing Technology* 90 (12 Dec. 2009), pp. 1543–1549. ISSN: 03783820. DOI: 10.1016/j.fuproc.2009.08.002.

[52] John. McMurry. *Organic chemistry*. The Brooks/Cole series in chemistry. Monterey, Calif.: Brooks/-Cole Pub. Co., 1984. URL: http://www.gbv.de/dms/bowker/toc/9780534012045.pdf.

[53] Noah McQueen et al. *A review of direct air capture (DAC): Scaling up commercial technologies and innovating for the future*. July 2021. DOI: 10.1088/2516-1083/abf1ce.

[54] Igor Medveď and Robert Černý. *Surface diffusion in porous media: A critical review*. July 2011. DOI: 10.1016/j.micromeso.2011.01.015.

[55] Anthony F. Mills. *Mass transfer.* Upper Saddle River: Prentice-Hall, 2001.

[56] Richard Monastersky. “Global carbon dioxide levels near worrisome milestone: concentrations of greenhouse gas will soon surpass 400 parts per million at sentinel spot”. In: *Nature* 497.7447 (2013), pp. 13–15.

[57] Fabio Montagnaro and Marco Balsamo. “Modelling CO2 adsorption dynamics onto amine- functionalised sorbents: A fractal-like kinetic perspective”. In: *Chemical Engineering Science* 192 (Dec. 2018), pp. 603–612. ISSN: 00092509. DOI: 10.1016/j.ces.2018.08.009.

[58] S. Tadayon Mousavi et al. “Coupling of multicomponent transport models in particle-resolved fluid-solid simulations”. In: *Chemical Engineering Science* 291 (June 2024). ISSN: 00092509. DOI: 10.1016/j.ces.2024.119920.

[59] Kathryn A. Mumford et al. *Review of solvent based carbon-dioxide capture technologies*. June 2015. DOI: 10.1007/s11705-015-1514-6.

[60] Shin-ichi Nakao et al. *Advanced CO2 capture technologies: absorption, adsorption, and membrane separation methods*. Springer, 2019.

[61] Burkhard Ohs, Maximilian Krödel, and Matthias Wessling. “Adsorption of carbon dioxide on solid amine-functionalized sorbents: A dual kinetic model”. In: *Separation and Purification Technology* 204 (Oct. 2018). Dual Kinetic Model, pp. 13–20. ISSN: 18733794. DOI: 10.1016/j.seppur.2018.04.009.

[62] G.S. Patience. *Experimental Methods and Instrumentation for Chemical Engineers*. Elsevier Science, 2017. ISBN: 9780444640383. URL: https://books.google.nl/books?id=W20etAEACAAJ.

[63] K. S.C. Peerenboom et al. “Mass conservative finite volume discretization of the continuity equations in multi-component mixtures”. In: *Journal of Computational Physics* 230 (9 2011), pp. 3525–3537. ISSN: 10902716. DOI: 10.1016/j.jcp.2011.02.001.

[64] John H Perry. *Chemical engineers’ handbook*. 1950.

[65] Elisabeth J. Quirijns et al. “Sorption isotherms, GAB parameters and isosteric heat of sorption”. In: *Journal of the Science of Food and Agriculture* 85 (11 Aug. 2005), pp. 1805–1814. ISSN: 00225142. DOI: 10.1002/jsfa.2140.

[66] Ronald R Remickt and Christie J Geankoplis. *Ternary diffusion of gases in capillaries in the transition region between knudsen and molecular diffusion*. 1974.

[67] Fateme Rezaei and Paul Webley. “Optimum structured adsorbents for gas separation processes”. In: *Chemical Engineering Science* 64 (24 2009), pp. 5182–5191. ISSN: 00092509. DOI: 10.1016/j.ces.2009.08.029.

[68] Hannah Ritchie and Max Roser. “CO2 emissions”. In: *Our World in Data* (2020).

[69] Joeri Rogelj et al. *Energy system transformations for limiting end-of-century warming to below 1.5 °C*. June 2015. DOI: 10.1038/nclimate2572.

[70] 1938- Ruthven Douglas M. (Douglas Morris), Shamsuzzaman. Farooq, and Kent S. 1951- Knaebel. *Pressure swing adsorption*. Englisch. New York, N.Y.: VCH Publishers, 1994. URL: http://www.gbv.de/dms/bowker/toc/9780471188186.pdf.

[71] Douglas M Ruthven. *Principles of adsorption and adsorption processes*. John Wiley & Sons, 1984.

[72] Nooshin Saadatkhah et al. *Experimental methods in chemical engineering: Thermogravimetric analysis —TGA*. Jan. 2020. DOI: 10.1002/cjce.23673.

[73] Eloy S. Sanz-Pérez et al. *Direct Capture of CO2 from Ambient Air*. Oct. 2016. DOI: 10.1021/acs.chemrev.6b00173.

[74] S. Satyapal et al. “Performance and properties of a solid amine sorbent for carbon dioxide removal in space life support applications”. In: *Energy and Fuels* 15 (2 Mar. 2001). heat of adsorption, bindi, pp. 250–255. ISSN: 08870624. DOI: 10.1021/ef0002391.

[75] Michel Schellevis. *CO2 capture from air a process engineering approach*. 2023.

[76] William E Schiesser. *The numerical method of lines: integration of partial differential equations*. Elsevier, 2012.

[77] Charles A. Seipp et al. “CO 2 Capture from Ambient Air by Crystallization with a Guanidine Sorbent”. In: *Angewandte Chemie* 129 (4 Jan. 2017), pp. 1062–1065. ISSN: 0044-8249. DOI: 10.1002/ange.201610916.

[78] Rodrigo Serna-Guerrero, Youssef Belmabkhout, and Abdelhamid Sayari. “Influence of regeneration conditions on the cyclic performance of amine-grafted mesoporous silica for CO2 capture: An experimental and statistical study”. In: *Chemical Engineering Science* 65 (14 July 2010), pp. 4166–4172. ISSN: 00092509. DOI: 10.1016/j.ces.2010.04.029.

[79] Rodrigo Serna-Guerrero and Abdelhamid Sayari. “Modeling adsorption of CO2 on amine- functionalized mesoporous silica. 2: Kinetics and breakthrough curves”. In: *Chemical Engineering Journal* 161 (1-2 2010), pp. 182–190. ISSN: 13858947. DOI: 10.1016/j.cej.2010.04.042.

[80] Jeremy D. Shakun et al. “Global warming preceded by increasing carbon dioxide concentrations during the last deglaciation”. In: *Nature* 484 (7392 Apr. 2012), pp. 49–54. ISSN: 00280836. DOI: 10.1038/nature10915.

[81] W.K. Shi et al. “Bi-disperse adsorption model of the performance of amine adsorbents for direct air capture”. In: *Chemical Engineering Journal* (July 2024), p. 154090. ISSN: 13858947. DOI: 10.1016/j.cej.2024.154090.

[82] Xiaoyang Shi, Yuanchunyu Lin, and Xi Chen. *Development of sorbent materials for direct air capture of CO2*. Apr. 2022. DOI: 10.1557/s43577-022-00320-7.

[83] Valentina Stampi-Bombelli, Mijndert van der Spek, and Marco Mazzotti. “Analysis of direct capture of CO 2 from ambient air via steam-assisted temperature–vacuum swing adsorption”. In: *Adsorption* 26 (7 Oct. 2020), pp. 1183–1197. ISSN: 15728757. DOI: 10.1007/s10450-020-00249-w.

[84] Valentina Stampi-Bombelli et al. “On Comparing Packed Beds and Monoliths for CO 2 Capture from Air Through Experiments, Theory, and Modeling”. In: *Industrial & Engineering Chemistry Research* 63 (26 July 2024), pp. 11637–11653. ISSN: 0888-5885. DOI: 10.1021/acs.iecr.4c01392. URL: https://pubs.acs.org/doi/10.1021/acs.iecr.4c01392.

[85] Valentina Stampi-Bombelli et al. “On Comparing Packed Beds and Monoliths for CO 2 Capture from Air Through Experiments, Theory, and Modeling”. In: *Industrial & Engineering Chemistry Research* 63 (26 July 2024), pp. 11637–11653. ISSN: 0888-5885. DOI: 10.1021/acs.iecr.4c01392. URL: https://pubs.acs.org/doi/10.1021/acs.iecr.4c01392.

[86] Dong Myung Suh and Xin Sun. “Particle-scale CO2 adsorption kinetics modeling considering three reaction mechanisms”. In: *International Journal of Greenhouse Gas Control* 17 (2013), pp. 388–396. ISSN: 17505836. DOI: 10.1016/j.ijggc.2013.05.029.

[87] Muhammad Sultan et al. “Insights of water vapor sorption onto polymer based sorbents”. In: *Adsorption* 21 (3 Apr. 2015), pp. 205–215. ISSN: 15728757. DOI: 10.1007/s10450-015-9663-y.

[88] Ross Taylor and R. Krishna. *Multicomponent mass transfer*. Wiley series in chemical engineering. New York: Wiley, 1993. URL: http://catdir.loc.gov/catdir/description/wiley031/92040667.html.

[89] Ed Tegeler et al. “A novel contactor for reducing the cost of direct air capture of CO2”. In: *Chemical Engineering Science* 281 (Nov. 2023). ISSN: 00092509. DOI: 10.1016/j.ces.2023.119107.

[90] NOAA US Department of Commerce. *Global Monitoring Laboratory - Carbon Cycle Greenhouse Gases*. Oct. 2005. URL: https://gml.noaa.gov/ccgg/trends/mlo.html.

[91] Rens Veneman et al. “Adsorption of H2O and CO2 on supported amine sorbents”. In: *International Journal of Greenhouse Gas Control* 41 (Oct. 2015), pp. 268–275. ISSN: 17505836. DOI: 10.1016/j.ijggc.2015.07.014.

[92] Pauli Virtanen et al. “SciPy 1.0: Fundamental Algorithms for Scientific Computing in Python”. In: *Nature Methods* 17 (2020), pp. 261–272. DOI: 10.1038/s41592-019-0686-2.

[93] Kay White Vugrin et al. “Confidence region estimation techniques for nonlinear regression in groundwater flow: Three case studies”. In: *Water Resources Research* 43.3 (2007).

[94] Junye Wu et al. “The analysis and evaluation of direct air capture adsorbents on the material characterization level”. In: *Chemical Engineering Journal* 450 (Dec. 2022). ISSN: 13858947. DOI: 10.1016/j.cej.2022.137958.

[95] Jan Andre Wurzbacher et al. “Heat and mass transfer of temperature-vacuum swing desorption for CO2 capture from air”. In: *Chemical Engineering Journal* 283 (Jan. 2016). model for desorption in columns experiment, pp. 1329–1338. ISSN: 13858947. DOI: 10.1016/j.cej.2015.08.035.

[96] Zhao Xing-Yun et al. *Using a Tree Ring S13C Annual Series to Reconstruct Atmospheric CO2 Concentration over the Past 300 Years*I*. 2006.

[97] John Young et al. “The impact of binary water-CO2 isotherm models on the optimal performance of sorbent-based direct air capture processes”. In: *Energy and Environmental Science* 14 (10 Oct. 2021), pp. 5377–5394. ISSN: 17545706. DOI: 10.1039/d1ee01272j.

[98] Jie Yu and Steven S.C. Chuang. “The structure of adsorbed species on immobilized amines in CO2 capture: An in situ IR study”. In: *Energy and Fuels* 30 (9 Sept. 2016). experimental study, compares the heat of adsorption of different species, pp. 7579–7587. ISSN: 15205029. DOI: 10.1021/acs.energyfuels.6b01423.

[99] Xuancan Zhu et al. “Design of steam-assisted temperature vacuum-swing adsorption processes for efficient CO2 capture from ambient air”. In: *Renewable and Sustainable Energy Reviews* 137 (Mar. 2021). Column fixed-bed Model for Amine modified material. ISSN: 18790690. DOI: 10.1016/j.rser.2020.110651.

[100] Xuancan Zhu et al. *Recent advances in direct air capture by adsorption*. July 2022. DOI: 10.1039/d1cs00970b.

7

Appendix A

Isotherm Models

Pure Water Adsorption

The adsorption of pure H_2O on amine-functionalized sorbent materials is commonly described by the Guggenheim-Anderson-de Boer (GAB) isotherm [95, 65, 87]. It is developed on the basis of the Langmuir and BET (Brunauer-Emmett-Teller) isotherm models [65]. The GAB isotherm model assumes a tightly bound monolayer on the sorbent surface, and a following multilayer where the molecules have a lower binding energy (which is equivalent to the heat of adsorption) than in the monolayer. The multilayer is assumed to include the second up until the ninth layer, in subsequent layers the heat of adsorption is assumed to be equal to the latent heat of condensation, just like in the bulk liquid [65, 97]. The heat of adsorption for the different layers are dependent on temperature, for which experimental data needs to be used to obtain an empirical fit [97]. The GAB isotherm equation is thus:

$$q_{\mathrm{H_2O}} = \frac{q_{\mathrm{m}} k c x}{(1 - kx)(1 + (c - 1)kx)}. \tag{7.1}$$

$q_{\mathrm{H_2O}}$ [mol kg^{-1}] is the water loading, q_{m} [mol kg^{-1}] the loading at the monolayer which acts as a measure of the available adsorption sites. The parameters k and c are dimensionless and need to be fitted to experimental data. c describes the binding strength of the molecules in the first layer compared to the molecules in the multilayer. Large values imply a stronger binding in the monolayer and a large difference to the multilayer. k indicates the same for the multilayer and the bulk fluid [65].

Dry $\mathbf{CO_2}$ Adsorption

The adsorption of CO_2 on amine-funtionalised sorbents in absence of H_2O has previously been described with a temperature-dependent form of the Toth model [28]. Compared to the Langmuir isotherm it improves the fit at high and low pressure. The Toth isotherm is defined as

$$q_{\mathrm{CO_2}} = \frac{q_\infty(T) b(T) p_{\mathrm{CO_2}}}{\left(1 + \left(b(T) p_{\mathrm{CO_2}}\right)^{\tau(T)}\right)^{\frac{1}{\tau(T)}}} \tag{7.2}$$

with $q_{\mathrm{CO_2}}$ [mol kg^{-1}] being the loading of CO_2 on the adsorbent, $p_{\mathrm{CO_2}}$ (in Pa) the partial pressure of CO_2. q_∞ [mol kg^{-1}] is the maximum CO_2 capacity and is described as

$$q_\infty(T) = q_{\infty,0} \exp\left(\chi\left(1 - \frac{T}{T_0}\right)\right) \tag{7.3}$$

where $q_{\infty,0}$ is at a reference temperature T_0 [K], T [K] is the temperature and χ [-] is a factor for the temperature dependency. b [Pa^{-1}] is defined by

$$b(T) = b_0 \exp\left(\frac{-\Delta H_0}{RT}\right) \tag{7.4}$$

and describes the affinity of CO_2 to the adsorbent. b_0 is an affinity parameter, ΔH_0 [Jmol^{-1}] is the isosteric heat of adsorption and R is the universal gas constant. $\tau[-]$ is a parameter to account for surface heterogeneity and is given by

$$\tau(T) = \tau_0 + \alpha \left(1 - \frac{T_0}{T}\right) \tag{7.5}$$

with the factor α used to describe the temperature dependency and τ_0 at a reference temperature.

Co-Adsorption

The mathematical modeling of the co-adsorption isotherm for H_2O and CO_2 remains a current subject of research. The following section provides an explanation and comparison of both empirical and kinetic approaches to address this modeling challenge. When both H_2O and CO_2 are present, different interaction mechanisms can influence the adsorption behavior. While the presence of CO_2 typically does not have a significant impact on the adsorption of H_2O on typical amine-functionalized sorbents [91, 5, 28, 18], water can alter the adsorption capacity of CO_2. As the ambient air contains between $18-60\,\%$ humidity on average, depending on the season, this effect is highly relevant [31]. As described in Section 3.1.8, the chemical adsorption mechanisms extend from only the formation of carbamates to the additional formation of bicarbonates when water vapour is present. The difference in the stoichiometric relations of the two reactions lead to different amine efficiency in dry and humid conditions ($\Phi = 0.5$ for carbamate and $\Phi = 1$ for bicarbonate) leading to an overall higher CO_2 adsorption capacity in the presence of water. Another effect that leads to higher CO_2 adsorption is that the presence of water changes the heat of adsorption, which changes the affinity to form bonds favourably. Yu et al. [98] find the heat of adsorption of carbamates to be higher than the one of species that involve the binding of water. As the heat of adsorption corresponds to the binding energy, this also alters the energy requirements for the TSA cycle. Less energy will be required to desorb CO_2 in the form of bicarbonates compared to carbamates, however, extra energy will be required to desorb the water molecules. Moreover, high amounts of water molecules present can block the CO_2 molecules access to amine sites, which can lower the adsorption capacity.

Empirical model based on the Toth-Isotherm [83] The model introduced by Stampi-Bombelli et al. is based on the Toth isotherm and extended by an affinity coefficient b [Pa^{-1}] and a water uptake dependence n_S [mol kg^{-1}]. The isotherm is defined as

$$q_{CO_2} = n_S(T, q_{H_2O}) \frac{b(T, q_{H_2O}) p_{CO_2}}{\left[1 + (b(T, q_{H_2O}) p_{CO_2})^{\tau(T)}\right]^{1/\tau(T)}} \tag{7.6}$$

with

$$n_s\left(T, q_{\mathrm{H_2O}}\right) = n_s(T) \left[\frac{1}{1 - \gamma q_{\mathrm{H_2O}}}\right] \quad \gamma > 0, \tag{7.7}$$

and

$$b\left(T, q_{\mathrm{H_2O}}\right) = b(T)\left(1 + \beta q_{\mathrm{H_2O}}\right) \quad \beta > 0. \tag{7.8}$$

The parameters γ and β [kg mol^{-1}] are then determined by equilibrium data for the present material, but are suggested to be positive. However, Young et al. state that γ might have negative values as they revise the model in their work and take into account the possibility that water molecules block available amine sites and thus reduce the CO_2 uptake capacity [97]. As explained above, the presence of water leads to a change in the adsorption capacity of CO_2 as well as to a change in its affinity [83, 32, 97]. In this model, the water uptake dependence n_S leads to an increase in both when water is present, and leaves the model as the regular Toth isotherm in dry conditions [83].

Isotherm and kinetics models [35, 20] Jung and Lee [35] propose a model that includes the adsorption kinetics and equilibrium for co-adsorption of H_2O and CO_2 on amine functionalized sorbents. The model is based on the mechanisms of the formation of carbamate and bicarbonate with the amines. However, the model neglects the reaction stoichiometry and the partial pressures of CO_2 and H_2O that were studied are higher than the ones occurring in ambient air, and are thus not applicable to DAC [20].

Elfving et al. [20] follow a kinetic approach which they use to develop an equilibrium model as well as a dynamic model that they fit to a column experiment. They introduce a 5-parameter and 7-parameter model that are based on the reactions forming carbamates in dry, and bicarbonates and hydronium carbamates in humid conditions. They include the fact that a formation of a carbamate includes two amine sites, while the formation of bicarbonates and hydronium carbamates only include one. Both of their models yield good results in describing the equilibrium data of the adsorption isotherm, with the 7-parameter only showing a slight improvement in the fit in the case of low humidity and low partial pressure. The difference in the dynamic model was clearer, as the 7-parameter model gave reasonably good results in regions where the 5-parameter model failed [20].

Mechanistic co-adsorption model [97] The mechanistic co-adsorption model is based on the three governing mechanisms described above (presence of water increasing the amine efficiency, presence of water changing the heats of adsorption, water molecules blocking access to amine sites for CO_2). The CO_2 loading q_{CO_2} [mol kg^{-1}] is defined dependent on the humidity, by including the amine efficiency under present conditions (Φ [$-$]) and dry conditions (Φ_{dry} [$-$]):

$$q_{CO_2} = \frac{\Phi}{\Phi_{dry}} f(p_{CO_2}, T, \Delta H_{ave}). \tag{7.9}$$

Here, f is the isotherm equation, which is dependent on temperature T [K], partial pressure p_{CO_2} [Pa] and the average heat of adsorption ΔH_{ave} [J mol^{-1}].

The effect of water blocking amine sites is included in the model by calculating the available amine sites for CO_2 adsorption.

$$\Phi_{available} = \Phi_{max} - f_{blocked} \tag{7.10}$$

Φ_{max} can be assumed to be 1, as it describes the maximum possible amine efficiency, and the fraction of the sites blocked $f_{blocked}$ needs to be determined. It is assumed that it is proportional to the size of adsorbed water aggregates, which is related to the loading of water on the adsorbent. Young et al. [97] compare the growth of the aggregates to the process of crystals growing in time and propose Avrami's equation.

To describe the transition of species formed, which leads to one molecule of CO_2 bonding with a single amine group instead of two, Young et al. [97] propose to use a Maxwell-Boltzman distribution.

$$\Phi = \Phi_{dry} + (\Phi_{available} - \Phi_{dry}) e^{-\frac{A}{q_{H_2O}}} \tag{7.11}$$

The critical water loading value A [mol kg^{-1}] needs to be fitted.

The effect of the change in heat of adsorption is included by calculating a weighted average between the wet and dry states with

$$\Delta H_{ave} = \left(1 - e^{-\frac{A}{q_{H_2O}}}\right) \Delta H_{dry} + e^{-\frac{A}{q_{H_2O}}} \Delta H_{wet}. \tag{7.12}$$

WADST co-adsorption model [97] To be able to use the mechanistic model, everything about the adsorption process of the pure species on the sorbent must be known. To develop a more general approach, the weighted average dual site Toth (WADST) model is proposed [97]. In this approach, the different species that can be formed during adsorption are viewed as different types of sites, i.e. one with an available water molecule and one without. Just like in the mechanistic model, an Arrhenius equation is used to describe the critical water loading A, which leads to equation

$$q_{CO_2} = \left(1 - e^{-\frac{A}{q_{H_2O}}}\right) \frac{q_{\infty,dry}(T) b_{dry}(T) p_{CO_2}}{\left(1 + (b_{dry}(T) p_{CO_2})^{\tau_{dry}(T)}\right)^{\frac{1}{\tau_{dry}(T)}}} + e^{-\frac{A}{q_{H_2O}}} \frac{q_{\infty,wet}(T) b_{wet}(T) p_{CO_2}}{\left(1 + (b_{wet}(T) p_{CO_2})^{\tau_{wet}(T)}\right)^{\frac{1}{\tau_{wet}(T)}}}. \tag{7.13}$$

The Toth model is used here to define the dry site of the isotherm with the pure-component parameters, while the wet site is fit to co-adsorption experiments.

General Isotherm Model [36] Kaneko and Lackner develop a general analytical binary isotherm model that can, among other cases, be applied to solid amines interacting with CO_2 and H_2O [36]. The model is generalized for primary, secondary, tertiary as well as quaternary amines. All the chemical species and reactions are included in the model. According to Kaneko and Lackner, only the adsorption process of water to the sorbent is specific to each material, and is thus not defined in the model. Instead, the water concentration in the solid, meaning the adsorbed water molecules to the solid amine surface needs to be taken into account, as well as the hydration water around ions. Accordingly, the water concentration is introduced in the reaction equations with the definition of hydration numbers. By defining equations for charge neutrality and mass conservation of the total nitrogen, and inserting the definitions of the equilibrium coefficients and Henry's constants, a set of equations is derived that can be solved for the CO_2 concentration. This general equation is firstly defined for aqueous ammonium, secondly adjusted for aqueous amine solutions including primary and secondary amines and lastly generalized to amine solids. The model is validated for aqueous ammonia, and Kaneko and Lackner suggest that it will be transferable to solid amines. A validation for the latter has however not yet been conducted.

Comparison of the models Young et al. compare their models and the one introduced by Stampi-Bombelli [83] by assessing their accuracy when validated with experimental data. Including the co-adsorption behaviour mainly led to differences in the results of CO_2 loading and mole fraction [97], thus changing the working capacity, which is one of the main indicators of the process performance. Young et al. find that the WADST and mechanistic model yield similar results, estimating the loadings $\sim 50\%$ higher during adsorption, and $\sim 30\%$ higher after desorption, leading to a $\sim 50\%$ higher cyclic working capacity compared to when no co-adsorption is included. As both the mechanistic and WADST model led to similar results, the choice depends on available input parameters. Opposed to that, Stampi-Bombellis model [83] predicts a similar working capacity in both cases [97]. They conclude that this behaviour is because of the fact that the empirical model does not take temperature into account, i.e. the model assumes the isotherm parameters to be dependent on the water loading but not on temperature, and predicts a constant increase in affinity and decrease in capacity for a certain water loading. Thus, it over-predicts the capacity at higher temperatures, leading to an under-prediction of the working capacity. Young et al. reject the findings of the Stampi-Bombelli model due to its inability to predict the behaviour at higher temperatures [97].

Jung et al. and Elfving et al. both develop models that are based on the kinetics of the occurring reactions [35, 20]. Jung et al.'s model is limited due to neglecting the reaction stoichiometry, furthermore it is only validated for partial pressures of CO_2 and H_2O higher than the ones occurring in ambient air [20]. Elfving et al. include the change in stoichiometry and obtain accurate results for all tested partial pressures. Crucial input parameters for both models are the kinetic constants of the reactions.

While Kaneko's and Lackner's model is the most general, applicable to different processes, it requires the knowledge of many input parameters such as equilibrium coefficients of all the transitions occurring in the process as well as measures for the water concentration in the solid and the hydration water, which are not easy to obtain. This makes the application to different materials, as well as different temperature conditions difficult. Moreover, it has not yet been validated for solid sorbents.

Models of adsortion kinetics

Kinetic models of the adsorption process in literature make use of various driving force models, where relationships between the current and the equilibrium CO_2 loading are approximated. Examples are the pseudo fist-order and second-order model [79], Avrami's kinetic models [79], the fractal-like kinetic model [57] and the Dual Kinetic Model [61], which yield reasonably good results. However, these models do not explicitly model intra-particle mass transfer, which is why kinetic constants include the effects of mass transfer as well as reaction kinetics. By modeling the adsorption in terms of reaction rates, the process can be described using only thermodynamic and kinetic parameters of the reactions. This makes it possible to describe the process in a more general way, dependent on different mechanisms of intra-particle mass transfer and more easily adjustable to different materials. Ge et al. [27] model the

kinetics of dry adsorption by using the reaction equation of carbamate formation. Lee et al. [45] propose a model that combines carabamate and bicarbonate formation in order to depict the process in humid conditons. Their model is adapted and adjusted by Suh and San, who combine it with a intra-particle diffusion model [86]. Later, a model based on the reactions for the formation of hydronium carbamates instead of bicarbonates is proposed by Li et al. [47].

Pore System Models

Parallel Pore Model If the pore size distribution is not uniform, one needs to account for the variation in diameter of the pores additional to their length, when defining the diffusivity. This is commonly done by using the *parallel pore model*, calculates the effective diffusivity based on the following equation:

$$\langle \varepsilon D \rangle = \int_0^\infty D_{eff}(r) f(r)\, dr; \quad D_{eff} = \frac{\langle \varepsilon D \rangle}{\tau}. \tag{7.14}$$

Here $f(r)dr$ is the fraction of pore volume that has a radius between r and $r + dr$, *i.e.* the pore size distribution function [37]. This model is equivalent to a structure that connects the different pore sizes in parallel.

Random Pore Model As pores of different sizes can be connected in series or parallel, the model was extended to the *random pore model*. This models the structure as an assembly of stacked layers of particles with a microporosity ε_{mi} that form a macroporosity ε_{ma} between them. The structure of two layers can then be described by four possible paths from which the following equation for the effective diffusivity can be derived:

$$D^e = \varepsilon_{\mathrm{ma}}^2 D_{\mathrm{ma}} + (\varepsilon_{mi})^2 \frac{(1 + 3\varepsilon_{\mathrm{ma}})}{1 - \varepsilon_{\mathrm{ma}}} D_{\mathrm{mi}}. \tag{7.15}$$

D_{ma} and D_{mi} refer to the macro- and micropore diffusivity, respectively.

8

Appendix B

Rate of Surface Diffusion

Ge et al. [27] estimate a surface diffusion coefficient for CO_2 through branched PEI of $D_S = 5.8e{-}14 \mathrm{m}^2/s$ at $T = 300\,\mathrm{K}$. They consider a material with a support of mesoporous ordered silicia (SBA-15). To estimate surface diffusion, they consider the PEI to be arranged in a layer of thickness $\delta = 2\,\mathrm{nm}$, covering the pore wall. For diffusion through the pore, they estimate a diffusion coefficient of $D_P = 1.48e-7 \mathrm{m}^2/s$, which agrees with estimations for Knudsen diffusion. As the difference between the diffusion coefficients is of several orders of magnitude, and the area of the cross section of the layer compared to the pore is small, surface diffusion does not play a deciding role in the diffusion in radial direction, and can thus be neglected.

To show this, the flow due to surface diffusion and the flow due to pore diffusion are estimated.

$$\Phi_S = J_S \cdot A_S \quad \text{and} \quad \Phi_P = J_P \cdot A_P \tag{8.1}$$

with

$$J_S = D_S \frac{C_\infty - 0}{R} \quad \text{and} \quad J_P = D_P \frac{C_\infty - 0}{R} \tag{8.2}$$

and

$$A_S = \pi \left(\frac{d_p}{2} + \delta \right)^2 - A_P \quad \text{and} \quad A_P = \pi \left(\frac{d_p}{2} \right)^2 . \tag{8.3}$$

D_S is taken as $5.8e - 14 \mathrm{m}^2/s$, and D_P is taken as the Knudsen diffusion coefficient, which is dependent on the pore size. The thickness of the layer δ is assumed to be in the same relation to the diameter as the pore as in Ge et al.'s estimations. Thus, the parameter $k = \frac{L}{dp}$ is kept constant. Now, the flow inside the layer and the pore are compared, while varying the pore size. For pore sizes between $d_p = 0.01 - 100\,\mathrm{nm}$, the diffusive flow due to pore diffusion is higher ($\gg$) than the one due to surface diffusion. This behaviour stays the same when the ratio k of δ and d_p is increased.

The same estimation can be made for water, when adjusting the respective values. However, as CO_2 lacks behind water in pore diffusion (see Section 4.1), surface diffusion of water is not relevant, as a fast surface diffusion of water would not speed up the adsorption process of CO_2.

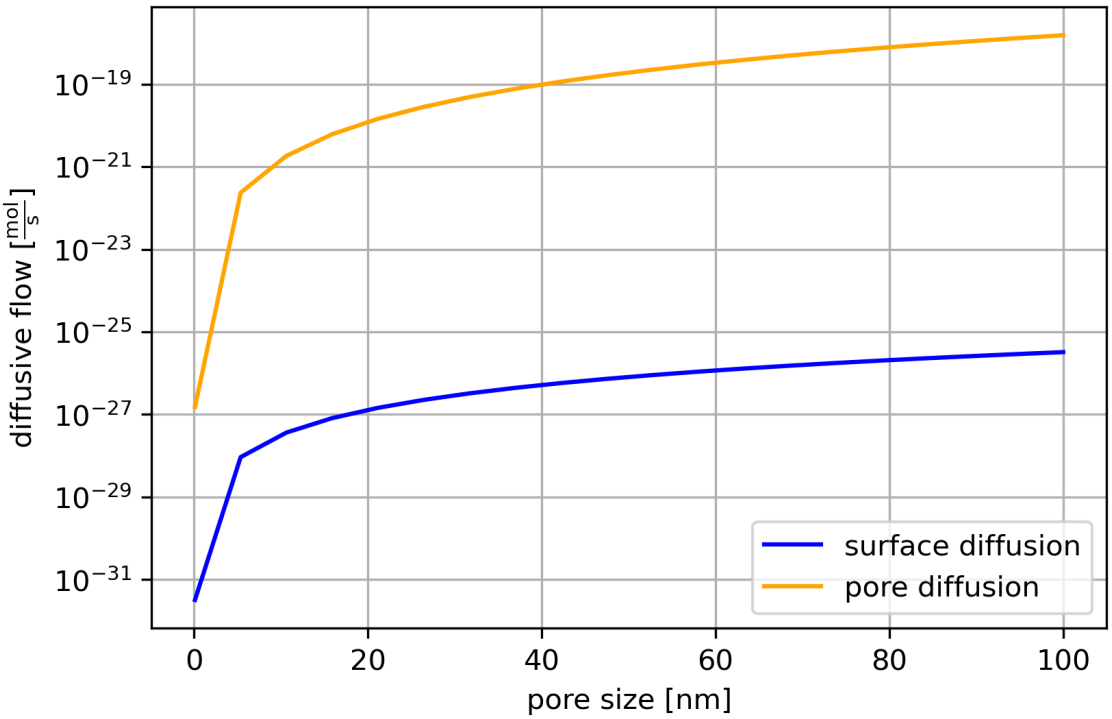

Figure 8.1: comparison of diffusive flows

Mesh Sensitivity

A study to evaluate mesh independence of the model is conducted. It is shown that results on the loading of the particle model is mesh independent for a gridsize of 40 gridpoints and higher. To establish mesh-independence in the contactor model, different refinements are tested. The refinement is referred to with the first number being the amount of gridpoints along the column, and the second being the amount of gridpoints in the particle, which is fixed to 40. The results of the breakthrough curves for the different refinements are illustrated in Figure 8.2. The biggest deviation of the curves is after around $1500\,\mathrm{min}$. Thus, this value is analysed quantitatively. The relative difference to the concentration of the finest discretization can be seen in Table 8.1

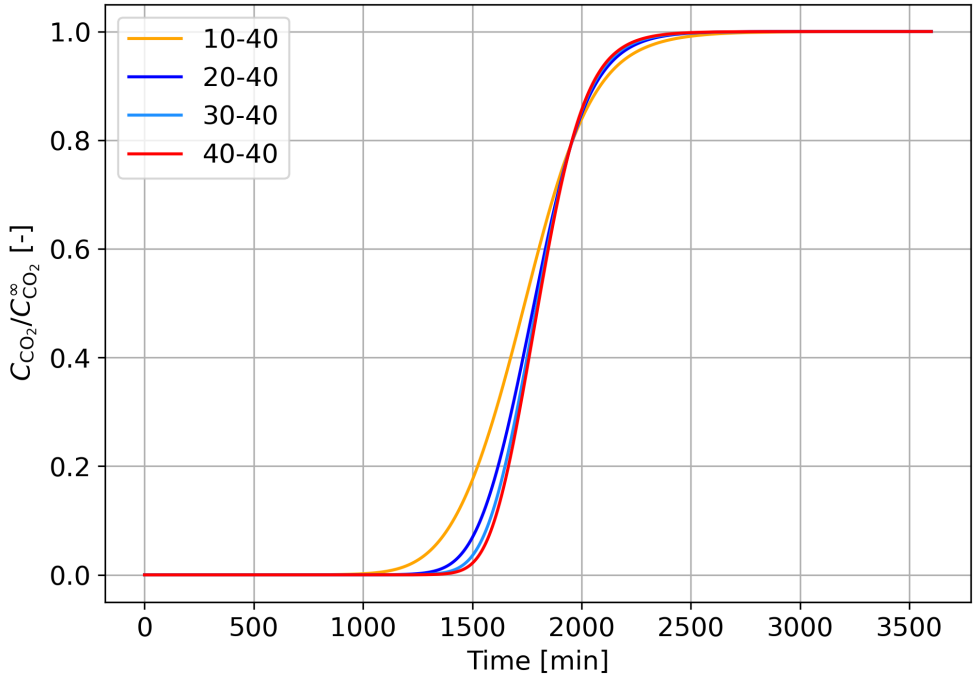

Figure 8.2: Caption

Table 8.1: Dimensions of the Packed Bed

Mesh	10-40	20-40	30-40
rel. deviation [%]	714	220.7	64.56

Considering that this is the point where the differences are the most prominent, and that the overall curves match well, the error to the grid with 30 discretization points is accepted for this study.

Validation dependence on particle size

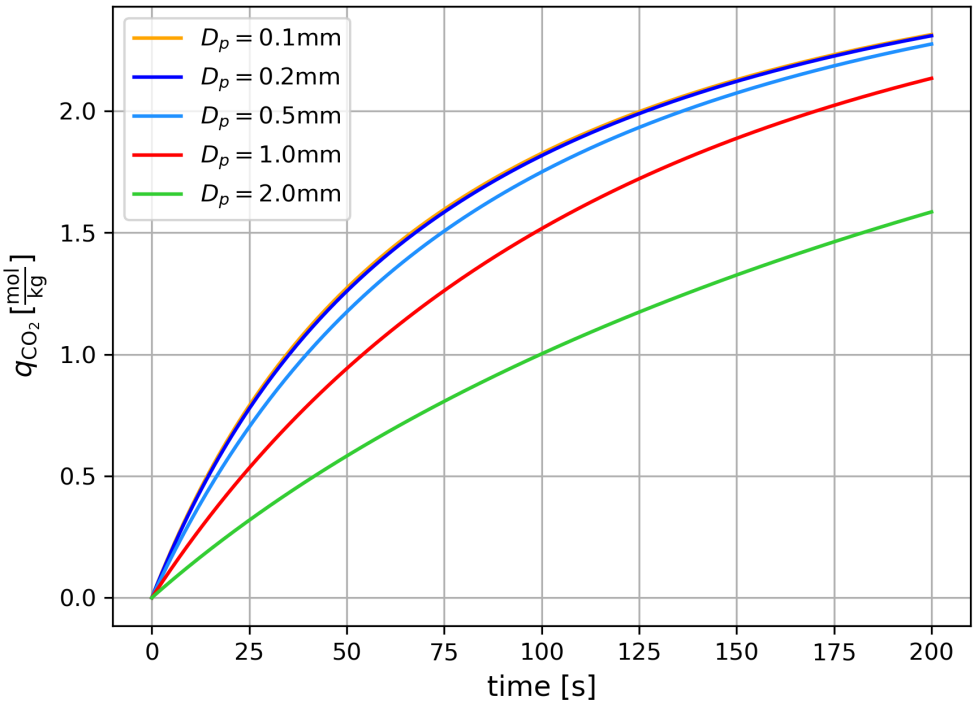

Figure 8.3: Model predictions on the uptake rate with different particle sizes, under the conditions from Bos et al.'s [9] experiments. Results show the same threshold in particle size from which diffusion limitations become relevant

Energy consumption of the fan for the monolith

For clarity, the energy consumed by the fan for the monolith is plotted on a smaller scale.

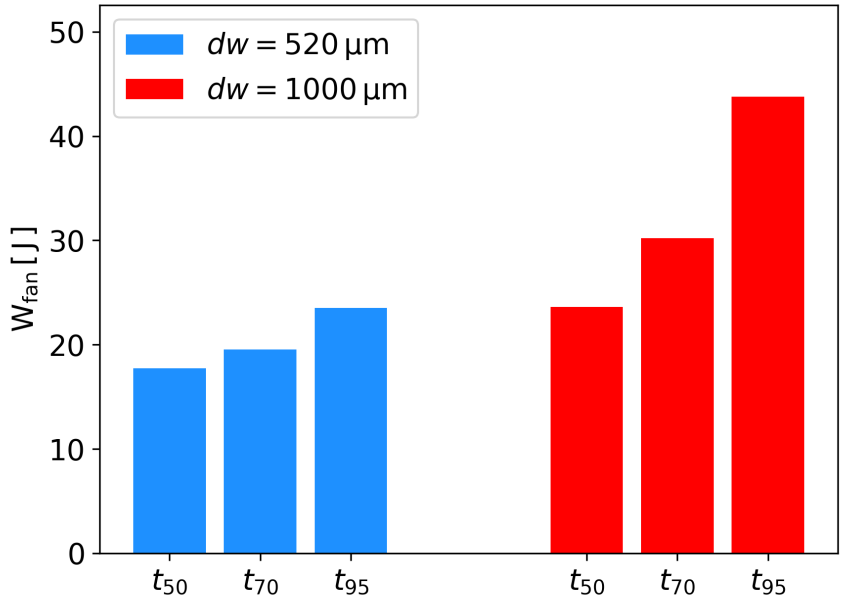

Figure 8.4: Energy consumed by the fan for the monolith at $dw = 520\,\mu\mathrm{m}$ and $dw = 1000\,\mu\mathrm{m}$, for reaching 50%, 70% and 95% breakthrough